



# DEVELOPMENT OF A TOMOGRAPHIC ATMOSPHERIC MONITORING SYSTEM BASED ON DIFFERENTIAL OPTICAL ABSORPTION SPECTROSCOPY

RUI FILIPE CANTARINO VALENTE DE ALMEIDA

Master in Biomedical Engineering

BIOMEDICAL ENGINEERING

NOVA University Lisbon  
(month), (year)



**NOVA**

NOVA SCHOOL OF  
SCIENCE & TECHNOLOGY

DEPARTMENT  
OF PHYSICS

---

# DEVELOPMENT OF A TOMOGRAPHIC ATMOSPHERIC MONITORING SYSTEM BASED ON DIFFERENTIAL OPTICAL ABSORPTION SPECTROSCOPY

RUI FILIPE CANTARINO VALENTE DE ALMEIDA

Master in Biomedical Engineering

**Adviser:** Mary Doe Adviser Name  
*Full Professor, NOVA University Lisbon*

**Co-advisers:** John Doe Co-Adviser Name  
*Associate Professor, NOVA University Lisbon*  
John Doe other Co-Adviser Name  
*Full Professor, NOVA University Lisbon*

BIOMEDICAL ENGINEERING

NOVA University Lisbon  
(month), (year)

## **Development of a Tomographic Atmospheric Monitoring System based on Differential Optical Absorption Spectroscopy**

Copyright © Rui Filipe Cantarino Valente de Almeida, NOVA School of Science and Technology, NOVA University Lisbon.

The NOVA School of Science and Technology and the NOVA University Lisbon have the right, perpetual and without geographical boundaries, to file and publish this dissertation through printed copies reproduced on paper or on digital form, or by any other means known or that may be invented, and to disseminate through scientific repositories and admit its copying and distribution for non-commercial, educational or research purposes, as long as credit is given to the author and editor.

*To my parents.*

---

## Acknowledgments

---

I know the pieces fit, 'cause I watched them fall away.

## ABSTRACT

Regardless of the language in which the dissertation is written, a summary is required in the same language as the main text and another summary in another language. It is assumed that the two languages in question are Portuguese and English.

The abstracts should appear first in the language of the main text and then in the other language. For example, if the dissertation is written in Portuguese the abstract in Portuguese will appear first, then the abstract in English, followed by the main text in Portuguese. If the dissertation is written in English, the abstract in English will appear first, then the abstract in Portuguese, followed by the main text in English.

In the L<sup>A</sup>T<sub>E</sub>X version, the NOVAtesis template will automatically order the two abstracts taking into account the language of the main text. You may change this behaviour by adding

```
\abstractorder(<MAIN_LANG>) := {<LANG_1>, ..., <LANG_N>}
```

to the customization area in the document preamble, e.g.,

```
\abstractorder(de) := {de, en, it}
```

The abstracts should not exceed one page and, in a generic way, should answer the following questions (it is essential to adapt to the usual practices of your scientific area):

1. What is the problem?
2. Why is this problem interesting/challenging?
3. What is the proposed approach/solution?
4. What results (implications/consequences) from the solution?

**Keywords:** Keyword 1, Keyword 2, Keyword 3, Keyword 4, Keyword 5, Keyword 6, Keyword 7, Keyword 8, Keyword 9, ...

## RESUMO

Independentemente da língua em que a dissertação esteja redigida, é necessário um resumo na mesma língua do texto principal e outro resumo noutra língua. Pressupõe-se que as duas línguas em questão sejam o português e o inglês.

Os resumos devem aparecer primeiro na língua do texto principal e depois na outra língua. Por exemplo, se a dissertação for redigida em português, o resumo em português aparecerá primeiro, seguido do resumo em inglês (*abstract*), seguido do texto principal em português. Se a dissertação for redigida em inglês, o resumo em inglês (*abstract*) aparecerá primeiro, seguido do resumo em português, seguido do texto principal em inglês.

Na versão L<sup>A</sup>T<sub>E</sub>X o template NOVAthesis irá ordenar automaticamente os dois resumos tendo em consideração a língua do texto principal. É possível alterar este comportamento adicionando

```
\abstractorder(<MAIN_LANG>) := {<LANG_1>, ..., <LANG_N>}
```

à zona de customização no preâmbulo do documento, e.g.,

```
\abstractorder(de) := {de, en, it}
```

Os resumos não devem ultrapassar uma página e, de forma genérica, devem responder às seguintes questões (é essencial adaptá-los às práticas habituais da sua área científica):

1. Qual é o problema?
2. Porque é que é um problema interessante/desafiante?
3. Qual é a proposta de abordagem/solução?
4. Quais são as consequências/resultados da solução proposta?

**Palavras-chave:** Palavra-chave 1, Palavra-chave 2, Palavra-chave 3, ...

# CONTENTS

<b>List of Figures</b>	<b>xi</b>
<b>List of Tables</b>	<b>xv</b>
<b>Acronyms</b>	<b>xvi</b>
<b>1 Introduction</b>	<b>1</b>
1.1 Background, Motivation and Starting Points . . . . .	1
1.1.1 Introduction . . . . .	1
1.1.2 Context . . . . .	1
1.2 Problem Introduction . . . . .	2
1.3 Literature review . . . . .	3
1.3.1 Tomography . . . . .	3
1.3.2 Differential Optical Absorption Spectroscopy (DOAS) . . . . .	5
1.3.3 DOAS Tomography . . . . .	5
1.4 Research Questions . . . . .	6
1.5 Hypothesis . . . . .	7
1.6 Methods and Findings . . . . .	8
1.7 Layout . . . . .	8
<b>2 Literature Review</b>	<b>10</b>
2.1 Air Pollution . . . . .	10
2.1.1 Criteria Pollutants . . . . .	11
2.1.2 Air Pollution Effects on Human Health . . . . .	11
2.1.3 Air Pollution effects on ecosystems . . . . .	17
2.1.4 Air Pollution Sources . . . . .	18
2.1.5 Detecting and Monitoring Air Pollution . . . . .	26
2.2 DOAS . . . . .	28
2.2.1 Types of DOAS experiments . . . . .	31
2.3 Important Notes on DOAS in practice . . . . .	36
2.3.1 Cross section conditioning . . . . .	36
2.3.2 Spectral Calibration . . . . .	37
2.4 Tomographic algorithms and reconstruction techniques . . . . .	39
2.5 DOAS Tomography . . . . .	45

## CONTENTS

---

<b>3 Methods</b>	<b>49</b>
3.1 Tomosim . . . . .	49
3.1.1 Discretisation . . . . .	51
3.1.2 Phantoms . . . . .	56
3.1.3 Error Estimation . . . . .	57
3.1.4 Reconstruction Results . . . . .	59
3.2 The Experiment . . . . .	62
3.2.1 Protocol and conduction . . . . .	63
3.2.2 First Run . . . . .	65
3.2.3 Second run . . . . .	68
3.2.4 Data Processing . . . . .	70
3.2.5 The DOAS Library . . . . .	73
<b>4 Discussion</b>	<b>75</b>
4.1 First Hypothesis . . . . .	75
4.2 Second Hypothesis . . . . .	76
<b>5 Conclusions</b>	<b>79</b>
<b>Bibliography</b>	<b>81</b>
<b>Annexes</b>	

## LIST OF FIGURES

1.1	A schematic representation of a projection acquisition. In this image, taken from [41], the clear line that comes down at a diagonal angle is a projection.	4
2.1	Annotated anatomy of the respiratory system [84]. . . . .	12
2.2	Possible abnormalities caused by Air Pollution (AP) exposure <i>in utero</i> . Notice that time of exposure is of critical importance [84]. . . . .	15
2.3	Developmental stages of the lung throughout life vs the risks of AP exposure in each stage [84]. . . . .	16
2.4	Dramatic photograph depicting the Capelinhos' lighthouse, half a kilometer from the eruption site, surrounded by a cloud of ash Particulate Matter (PM), volcanic gas and water vapor with more than 1km in height[81]. .	20
2.5	House almost completely buried by the Black Sunday dust storm. Several houses were entirely swallowed during this storm, trapping people inside, as if a big blizzard had hit them. Unlike a blizzard though, there was nothing anyone could do to keep the dirt outside, and all surfaces were covered black [72]. . . . .	21
2.6	Carbon Dioxide (CO <sub>2</sub> ) atmospheric concentrations since the year 1000. Note the seemingly exponential increase since the 1800s. Plotted and published by the 2 Degrees Institute [1] with data from ice cores [29] and in situ monitors [80]. . . . .	22
2.7	Schematic presentation on the sources of anthropogenic pollution and its categorisation according to the IPCC. Adapted from [14] . . . . .	23
2.8	Chinese energy production, Gross Domestic Product (GDP) and CO <sub>2</sub> emissions. Data collected from the World Bank and International Energy Agency websites [89, 43] . . . . .	24
2.9	General trends for European emissions. Data presented in % emissions of year 2000. Note the downward global trend in pollutant emissions, and its decoupling with the European GDP [28]. . . . .	25
2.10	European emissions divided by activity sector. The global decreasing trend is confirmed, as industries all around are producing less and less AP with the passing years [28]. . . . .	26
2.11	Semiconductor electrochemical sensor basic structure. There are many examples of this type of sensors, but in general they follow this architecture [19]. . . . .	28

---

## LIST OF FIGURES

---

2.12 Simplified schematic flowchart of the DOAS algorithm, including the non-linear part . . . . .	32
2.13 Active DOAS schematic. . . . .	32
2.14 Passive DOAS schematic. . . . .	33
2.15 Several examples of possible passive DOAS experiment geometries. All these examples use only the light from an astronomical source to detect many atmospheric trace gases. All these examples were taken from [65].	34
2.16 Occultation measurement schematic representation [65] . . . . .	34
2.17 Schematic representation of the limb satellite measurement geometry. .	35
2.18 Schematic representation of the nadir satellite measurement geometry.	35
2.19 Before being used in DOAS calculations, literature trace gas cross section spectra must undergo a conditioning process to make sure they are compatible with the current experiment's instruments. Figure adapted from [4]	37
2.20 This figure, taken from [4], shows the difference between NO <sub>2</sub> cross sections. The red line comes from the literature, and has been conditioned to the experiment spectrometer. The blue line was actually collected with that device. The slight discrepancies that can be observed are calibration defects.	38
2.21 High resolution solar spectrum commonly used to calibrate the various spectral signals in DOAS experiments [18]. . . . .	39
2.22 Schematic representation for coordinate setting. The image depicts a parallel projection setting [47]. . . . .	41
2.23 The Fourier Slice Theorem (FST), a schematic representation [3]. . . . .	42
2.24 Schematic representation of an equiangular fan-beam projection, taken from [46]. . . . .	44
2.25 Simplified diagram of the Systematic Mapping Study (SMS) method. This type of study is focused on registering every step of the search and the reading of the retrieved material, in an effort to make the process completely repeatable. Adapted from [49]. . . . .	46
2.26 BABII assembly geometry. In this experiment campaign, the telescopes illuminated retroreflecting targets that were positioned in two steel towers on both sides of a busy motorway in Germany, connecting Heidelberg to Mannheim [69]. . . . .	46
2.27 Erna Frins's paper [32] proposes a very relevant passive DOAS application that can conceptually be employed in a DOAS tomography scenario. In this 2006 paper, the authors use multi-axis measurements of sun-illuminated targets to estimate absorption paths without using radiative transfer models. . . . .	48
3.1 Hexacopter in flight. Image taken from LevelFiveSupplies[52], for illustration purposes only. . . . .	50

3.2 Illustration of the projection gathering algorithm based on the assembly of groups of acquisitions as fanbeam projections. The lines presented on the drawing come from the right to the left. Each is a ray in fan, corresponding to one stop of the drone. In the second measurement moment, the drone moves to the exit point on the left and repeats the first moment collection. Here, both fans and rays are separated by 5 degrees and there are 6 rays within each fan. A "real life" acquisition would feature a lot more rays, but that would be graphically complicated for the reader. Both ray and fan angular distance are customisable at runtime. Map taken from Google Maps in 2019. ©Google.	51
3.3 Grid and pixel definition, as they appear in the original article by Robert Siddon [75]. Pixels are "formed" by intersecting the ray (here going from point 1 to point 2) with the superimposed grid.	52
3.4 $P_2$ Calculation. The software uses the position of the drone, as defined by the vertical angle, $\beta$ , and the distance between the drone and the centre of the trajectory, $D$ , to determine $P_2$ through the solution of a second degree equation.	55
3.5 A graphical representation of the new spectral phantom, custom built for the TomoSim application.	57
3.6 Error estimation graphical representation. Note errors are extremely exaggerated for visualisation purposes.	58
3.7 Sinogram examples: the new spectral phantom projection data at a projection interval of 1 degree. On the left, the projection data before resorting; on the right, the parallel projection data obtained after resorting the fan-beam line integrals.	60
3.8 Tomographic reconstruction results, projection interval of 1 degree. From left to right: original phantom, FBP reconstruction, SART reconstruction, MLEM reconstruction	60
3.9 Tomographic reconstruction errors. Each one of these images was constructed by subtracting the respective reconstruction matrix, displayed in Figure 3.8, from the original phantom matrix. Error value is normalised to the pixel values, i.e., 32 bit floating point numbers with values between 0 and 1.	60
3.10 Reconstruction degradation: the projection interval was crucial for reconstruction. Note the image degradation going from a projection interval of 1 degree to 5 degrees (left to right). Images reconstructed using the FBP algorithm.	61
3.11 Location of observer points for the physical experiment.	63
3.12 Published spectrum of the CREE XHP50.2 LED light. The LED that was used in this experiment corresponds to the blue line [20].	64
3.13 Spectrum measured with the experiment spectrometers, at a distance of approximately 50 m from the torchlight.	64
3.14 View from West Bank assembly at sunrise during the first run of the experiment. Note that even with the sun appearing in the back, the light from the torch is perfectly visible at this distance.	66

## LIST OF FIGURES

---

3.15 Optical densities calculated with reference to measurement #1 for the other measurement moments in the active DOAS mode. . . . .	67
3.16 Optical densities calculated with reference to measurement #1 for the other measurement moments in the passive DOAS mode. . . . .	67
3.17 Calculated Nitrogen Dioxide (NO <sub>2</sub> ) concentrations for the various measurement moments. Each integer in the horizontal axis corresponds to a moment, organized chronologically. . . . .	68
3.18 This image, built using Google Maps, illustrates the East Bank relocation that took place in the second leg of the experiment. The first location is presented as EB <sub>1</sub> , while the second is naturally EB <sub>2</sub> . The West Bank is also presented for some geographic reference, and identified by WB. . . . .	69
3.19 Active DOAS molecular density for NO <sub>2</sub> , varying with the measurement number. . . . .	70
3.20 Passive DOAS molecular density for NO <sub>2</sub> , varying with the measurement number. Note that this is the difference between the density obtained at the two experiment assemblies, as per hypothesis 2 (see 4.2). . . . .	70
3.21 Active DOAS fit results. Each plot corresponds to one measurement moment. . . . .	71
3.22 Passive DOAS fit results, from the system on the East Bank. Each plot corresponds to one measurement moment. . . . .	71
3.23 Passive DOAS fit results, from the system on the West Bank. Each plot corresponds to one measurement moment. . . . .	71
3.24 The Avantes ASCII file format. This is a screenshot of a file of this type opened in the VIM text editor. Note its particular structure, around which the file / folder parsing objects described by Figure 3.26 and Figure 3.27 are constructed. . . . .	72
3.25 The Data processing. The Object Oriented Programming (OOP) approach that was taken attempts to take advantage of the organisational structure of the spectral data, by modelling it into Python objects. . . . .	72
3.26 The file loading process. An Avantes ASCII file originates an AvantesASCII object, which besides a series of string-parsing operations stores the data in a Pandas DataFrame, for easy access and control. . . . .	73
3.27 The folder loading process. Each folder can have many files. The way in which the data is gathered (described in Subsection 3.2.2) requires some global operations performed on groups of files, like summation and normalisation (with reference to the integration time). The AvantesASCIIFolder object provides such operations. . . . .	73
3.28 UML diagram for the DOAS library. The OOP approach that was followed allows for an instrument-oriented experiment parametrisation, which is not available in any other software . . . . .	74

## LIST OF TABLES

1.1	Main research question . . . . .	7
1.2	Secondary research questions . . . . .	7
2.1	Global energy production, divided according to the fuel used to obtain it and the production country . . . . .	24
3.1	Table summarising the new phantom's construction details, as a sum of 5 Gaussian profiles and an ellipse designed using TomoPhantom. In this table, Co is the object's amplitude, Xo and Yo are its center coordinates, and a and b are the objects half-widths. The table is constructed using TomoPhantom's particular syntax and more information can be obtained at [48]. . . . .	56
3.2	Reconstruction error table for the new spectral phantom at several projection intervals. The MLEM routine used pure fan-beam data while the other two used resorted parallel information. Errors presented were calculated using the Root Mean Square Errors, normalised to the range of the reconstructed image. . . . .	59
3.3	Summary table for the two experiment assemblies. Note the difference in terms of material, due to the two different roles both assemblies play during the experiment. This is translated into not having the need of an artificial light source in the West Bank's assembly. . . . .	64
3.4	Actions are the indivisible unit upon which each capture is built. The prescribed actions for this experiment are described in this table. . . . .	65
3.5	Captures are particular sets of actions that are conducted according to a specific order, depending on the time of day on which the capture is run. This table describes the prescribed captures on which this experiment consisted.	65
3.6	First run: measurement table. . . . .	66
3.7	Second run: time of measurements table. . . . .	69
3.8	Parameters for the DOAS measurements relative to the second run of the experiment. . . . .	70

## ACRONYMS

<b>ALRI</b>	Acute Lower Respiratory Infections <a href="#">i, 13</a>
<b>ANS</b>	Autonomic Nervous System <a href="#">i, 13, 14</a>
<b>AP</b>	Air Pollution <a href="#">i, ix, xi, 1, 2, 3, 6, 10, 11, 12, 13, 14, 15, 16, 17, 18, 19, 21, 22, 23, 24, 25, 26, 27, 28</a>
<b>API</b>	Application Programming Interface <a href="#">i, 56</a>
<b>ART</b>	Algebraic Reconstruction Technique <a href="#">i, 4</a>
<b>ASCII</b>	American Standard Code for Information Interchange <a href="#">i, 64, 70</a>
<b>BAEP</b>	Brainstem Auditory-Evoked Potentials <a href="#">i, 15</a>
<b>BTU</b>	British Thermal Unit <a href="#">i, 22</a>
<b>CEM</b>	Continuous Emission Monitoring <a href="#">i</a>
<b>CNS</b>	Central Nervous System <a href="#">i, 16</a>
<b>CO</b>	Carbon Monoxide <a href="#">i, 25, 27, 35</a>
<b>CO<sub>2</sub></b>	Carbon Dioxide <a href="#">i, xi, 22, 24, 27, 35</a>
<b>COPD</b>	Chronic Obstructive Pulmonary Disease <a href="#">i, 13, 16</a>
<b>CT</b>	Computed Tomography <a href="#">i, 3, 4, 39</a>
<b>CVD</b>	Cardiovascular Disease <a href="#">i, 13</a>
<b>CVM</b>	Cardiovascular Mortality <a href="#">i, 13, 14</a>
<b>DIAL</b>	Differential Absorption LIDAR <a href="#">i</a>
<b>DOAS</b>	Differential Optical Absorption Spectroscopy <a href="#">i, ix, xii, xiv, 2, 5, 6, 7, 8, 11, 28, 29, 30, 31, 32, 33, 34, 35, 36, 37, 38, 39, 40, 45, 46, 47, 48, 49, 50, 62, 68, 70, 71, 73, 74, 76, 77</a>
<b>EEA</b>	European Environmental Agency <a href="#">i, 10, 11, 25</a>
<b>EPA</b>	Environmental Protection Agency (United States) <a href="#">i, 10</a>
<b>ESCAPE</b>	European Study of Cohorts for Air Pollution Effects <a href="#">i, 13</a>
<b>FBP</b>	Filtered BackProjection <a href="#">i, 4, 41, 42, 43, 44</a>
<b>FFF</b>	Forest Fire Finder <a href="#">i, 1, 2</a>
<b>FP7</b>	European Union's Seventh Framework Programme <a href="#">i, 13</a>

<b>FST</b>	Fourier Slice Theorem <a href="#">i</a> , <a href="#">xii</a> , <a href="#">41</a> , <a href="#">42</a>
<b>FT</b>	Fourier Transform <a href="#">i</a> , <a href="#">41</a> , <a href="#">42</a>
<b>FWHM</b>	Full Width at Half Maximum <a href="#">i</a> , <a href="#">36</a>
<b>GDP</b>	Gross Domestic Product <a href="#">i</a> , <a href="#">xi</a> , <a href="#">22</a> , <a href="#">24</a> , <a href="#">25</a>
<b>H<sub>2</sub>O</b>	Water <a href="#">i</a> , <a href="#">35</a>
<b>H<sub>2</sub>S</b>	Hydrogen Sulfide <a href="#">i</a> , <a href="#">19</a>
<b>ICE</b>	Internal Combustion Engine <a href="#">i</a>
<b>ICE</b>	Internal Combustion Engine <a href="#">i</a> , <a href="#">24</a> , <a href="#">25</a>
<b>IEP</b>	InfraEstruturas de Portugal <a href="#">i</a> , <a href="#">63</a> , <a href="#">65</a>
<b>IFT</b>	Inverse Fourier Transform <a href="#">i</a> , <a href="#">42</a> , <a href="#">43</a>
<b>IOT</b>	Internet Of Things <a href="#">i</a> , <a href="#">2</a>
<b>LPG</b>	Liquefied Petroleum Gas <a href="#">i</a> , <a href="#">25</a>
<b>MAX-DOAS</b>	MultiAxis-DOAS <a href="#">i</a> , <a href="#">5</a> , <a href="#">6</a> , <a href="#">34</a>
<b>ML</b>	Machine Learning <a href="#">i</a>
<b>MLEM</b>	Maximized Likelihood Expectation Maximization <a href="#">i</a> , <a href="#">4</a>
<b>MSE</b>	Mean Squared Error <a href="#">i</a> , <a href="#">58</a> , <a href="#">59</a>
<b>NH<sub>3</sub></b>	Ammonia <a href="#">i</a> , <a href="#">26</a>
<b>NO<sub>2</sub></b>	Nitrogen Dioxide <a href="#">i</a> , <a href="#">xiv</a> , <a href="#">6</a> , <a href="#">11</a> , <a href="#">13</a> , <a href="#">15</a> , <a href="#">17</a> , <a href="#">27</a> , <a href="#">67</a> , <a href="#">68</a> , <a href="#">70</a> , <a href="#">77</a> , <a href="#">78</a>
<b>NO<sub>x</sub></b>	Nitrogen Oxides <a href="#">i</a> , <a href="#">25</a>
<b>O<sub>3</sub></b>	Ozone <a href="#">i</a> , <a href="#">11</a> , <a href="#">15</a> , <a href="#">18</a>
<b>O<sub>4</sub></b>	Tetraoxygen <a href="#">i</a>
<b>OECD</b>	Organisation for Economic Cooperation and Development <a href="#">i</a> , <a href="#">6</a>
<b>OOP</b>	Object Oriented Programming <a href="#">i</a> , <a href="#">xiv</a> , <a href="#">70</a> , <a href="#">72</a> , <a href="#">73</a> , <a href="#">74</a>
<b>PAH</b>	Polycyclic Aromatic Hydrocarbons <a href="#">i</a> , <a href="#">15</a>
<b>PICOC</b>	Population Intervention Context Objective Comparison <a href="#">i</a>
<b>PM</b>	Particulate Matter <a href="#">i</a> , <a href="#">xi</a> , <a href="#">11</a> , <a href="#">13</a> , <a href="#">14</a> , <a href="#">15</a> , <a href="#">19</a> , <a href="#">20</a> , <a href="#">21</a>
<b>Project ATMOS</b>	ATmosphere MOnitoring System Project <a href="#">i</a> , <a href="#">1</a> , <a href="#">2</a>
<b>PT2020</b>	Portugal2020 <a href="#">i</a> , <a href="#">1</a> , <a href="#">2</a>
<b>ROI</b>	Region Of Interest <a href="#">i</a> , <a href="#">3</a> , <a href="#">8</a> , <a href="#">49</a> , <a href="#">50</a> , <a href="#">51</a> , <a href="#">52</a>
<b>RQ</b>	Research Question <a href="#">i</a> , <a href="#">7</a> , <a href="#">8</a> , <a href="#">49</a>
<b>RTK GPS</b>	Real Time Kinematic Global Positioning System <a href="#">i</a> , <a href="#">57</a>
<b>SART</b>	Simultaneous Algebraic Reconstruction Technique <a href="#">i</a> , <a href="#">4</a>
<b>SGA</b>	Small for Gestation Age <a href="#">i</a> , <a href="#">14</a> , <a href="#">15</a>
<b>SLR</b>	Systematic Literature Review <a href="#">i</a>
<b>SLR</b>	Systematic Literature Review <a href="#">i</a>
<b>SMS</b>	Systematic Mapping Study <a href="#">i</a> , <a href="#">xii</a> , <a href="#">45</a> , <a href="#">46</a>

## ACRONYMS

---

<b>SO<sub>2</sub></b>	Sulfur Dioxide <a href="#">i</a> , <a href="#">15</a> , <a href="#">17</a> , <a href="#">19</a>
<b>TDL</b>	Tunable Diode Laser <a href="#">i</a>
<b>UAV</b>	Unmanned Aerial Vehicle <a href="#">i</a> , <a href="#">1</a> , <a href="#">8</a> , <a href="#">50</a>
<b>UML</b>	Unified Modelling Language <a href="#">i</a> , <a href="#">73</a>
<b>USB</b>	Universal Serial Bus <a href="#">i</a> , <a href="#">64</a>
<b>VOC</b>	Volatile Organic Compound <a href="#">i</a> , <a href="#">21</a>
<b>WFM-DOAS</b>	Weighting Function Modified Differential Optical Absorption Spectroscopy <a href="#">i</a> , <a href="#">34</a> , <a href="#">35</a>
<b>WHO</b>	World Health Organization <a href="#">i</a> , <a href="#">2</a>

## TODO LIST

Description of criteria pollutants and an explanation of their chemistry and atmospheric cycles. . . . .	11
Read the first leg of the expeiment again; add some official data; check to see if it plays out ok. . . . .	76



# INTRODUCTION

## 1.1 Background, Motivation and Starting Points

### 1.1.1 Introduction

This thesis describes the work that I have done in the past 4 years on the design and development of a miniaturized system for atmospheric monitoring based on optical spectroscopy. The project itself was the major part of the [ATmosphere MOnitoring System Project \(Project ATMOS\)](#), an initiative that was contemplated with European funding through a [Portugal2020 \(PT2020\)](#) initiative and came as a response to the growing weight that [AP](#) has in the whole Western world.

The potential impact of [AP](#) on human health is amply documented. Numerous papers have, for decades, established many links between air quality and several common ailments like respiratory syndromes and cardiovascular diseases. Similar connections have also been found regarding the probability of gestational malformations and several types of cancer. On a different level, and of perhaps less immediate concern, are the effects that have been observed on ecosystems. Many times these effects are difficult to predict (and timely mitigate) and in some cases have been known to interfere with people's livelihood. In time, and if not addressed, these interferences will certainly hinder economies and limit the quality of life of populations globally. The severity of this problem makes it clear that we need to tackle it intelligently, and this approach requires that we can measure, trace and track [AP](#) effectively, which beckons engineers and scientists to create more technology for this specific purpose.

Answering this call, with this work I have tried to create a reply to the question of whether it would be possible to develop a two-dimensional pollutant mapping tool, small enough to be fitted onto a [Unmanned Aerial Vehicle \(UAV\)](#), which came to be a to-morphographically enabled design. To this end, I have developed a simulation platform that computationally proves the method's feasibility and confirmed through experiments that the hypothesis on which the solution is based, regarding the use of sequentially measured scattered sunlight as analogous to an artificial light source is valid.

### 1.1.2 Context

The idea behind this thesis was born in 2015, at NGNS-IS (a Portuguese tech startup). At the time, the company's flagship product was the [Forest Fire Finder \(FFF\)](#). The

**FFF** was a forest fire detection system, capable of mostly autonomous and automatic operation. The system was the first application of **DOAS** for fire detection, and for that it was patented in 2007 (see [86, 85]). The **FFF** is a remote sensing device that scans the horizon for the presence of a smoke column, sequentially performing a chemical analysis of each azimuth, using the Sun as a light source for its spectroscopic operations [83].

The **FFF** was deployed in several "habitats", both nationally (Parque Nacional da Peneda-Gerês and Ourém) and internationally (Spain and Brazil). One of the company's clients at the time was interested in a pollution monitoring solution, and asked if the spectroscopic system would be capable of performing such a task. The challenge resonated through the company's structure and the idea that created this thesis was born. The team then started reading about the concept of **AP** and how both populations and entities were concerned about it. It became clear that, while there were already several methods to measure **AP**, there was a clear market drive for the development of a system that could leverage the large area capabilities of a **DOAS** device while being able to provide a more spatially resolved "picture" of the atmospheric status. With this in mind, the company managed to have the investigation financed through a **PT2020** funding opportunity. This achievement was a clear validation of the project's goals and of the need there was for a system with the proposed capabilities. It was, however, not enough. **FFF** was a very good starting point, but there was still a lot of continuous research work needed before any of the goals that had been set were achieved. This led to the publication of this PhD project, in a tripartite consortium between FCT-NOVA, NGNS-IS and the Portuguese Foundation for Science and Technology. Its main goal was to develop an atmospheric monitoring system prototype that would be able to spectroscopically map pollutant concentrations in a two-dimensional way.

In April 2017, NGNS-IS was integrated in the Compta group, one of the oldest IT groups operating in Portugal. Despite its age, this company is one of the main presences in some of the most modern industrial fields, like **Internet Of Things (IOT)** applications. **Project ATMOS**'s pollutant tracing capabilities made it an almost perfect fit in one of **IOT**'s most resounding niches, the *Smart Cities* trend. Unfortunately, the transition between one company and the other, regardless of the project's adequacy, was anything but smooth. Almost two years later, in the beginning of 2019, engulfed in a sea of endless bureaucracy and ill intent on behalf of the managing governmental authorities (who seemed always more interested in seeing the project fail than anything else), **Project ATMOS** was terminated and financing was cut.

## 1.2 Problem Introduction

**Air Pollution** poses an important threat to the human way of life. The **World Health Organization (WHO)** have estimated that 1 out of each 9 deaths in 2012 were **AP**-related and of these, 3 million were directly attributable to outdoor **AP** worldwide, most of which in developing countries (87% vs 82% population). Although the European picture is not so dire as this, the topic does cause concern. In 2016, there were an estimated 400.000 deaths due to **AP** in Europe, 391.000 of which in the EU-28

space [36]. An increased number of premature deaths is sufficiently bad for treating this issue seriously, but the problems brought forth by [Air Pollution](#) do not end here. Not only are people dying more, disabilities (namely respiratory) are more frequent, and so are hospital visits. These two factors represent a decrease in productivity and an increase in medical costs, which accrue to the huge burden that [AP](#) already represents to any society. In Europe, health impacts of diesel emissions were estimated to be in the region of 60 billion euros [17] for the year of 2016.

These impressive numbers have perspired onto the public opinion, which is (now more than ever) concerned with the whole problem of [AP](#). In fact, the subject is considered by the public the second most important environmental threat (after Climate Change, which is a very related topic), and citizens throughout Europe have been partaking in initiatives which aim to aid and incentivize air quality monitoring, as well as raising awareness to the necessity of paying attention to this issue and for behavioral changes. As tackling [Air Pollution](#) and its causes grows ever more popular, so does the political weight associated with the subject, which in turn results in an increased number of measures destined to improve air quality. However, effective actions against [AP](#) require the approach to be intelligent and knowledgeable, for the more we know, the better we can handle it. It is thus the role of technology and technologists, to develop new ways in which to measure, map, track and trace [AP](#), leveraging the power of human intellect and ingenuity to combat this impending threat that is upon us.

## 1.3 Literature review

### 1.3.1 Tomography

Tomography is the cross-sectional imaging of an object through the use of transmitted or reflected waves, captured by the object exposure to the waves from a set of known angles. It has many different applications in science, industry, and most prominently, medicine [22]. Since the invention of the [Computed Tomography \(CT\)](#) machine in 1972, by Hounsfield [37], tomographic imaging techniques have had a revolutionary impact, allowing doctors to see inside their patients, without having to subject them to more invasive procedures [46].

Mathematical basis for tomography were set by Johannes Radon in 1917. At the time, he postulated that it is possible to represent a function written in  $\mathbb{R}$  in the space of straight lines,  $\mathbb{L}$  through the function's line integrals. A line integral is an integral in which the function that is being integrated is evaluated along a curved path, a line. In the tomographic case, these line integrals represent a measurement on a ray that traverses the [Region Of Interest \(ROI\)](#). Each set of line integrals, characterized by an incidence angle, is called a projection (see Figure 1.1). To perform a tomographic reconstruction, the machine must take many projections around the object. To the set of projections arranged in matrix form by detector and projection angle, we call sinogram. All reconstruction methods, analytical and iterative, revolve around going from reality to sinogram to image [10, 46, 42, 40, 41, 24].

There are two broad algorithm families when it comes to tomographic reconstruction, regarding the physics of the problem. It can involve either non-diffracting sources



Figure 1.1: A schematic representation of a projection acquisition. In this image, taken from [41], the clear line that comes down at a diagonal angle is a projection.

(light travels in straight lines), such as the X-Rays in a conventional [CT](#) exam; or diffracting sources, such as micro-waves or ultrasound in more research-oriented applications [46]. In this document, I will not address the latter family, since I will not be applying them in my work.

In any tomographic procedure, the first step is to gather information from the target object. The first concept one requires for this is to determine the problem's geometry. There are many different possible geometry, however, there are two that are more important for this thesis: parallel and fan-beam geometries. In the parallel case, there are as many light sources as there are detectors. Light travels between the source and the detector in straight lines, and the whole set rotates around the object's location. Fan-beam geometries are characterized by having only one light source which rotates around the target object. In this geometry, a set of detectors are placed on the other side of the object, and the lines (rays) between the source and the detectors describe a fan, thus the name of the technique [41, 46].

As far as algorithms are concerned, there are two main types: analytical and iterative. The first family includes the most famous algorithm for these applications, the [Filtered BackProjection \(FBP\)](#). Iterative algorithms work by iteratively searching for a solution to the reconstruction equation, which is basically an underdetermined system of equations (far less equations than unknowns). There are numerous algorithms that work in this way, but in my work, I have identified three that are extensively used, both in the field of atmospheric tomography and in medicine: [Algebraic Reconstruction Technique \(ART\)](#), [Simultaneous Algebraic Reconstruction Technique \(SART\)](#), and [Maximized Likelihood Expectation Maximization \(MLEM\)](#). The simulator that was developed as part of this project uses the last two and [FBP](#). All these techniques are further discussed and presented in Chapter 2.

### 1.3.2 DOAS

Since the beginning of the 20<sup>th</sup> century, scientists have been using spectroscopy to measure reactive trace gases in the atmosphere, especially ozone. The basis for these applications were set by Bouguer, Lambert and Beer, which have separately presented the law (Lambert-Beer's) that determines the relationship between light extinction and the concentration of an absorber, when it must traverse a medium in which this absorber is present. DOAS is one of the methods that is applied for this purpose. It was developed in 1976, by Perner and his colleagues [64], to detect and quantify the hydroxyl radical in the atmosphere. The book by Jochen Stütz and Ulrich Platt [65] is considered by most researchers one of the most important references in the field and is present in most bibliographies of the literature in this subject (it is also one of the main references in this thesis). Platt, in particular, has been working with the technique since its beginning, as one of the elements of Perner's team that published the article about the hydroxyl radical mentioned some lines above [64].

Besides DOAS, Lambert-Beer's law is the basis of many quantitative spectroscopy applications. However, most of these techniques are used in a laboratory context, in which conditions are controlled and very well known. Atmospheric studies do not have this luxury. In the open atmosphere, there are a number of factors, like Mie and Rayleigh scattering, atmospheric turbulence or thermal fluctuations in the optical path that make outdoor spectral measurements more complicated. DOAS is able to circumvent these difficulties by measuring differential absorptions, which is to say the difference in absorption between two different wavelengths [65, 55].

There are two modalities for DOAS experiments, Active and Passive, which differ mainly on the use of artificial or natural light sources, respectively. Both methods have their advantages and disadvantages. Active systems are more similar to a bench spectroscopy experiment. Conditions are more controlled (starting with the light source) and therefore, results are usually more reliable and precise, not to mention simpler to reach, since there is no need to account for complex physical phenomena, like radiative transfer [65]. However, these systems do require additional material, and many times entire infrastructures have to be built around them [68]. Passive systems, on the other hand, can be comprised of just a computer, a spectrometer and a telescope, making them instrumentally much simpler than their active counterparts. This flexibility also comes with the possibility to develop new interesting sub-techniques, like MultiAxis-DOAS (MAX-DOAS), which allows (for instance) the determination of the stratospheric contribution of a certain trace gas (in opposition to its tropospheric contribution). The mathematical processing of the acquired spectra, nonetheless, is much more complex.

### 1.3.3 DOAS Tomography

DOAS tomography is a relatively new subject within the realm of DOAS. It consists in the application of tomographic methods to reconstruct a two-dimensional or three-dimensional *map* of the concentrations of trace gases in study. The seminal paper that originated this and other remote sensing tomographic techniques was published by Byer and Shepp in 1979 [13]. It is not by any means a very populated literary space. In a systematic review that was performed as part of a course I took during

the development of this PhD thesis (see Section 2.5), I managed to identify a total of 13 papers that were clearly about DOAS tomography. In doing this review, I have also found that the largest DOAS tomography study was performed in Germany, during the first years of the 21<sup>st</sup> century. This research campaign, called BAB-II [51], aimed to measure and map traffic-related concentrations for NO<sub>2</sub> in the motorway that goes between Heidelberg and Mannheim. A more recent effort that is mention worthy is the paper by the Stutz [79], in which the group created a tomographic system that was able to perform as a fence line monitor for a refinery in Houston, Texas. In between the two studies, and right after BAB-II, Erna Frins published her paper [32], in which she described the use of a MAX-DOAS system alternately pointed towards sun-illuminated and dark targets in a tomographic manner.

Besides the birds eye view of the literary panorama of the DOAS tomography field, this systematic review allowed me to understand two important gaps in the technology being employed for this research. The first is that all of the studies that were featured in my review used a very low number of tomographic projections (some dozens of line integrals). This is a problem because it is the single most important factor for the resolution of any tomographic procedure, and although resolution is not an absolutely critical factor in atmospheric analysis (because the sizes of the target objects - gas plumes - are very large and diffuse), it is an important system feature that should be improved. Moreover, the second important pattern that was clear from my research was that all but one of the described systems were fixed, and the one that was mobile was composed of a minimum of two spectral acquisition devices and had one of the lowest numbers of projections in all papers. This is a very important gap. DOAS tomography has the ability not only to measure but also to map pollutant concentrations and can be an invaluable technique in the fight to understand and track the movement of pollutant plumes, but the fact that the available systems require dedicated infrastructure to operate and have no mobility at all may be the most important factor leading to the almost non-existing investment DOAS tomography systems.

More than half of the world's population is expected to be living in cities by the year 2050, and in the next 10 years we will see an increase in the number of so-called mega cities of more than 30% [14]. This puts a lot of pressure on governmental agencies and municipalities (specially in the West) to "smarten up" their urban infrastructures, so that cities can harbour their inhabitants with reasonable quality of life for everyone. In fact, a recent report by Organisation for Economic Cooperation and Development (OECD) concluded that in 2010, estimated costs due to AP were around 1.7 trillion American dollars, just in OECD countries. The flexibility and mobility that the system I am developing brings to the table are two very heavy points in its favour as a pollution mapping tool which is unobtainable with the traditional methods, whether *in-situ* or remote.

## 1.4 Research Questions

In Section 1.1.2, I have introduced the reasons which led NGNS-IS to pursue the development of an atmospheric monitoring system, and that what set it apart from other systems was the ability to spectroscopically map pollutants concentrations using

tomographic methods, thus defining a primary objective for this thesis.

Two secondary objectives were born from the necessary initial research, which had a very heavy influence over the adopted methods:

- To use a tomographic approach for the mapping procedure;
- To ensure the designed system would be small and highly mobile;
- To use a single light collection point, minimizing material costs.

Taking all the above into account, we arrive at the main Research Question ([Research Question \(RQ\)](#)), presented in Table [1.1](#).

Table 1.1: Main research question.

---

<b>RQ1</b>	<i>How to design a miniaturized tomographic atmosphere monitoring system based on DOAS?</i>
------------	---

---

This is the main research question. It gave rise to four other more detailed research questions. These secondary questions allow a better delimitation of the work at hand and are important complements to RQ1. This questions are presented in Table [1.2](#).

Table 1.2: Secondary research questions.

---

<b>RQ1.1</b>	<i>What would be the best strategy for the system to cover a small geographic region?</i>
<b>RQ1.2</b>	<i>What would be the necessary components for such a system?</i>
<b>RQ1.3</b>	<i>How will the system acquire the data?</i>
<b>RQ1.4</b>	<i>What should the tomographic reconstruction look like and how to perform it?</i>

---

## 1.5 Hypothesis

As stated in Section [1.4](#), the main goal of my work was to provide an answer to the question of how to design a miniaturized tomographic atmosphere monitoring system, based on [DOAS](#). This sentence is the most important point of the project. Every development from this point forward stems from it and is motivated by it. It also requires some deconstruction in order to understand the true scope of the matter. First, it is a miniaturized device. This means that besides all the habitual requirements (performance, function, adequacy, compatibility with the other components, safety and security) in defining components in an engineering project, one must also keep in mind the footprint of each component, and how much it weighs. Second, it is a tomographic system, which means that not only the device must be able to take line integrals from some kind of medium, it must also be able to describe a predefined trajectory, with admissible levels of geometric error, which complies to a certain projection geometry. Otherwise, one would not be able to apply a tomographic reconstruction routine to

obtain the map of the target species concentrations. Finally the system is supposed to monitor the atmosphere in some way. Now, as implied in the same sentence, **DOAS** is the technique that I am trying to apply in this system. But as I point out in Section 1.3.2 and with more depth in Section 2.2, there are two families of **DOAS**, and within them, many sub-techniques. This system which I am developing is based on the hypothesis that we can use an almost hybrid approach to **DOAS**: passive **DOAS** instrumental simplicity and active **DOAS** retrieval simplicity. One could use a scattered sunlight measurement as a light source for a **DOAS** analysis, provided distances between the two points are kept small, optical densities are low (clear atmosphere), and both spectral measurements are taken in the same angle. With this process, we would only effectively be using as projections the spectral measurements of the **ROI**. This hypothesis, while not being mentioned in the library directly, has already been hinted at in several papers, namely references [32, 16, 45].

## 1.6 Methods and Findings

The **Research Question** were used to guide the conduction of this thesis' work. This has led to a natural two side division: on the one hand, there was the need to algorithmically define projections for tomographic reconstruction of a trace gas concentration field; on the other hand, physical tests had to be conducted to ensure that the idealised projections were feasible. These were the two hypothesis that had to be verified.

The first hypothesis was addressed by the construction of a software simulation system based on several projection and backprojection matrix operators. This system is based on one of the main novelties involved in this project: a high degree of geometric measurement freedom. This is achieved by assuming that our tomographic acquisition system is mounted on a custom-built **UAV**, which carries specific spectroscopic equipment and is programmed using ArduCopter's SITL software suite [**arducopter**] for full autonomous operation. Spectral acquisition takes place using a set circular trajectory that implies the acquisition of a higher-than-usual projection number in comparison with traditional DOAS-tomography operations. After simulating the spectral projection information, according to a number of parameters that are input at runtime, the system calculates their backprojection and assembles a simulated concentration map for the selected trace gases.

The second hypothesis is addressed by means of the physical acquisition of spectral data between two relatively close points in Almada, Portugal. By comparing spectral information retrieved by two different sets of equipment in said geographical points, we should be able to establish that current day equipment is able to measure trace gas concentrations in this kind of distances and that it is possible to make these measurements through the difference of two passive **DOAS** measurements.

## 1.7 Layout

After this introduction, in Chapter 2, we can find a more thorough literature review than the one presented in Section 1.3. After that, I have included the chapter in which I present the methods employed in this project's development (Chapter 3), and discuss

them in Chapter 4. Finally, in Chapter 5, I present what could be concluded as a result of this project and some of the future developments that might be pursued.

## LITERATURE REVIEW

### 2.1 Air Pollution

Daniel Vallero, in his book "Fundamentals of Air Pollution" [84] makes a very important observation: Air Pollution has no universal definition. Its meaning is intertwined with the context with which it is measured and observed, with the ecosystem in which it is perceived and even with the pollutant concentration (not every toxic compound is toxic at every concentration). The [Environmental Protection Agency \(United States\) \(EPA\)](#) defines Air Pollution as the following:

*Air Pollution is the presence of contaminants or pollutant substances in the air that interfere with human health or welfare, or produce other harmful environmental effects.*

He then analyzes this definition through two possible lenses, the one that comes with the interference produced by air contaminants; and the one that comes from the harm they may cause. He notes that both points of view come with a heavy burden of ambiguity, incompatible with a scientific definition. We can thus observe that preferable to address the issue through its measurable effects and consequences. These are well-established and well known, and scientists all around the world have been publishing extensively about them for some decades now. The correlation between Air Pollution and an increased mortality in heavily industrialized areas was first established in Europe, in the 19<sup>th</sup> century, but the first time it was taken seriously was during the 1952 killer-smog incidents, in London [65]. At the time, a combination of very cold weather, an anticyclone and fireplace emissions caused a thick smog to fall over London, directly causing thousands of deaths and indirectly many more [5, 61]. The disastrous consequences of this incident had a huge impact in the civil society, resulting in a series of policies and laws, among which the Clean Air Acts of 1956 and 1968, which are broadly considered to be some of the first actions to decrease pollution in human societies. Much work has been done, and it has resulted in remarkable progress since the definition of those two policies. We are in fact in a much better place than we were some years or decades ago, but pollution is still a part of everyday reality for the whole of civilization. In the current day and age, both European and American regulatory and surveillance bodies (the [European Environmental Agency \(EEA\)](#) and the [EPA](#), respectively) have identified a group of six *criteria pollutants* that need to be monitored effectively.

### 2.1.1 Criteria Pollutants

Description of criteria pollutants and an explanation of their chemistry and atmospheric cycles.

### 2.1.2 Air Pollution Effects on Human Health

Arguably, there is no medium in which it is more important to consider AP by its effects than in the human body. However, even this has its caveats. The body's response to any given substance changes with the dose that is administered to it, something which has been known to us for centuries:

*What is it that is not poison? All things are poison and nothing is without poison. It is the dose alone that makes a thing not poison.*

– Paracelsus

This quote, originally in the writings of one of the fathers of modern medicine, the Swiss Paracelsus, was taken from Patricia Frank's book called *The Dose Makes The Poison* [31] and is one of the core tenets of toxicology even today. There are, however, some substances which do not need anything close to a high dose to cause harm to human health, and in general, atmospheric pollutants fall in that category. According to the EEA, heart disease and stroke are the most common causes of premature death due to Air Pollution. The same organization states that the most prominent atmospheric pollutants in terms of the effects they have on human health are PM, NO<sub>2</sub> and Ozone (O<sub>3</sub>) [27, 26]. In this thesis, I will focus mostly on them, not only because of their health importance, but also because of their spectral nature, which allows us to detect them using DOAS [65]. Of course, a complete description of how AP affects the human body is a colossal task which is well beyond the scope of this thesis. Therefore, I will focus my attention on the more prominent symptoms that are results of these chemicals: respiratory syndromes, cardiovascular diseases, problems during gestation and finally, neurologic consequences of AP.

#### 2.1.2.1 Respiratory effects of Air Pollution

The respiratory system's main functions are the delivery of oxygen into the blood stream and the removal of carbon dioxide from the body. Air enters the body from the upper airways and flows to the alveolar region, where oxygen diffuses across the lung wall into the blood stream, from which it is transported to the tissues where it diffuses yet again and is made available to the mitochondria in the cells, that use it for cellular respiration [58]. The whole system is in permanent interaction with the atmosphere, and is therefore exposed to all kinds of air pollutants and trace gases, and therefore it is only natural that respiratory effects are among the most direct health complications originating in AP [84].

The region in which a given pollutant is, within the respiratory system (see Figure 2.1), is of great importance. After the air is inhaled through the nose, the air is heated or cooled to body temperature, as well as humidified, in the upper airways. The trachea leads the air into the bronchi, where flow is divided several times before reaching the alveoli, where oxygen is supposed to enter circulation. Since air flows within

## CHAPTER 2. LITERATURE REVIEW

---

the different regions of the pulmonary system are completely different, AP is also handled differently among them. Moreover, it is also important to consider that pollutants also vary according to their own physical properties, and pollutant absorption is also a function of this. Particles' absorption depends on their aerodynamic characteristics, as well as soluble fraction and density. Gaseous pollutants are dependent exclusively on their vapor pressure, solubility and density [58, 84].

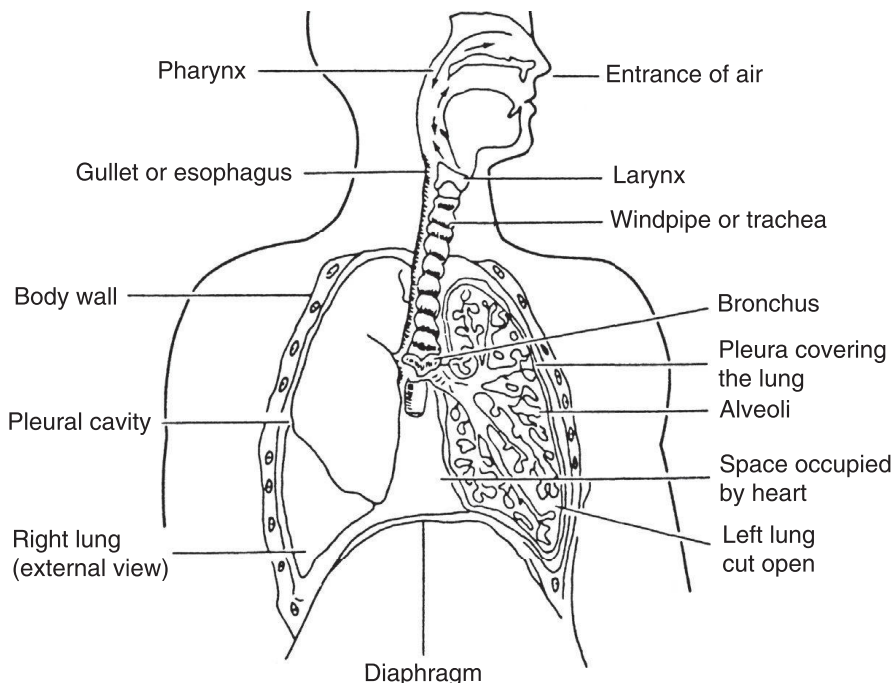


Figure 2.1: Annotated anatomy of the respiratory system [84].

The respiratory system has several (imperfect) mechanisms in place to prevent particles from reaching the blood stream. Larger particles are deposited in the nose, by impaction on the hairs and bends of the nose. Smaller particles are immune to this first barrier, and manage to get to the trachea and bronchi, where they are filtered also by impaction, this time on the walls of the innumerable bifurcations of the bronchial tree. The smallest particles are removed through Brownian motion, which ends up pushing them against the alveolar membrane. Deposited substances are then removed through the action of cilia in the pulmonary system's walls or by coughing, sneezing or blowing one's nose [84].

While the body is quite efficient at filtering out particles from the respiration process, the same cannot be said about gaseous pollutants. Removal of these compounds can only be achieved through absorption, which depends almost exclusively in the gases' solubility. High solubility compounds are absorbed directly in the upper airways ( $\text{SO}_2$ , for instance), while less soluble gases (such as  $\text{O}_3$  and  $\text{NO}_2$ ) are absorbed in the lungs themselves. Irritant gases trigger a variety of responses, in which one can include sneezing, coughing or bronchoconstriction. These gaseous compounds are then diffused through to the bloodstream or the lungs themselves try to convert them into other substances via biochemical processes. In some cases, this attempt to detoxify a pollutant can lead to much more problematic circumstances. For instance, the lung is

known to active procarcinogens, substances that are only carcinogenic after being metabolized in a certain way [84].

Acute symptoms of AP exposure are very varied, and range from mild irritation to complete respiratory failure, depending mostly on level of exposure and individual sensitivity to the chemical compound. One of the most important acute manifestations of AP exposure are encompassed within the **Acute Lower Respiratory Infections (ALRI)** group. There are several studies in which the relationship between this issue and AP is deducted and explained, mostly in developing countries, and it remains as one of the major causes for infantile death [14, 82]. Children are one of the most affected demographics by AP [27], and one of the chief reasons for this is that the human respiratory system is till developing in this stage of life.

In a 2016 review [34], the authors searched the literature for childhood adverse effects of AP, with a particular focus on respiratory problems. They have found evidence for a number of respiratory complications and diseases that were previously reported in the literature caused or exacerbated by AP. Effects are many, and vary immensely in nature, severity and affected populations. Short term effects, like coughing and wheezing were found for the three types of major pollutant and several others; several papers mention an association between the occurrence of respiratory infections and exposure to AP, namely concerning PM and NO<sub>2</sub>. The same review found reports of decreased lung function in children and asthma exacerbation in children due to Air Pollution. Moreover, a person exposed to high levels of AP during childhood are also more likely to develop syndromes like **Chronic Obstructive Pulmonary Disease (COPD)**, and to have exacerbated symptoms of this disease. Finally, and perhaps more concerning, the carcinogenic nature of several of the constituents of AP leads to findings relating the appearance of respiratory cancers to exposure levels during childhood. Many of the conclusions of this review come from a large-scale European effort called **European Study of Cohorts for Air Pollution Effects (ESCAPE)**, that intended to investigate long-term health effects of AP in Europe. ESCAPE was an European Union's Seventh Framework Programme (FP7) initiative that ended in 2014.

### 2.1.2.2 Air Pollution and cardiovascular issues

After being absorbed by the respiratory system, oxygen is distributed to all cells of the body through the cardiovascular system. Air pollutants, like particles and trace gases, are also capable of penetrating the lung barrier and therefore share the same fate. There are several pathways with which AP and negatively affect the cardiovascular system. The most immediate of which is probably an imbalance in the **Autonomic Nervous System (ANS)** caused by direct inflammation and oxidative stress in the respiratory system. The second most immediate pathway is systemic inflammation caused by Air Pollution. Finally, soluble AP compounds in the bloodstream also contribute to **Cardiovascular Disease (CVD)** by increasing inflammation and oxidative stress in the cardiovascular system [9, 84].

The link between Air Pollution and cardiovascular effects started being made during the twentieth century, given a series of incidents (like London's 1952 killer-smog) that happened in the urban areas of industrialized countries. Nowadays, **Cardiovascular Mortality (CVM)** has been shown to be intricately connected to AP. In fact, in a

2013 review indicated that an annual increase of  $10\mu\text{g}/\text{m}^3$  in fine PM and NO<sub>2</sub> led to an increase of 11% and 13% respectively in terms of CVM and premature atherosclerosis, in spite of absolute AP concentrations were maintained below the European policy-recommended thresholds. Road traffic exposure studies have reported similar findings, with subjects having increased coronary calcium scores [7].

Arrhythmia is one of the other cardiovascular issues that might be caused by AP. There is still some debate regarding whether or not there is a causal relationship between the two, but there have been several studies in which increased levels of Air Pollution were correlated with arrhythmia-related hospital admissions. Moreover, there seems to be a correlation between low heart rate variability and AP, which is considered a marker for ANS imbalance and an important risk factor for CVM[7].

The risk of stroke is also clearly exacerbated by the presence of increased levels of AP. In fact, it is currently thought that AP is responsible for about 29% of the burden of stroke, globally. Studies have shown that an increase of  $5 \mu\text{g}/\text{m}^3$  in the annual PM<sub>2.5</sub> concentration leads to a remarkable 19% increase in the risk of stroke, which was found to be more significant in non-smokers. A positive correlation was also found between gaseous pollutants (NO<sub>2</sub>, CO and SO<sub>2</sub>) concentration and the risk of stroke or stroke mortality.

Short term effects of AP on the cardiovascular system seem to be predominantly the triggering acute coronary incidents. For instance, a positive correlation was found between short term increases in AP and non-fatal myocardial infarctions.

### 2.1.2.3 Gestational and developmental complications

Mammals are in their life's most vulnerable stage while they are still developing inside their mother's womb. This is the time when there is a greater rate of tissue expansion and creation, creating an enormous need for nutrients. These are supplied by the mother's blood, crossing the placenta and reaching the fetus through its umbilical cord. High rates of tissue formation and proliferation render the forming being unstable and therefore more susceptible to the appearance of some kind of morphological abnormality. At this time, there is no separation between the mother's blood and the fetus, meaning that whatever chemical reaches the progenitor's bloodstream also reaches the growing fetus. If the mother is exposed, so is the fetus [84].

There are numerous chemicals that can affect the female reproductive system, of which some are habitual components of AP. They have been associated to several highly adverse affects, and interfere with such things as the processes by which the body is able to produce eggs, or other processes that enable the formation of a single cell by the union of the sperm and the egg (the zygote). After conception, AP has been known to reduce uterine nurturing capabilities, and hinder the new being's development. Some of them are even teratogens, meaning that they induce birth defects. Figure 2.2 illustrates the kind of defects that come with exposure, according to the time at which the mother was exposed.

There are already several studies that correlate higher AP exposure levels to birth defects or the probability of negative outcomes. For instance, in [53], researchers have studied the association between AP exposure levels (for the mother) and the appearance of premature Small for Gestation Age (SGA) by collecting more than 40000 births

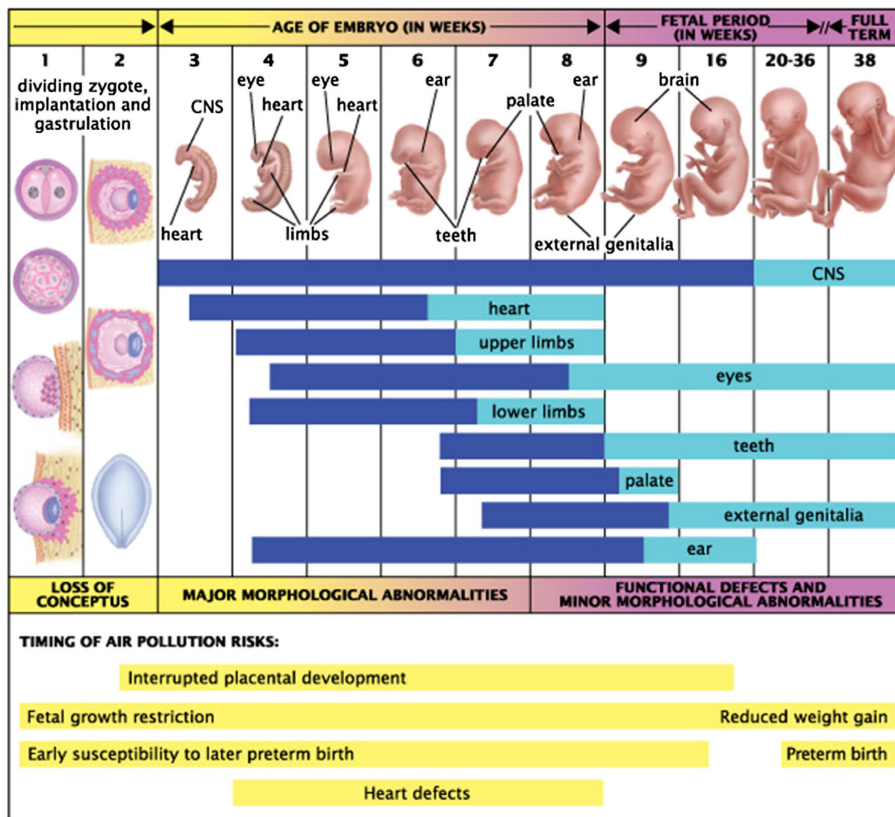


Figure 2.2: Possible abnormalities caused by AP exposure *in utero*. Notice that time of exposure is of critical importance [84].

in Changzhou Maternity (China) and studying the mother's typical environment. This study has found a positive association between SGA and exposure to PM<sub>2.5</sub> in two or three pollutants models of AP (with NO<sub>2</sub> and Sulfur Dioxide (SO<sub>2</sub>)), during the third trimester of gestation. Another, perhaps more comprehensive study, was performed using Swedish data from 1997 to 2007, and found that there was a positive association between O<sub>3</sub> exposure and the appearance of pre-eclampsia (a potentially deadly complication of pregnancy), estimating that about 1 in 20 pre-eclampsia cases were caused by AP [62].

Besides uterine development compromises, birth defects and reproductive difficulties, Air Pollution has also been associated with hindrances to the child's neurodevelopment. In a New York study was able to associate lower levels of mental development at age 3, in African-American children with valid prenatal Polycyclic Aromatic Hydrocarbons (PAH) exposure data. In another study from the neighboring Boston, AP was associated with generally lower cognitive test scores, even when correcting for several influencing factors. On a different level, AP was shown to produce significant delays in the central conduction times of Brainstem Auditory-Evoked Potentials (BAEP) tests in children, indicating that there might be important repercussions of AP to vestibular and auditory development.

Although most other systems are affected by AP, it does have a particularly heavy

toll on the respiratory development. This is because the lungs are not completely developed at birth, and are only finished in the late teens. The level to which AP affects the respiratory system development varies greatly with the stage of life in which the effect is produced, and severity is also very varied. Acute negative effects range from respiratory death to chronic cough [84]. Moreover, childhood (and prenatal) exposure to AP has been associated with the emergence of conditions such as COPD and asthma.

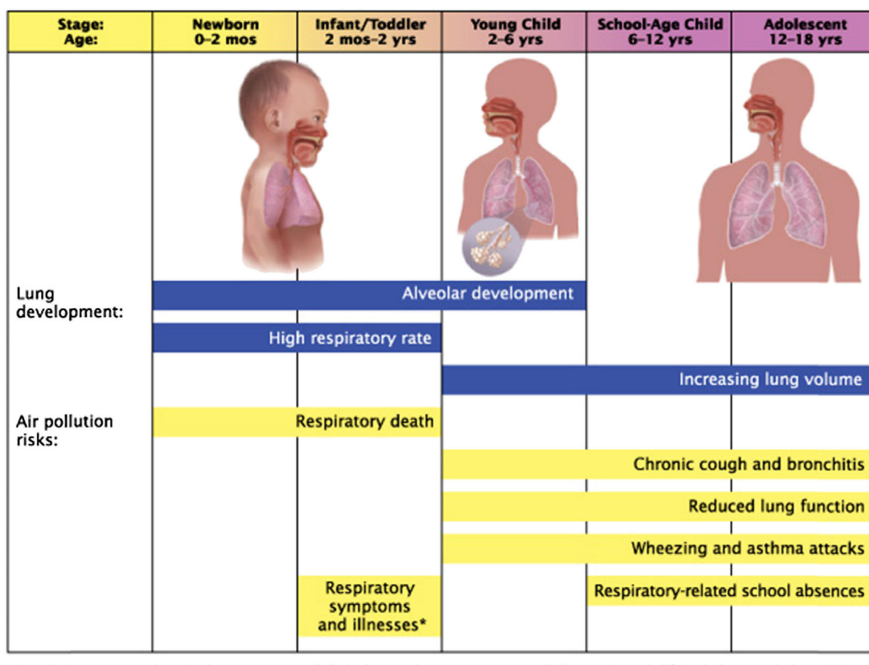


Figure 2.3: Developmental stages of the lung throughout life vs the risks of AP exposure in each stage [84].

#### 2.1.2.4 Neurological disorders

The brain and the Central Nervous System (CNS) were one of the last to be included in the range of organs that are affected by AP. While the effects of AP on the respiratory and cardiovascular systems are quite broad and include some "surprises", the fact that these systems were affected by Air Pollution was evident and expectable, given the type of exposure these systems endure. The CNS, on the other hand, has a more difficult to express relationship with AP, and has required more sophisticated methods to detect [84, 33]. It was in the beginning of this century that the first connections between AP and the emergence of neurological disorders started to be made, and from then on, we have progressed into thinking that not only are they related, but also that AP might be one of the key driving forces in the onset of certain neurological diseases, including the most dreaded of them all, Alzheimer's and Parkinson's [33, 23, 15].

The reason why AP is able to reach and damage the CNS is a continuation (or even an extension) of the ways in which it affects the cardiovascular system. By crossing the alveolar barrier into the bloodstream, AP acts as an oxidative stress source. As

it can also do in lung tissue, **Air Pollution** creates some local proinflammatory effects in the cardiovascular system, affecting the vascular endothelium cells. This can lead to a systemic inflammatory status, which is accompanied by the production of proinflammatory cytokines (a type of message-protein that is used by organisms to trigger certain types of response, like inflammation [91]). Now, since blood vessels in the brain are extremely responsive to this kind of message, their presence can activate cerebral endothelial cells and disrupt the blood-brain barrier [33].

In 2018, a consortium of several Spanish universities and researchers wrote a review detailing the until-then-published articles dealing with the neurological implications of **AP** [23]. This review identifies several articles that connect the long-term exposure to **Air Pollution** with adverse impacts on the brain and brain structures. *In vitro* and *in vivo* studies, focusing on traffic related emissions and their effect on gray matter cells, have found that these display significant alterations. On other studies identified by the review, it was shown that white matter, the myelinated part of the brain, is particularly sensitive to **AP** and its volume is significantly decreased both in the elderly and children, as consequence of prolonged exposure to it.

There are also several articles that show that there is an association between exposure to air pollutants and impairments on brain function. In Section 2.1.2.3, I have already mentioned a study that was conducted in New York, and that found that the children that they were using as subjects were found to have measurable cognitive deficits in comparison with children of the same age living in less polluted areas which are compatible with the affected areas of the brain that were detected through neuroimaging studies [23].

### 2.1.3 Air Pollution effects on ecosystems

The Earth is home to an almost unbelievable number of different ecosystems. The ubiquitousness of **AP** means that all of them are in some way or another affected by this problem. In general terms, the threat posed by **AP** to any given habitat is a function of its biodiversity, defined as the number of different living beings that inhabit a certain environment (in all biological kingdoms) [63]. Living beings within an ecosystem are like nodes in a graph, with many connections to any particular node. More biodiversity corresponds to a greater number of nodes and an even larger number of links, which means that there is a greater probability that some of those links become disrupted by **Air Pollution** in some way.

Water based environments are greatly affected by **AP**. Material deposition on the surface of the water can have serious consequences in terms of habitat conditions for holding life. In this regard, the most important air pollutants are **NO<sub>2</sub>** and **SO<sub>2</sub>**, which significantly decreases the water's pH. On its own, this represents a major problem. The acidifying effects of nitrogen and sulfur deposition became very pronounced in Scandinavia (among other places). Thousands of this territory's lakes, once teeming with wildlife, became effectively lifeless. Those that did not reach this point, have seen the number of fish living on their waters dwindle to numbers from which there may be no return [88]. Sulfur and nitrogen depositions also enrich surface waters, altering the solubility and other physical aspects on the surface of the water, which in turn inevitably leads to disruptions in species abundance and diversity. Moreover, indirect

effects may also take their tolls. For instance,  $O_3$  does not play any significant role in the chemical behavior of a water body, but it can influence the number of predators around this habitat, which will compromise the predator-prey balance of the aquatic environment [84, 54].

In terrestrial ecosystems, AP effects are not smaller in importance or complexity, and they are different for each type of being. To the Flora, AP can have a subtle to deadly effect, depending on variables like pollutant chemical species, exposure time, or plant life stage in which exposure happens. For instance,  $O_3$  is especially poisonous to plants. Even small concentrations of this gas will cause plant growth to decrease significantly. It enters the plant through the stomata and reduces photosynthesis through increased oxidative stress. Many times, although concentrations are not enough to outright kill the plant, they are enough to make them more susceptible to other attacks like pathogens, insects or environmental conditions. Ozone is commonly responsible for huge financial losses that come from the diminished agricultural yields. And while it is true that due to several policies, AP is in a clear downward trend since the 1980s in urban regions, it is also true that in many rural areas, these changes have been smaller or non-existent, making these losses even more relevant [54, 84].

Forests are among the most susceptible environments to AP. They suffer from the previously described mechanisms of AP damage, like acidic deposition, but also suffer from other, less direct pollution risks. Emission of greenhouse gases can induce changes in humidity, temperature, and general climate profile of a forest. The combination of direct and indirect risks result in an exacerbation of both, leading to more and more forest losses due to Air Pollution. The damage done to forests all around the world is especially problematic given the biodiversity that these ecosystems contain within themselves. Rainforests in particular are thought to contain more than half of the world's terrestrial species. These species have many times adapted to a particular kind of microhabitat which only exists in the specific rainforest in which it lives. Changes in these specific conditions, whether caused by Air Pollution or any other cause, are leading to alarming extinction rates in forests and rainforests globally [84, 54].

Of course it is not only the flora that suffers with Air Pollution. Direct implications of AP on animals approximate those that fall upon humans. We are an animal species, after all. Our main difference is the adaptation capabilities that our superior intellect grants us, which allows us to escape more or less unscathed for a longer period of time, and to combat what we cannot escape from in ways which are simply unaccessible to other animal species. So, although AP has direct effects on all animals that are exposed to it, ecosystem damage and eventual destruction remains the most perilous factor for this biological realm [84, 54].

#### 2.1.4 Air Pollution Sources

There are almost as many AP sources as there are pollutants. The first major division between these sources is whether they are natural or anthropogenic. However, this separation is not always clear, as one source can lead to another and boundaries become fuzzy within their own context. The most prominent example of such is the case of accidental fires. While they are most of the times classified as a natural source of AP,

their origin lies most of the times in human activities. In this section, I will present a selection of the most important naturally occurring air pollutants and examples of how they have affected human lives throughout the times. The selection itself does not intend to be complete description of pollution sources, but rather paint a general picture of the subject.

#### 2.1.4.1 Natural Sources of Air Pollution

Although people, governments and institutions tend to speak far more seldomly of them than of their man-made counterparts, natural sources of air pollutant are not only abundant, but also important. One of the main natural sources of AP are volcanic eruptions. These phenomena are responsible for the emission of immense quantities of PM and gases such as SO<sub>2</sub>, Hydrogen Sulfide (H<sub>2</sub>S) and methane. Depending on the type of volcanic eruption, the emitted cloud of gas and PM can remain airborne for long periods of time, even disrupting modern life at times, namely in what concerns air travel. The last eruption to happen in Portuguese soil took place in the remote Azorian island of Faial. In September 1957, the Earth shook almost continuously for around two weeks. Finally, on the 27<sup>th</sup>, 100 m Northeast the Capelinhos islands, the sea was seen to boil and project vapor and volcanic material hundreds of meters into the air. In the following hours, the underwater volcano finally exploded, emitting large quantities of volcanic ash and gases into the atmosphere. The phenomenon lasted for more than a year, and the final ejection of lava took place in October 1958 (see Figure 2.4). The eruption had a significant social impact, in addition to its ecologic importance. In the end, 40% of Faial's population left the island as a result [84, 81].

Oceans are also a significant source of AP. Aerosol particles of salt are continuously emitted from these large masses of salt water, which damage many human created structures, namely metallic constructions. In certain parts of the world, another important source of Particulate Matter (especially because of its consequences in the inhabitants' daily life) are dust storms. The most famous of these events, and one of the most deadly storms in the recorded history of the US territory was the infamous *Black Sunday* dust storm. Starting on Palm Sunday, 14 April, this sky-blackening dust storm punished the peoples from the panhandles of Texas and Oklahoma, burying entire houses (see Figure 2.5) under the dust and destroying the livelihoods of thousands of Americans. Dust storms were an important part of the US history during the 1930s and led to the creation of the Soil Conservation Service, a branch of the US Department of Agriculture [84, 2, 72].

Fires are also one of the largest sources of natural air pollution in the world. The uncontrolled burning of organic matter that is a large forest fire creates a large quantity of air pollutants that range from smoke to unburned (or partially burned) hydrocarbons, nitrogen and carbon oxides, and ash particles. Besides the obvious dangers of this kind of burnings for human life and activities, forest fires can also cause indirect damages, such as disruptions in supplies and travel due to reduced visibility [84].

Trees and forests in themselves are also responsible for a certain quantity of air pollution. Although they have the main part in the carbon dioxide conversion into oxygen, through photosynthesis, plants and trees are still the largest emitters of hydrocarbons in the planet, as attested by the blue haze that is visible on top heavily

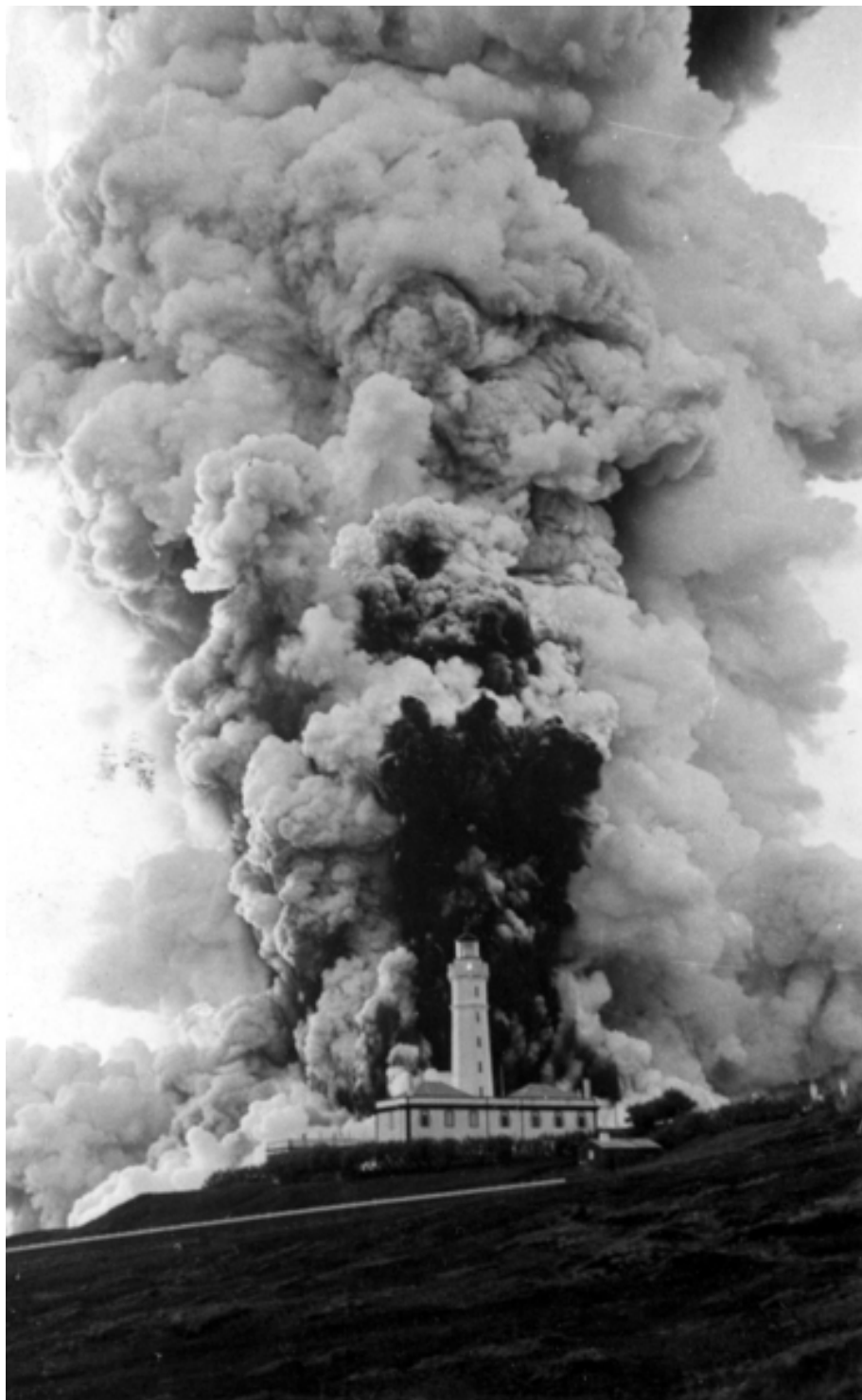


Figure 2.4: Dramatic photograph depicting the Capelinhos' lighthouse, half a kilometer from the eruption site, surrounded by a cloud of ash PM, volcanic gas and water vapor with more than 1km in height[81].



Figure 2.5: House almost completely buried by the Black Sunday dust storm. Several houses were entirely swallowed during this storm, trapping people inside, as if a big blizzard had hit them. Unlike a blizzard though, there was nothing anyone could do to keep the dirt outside, and all surfaces were covered black [72].

forested areas, resulting from chemical reactions between [Volatile Organic Compound \(VOC\)](#)s produced by the trees. This counter-intuitive fact was in the origin of the infamous Ronald Reagan speech in which he "blamed" trees for much of [AP](#), in a time when anthropogenic [AP](#) was at its apogee in the US and Europe. Plants are also the emitters of another kind of [PM](#), which is of particular importance both to themselves and humans, which are the pollens. This is a bio-aerosol - a type of aerosol that is or was part of a living being - associated with a number of diseases [84].

Finally, I will discuss Radon gas. This is a natural occurring radioactive gas that is part of the radiative decay of Uranium present in all rocks. Although chemically inert, Radon is radioactive and, as all radioactive substances, emits particles when it decays. Although present virtually everywhere, outdoor concentrations of Radon are typically too small to cause any problems. The problem with this gas comes essentially from indoor concentrations, namely at home. Being a gas, Radon is able to enter people's houses, exposing the inhabitants. Prolonged exposure to Radon gas is the second biggest cause of lung cancer and authorities estimate that between 3 and 14% of lung cancer cases are caused by this gas. In Portugal, Radon concentrations were found to be below the European prescribed limit in two thirds of the houses in a 2001 study, but in 17% of the cases, concentrations were not only above this limit, but also over the highest tolerable limit [84, 90, 67].

### 2.1.4.2 Anthropogenic Sources of Air Pollution

Air Pollution that originates from human activities is called anthropogenic. Since the first industrial revolution, mankind has been using more and more resources to fuel our progress and continuously improving way of life. Of course, the consumption of natural resources has some unpleasant and sometimes dangerous consequences. The most important of which, looking from the lens of this thesis, is the incredible increase in the levels of AP. If one had any doubts whatsoever, all it would take would be a look into the atmospheric CO<sub>2</sub> concentration chart (Figure 2.6) from a few centuries back to the current day to completely dissipate them.

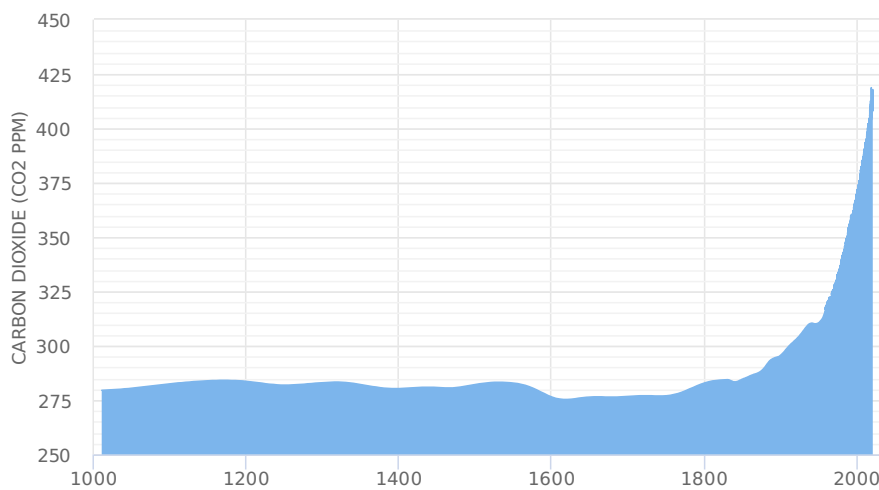


Figure 2.6: CO<sub>2</sub> atmospheric concentrations since the year 1000. Note the seemingly exponential increase since the 1800s. Plotted and published by the 2 Degrees Institute [1] with data from ice cores [29] and in situ monitors [80].

There are literally hundreds of sources of AP, but it is possible to categorize them into 4 main *families*: industrial processes, energy (includes transportation), agriculture and forestry, and waste. Of these 4 broad categories, as displayed in Figure 2.7. The most prominent is without a doubt the energy sector, although we also have to bear in mind that any and all combustion used in the other sectors is counted as energy production [44, 14].

From 2002 to 2011, fossil fuel combustion has been responsible for an average of 8.3 petagrams of carbon per year. This truly gigantic carbon footprint is in its majority explained by the worlds energy needs, which are ever increasing up to now. In 1990, total energy demand was situated at 356 quadrillion British Thermal Unit (BTU), having grown to 410 quadrillion BTU in 2010. In 2020, energy demand estimates are located at 600 quadrillion BTU, of which almost a quarter was expended by China [14].

It is important that we focus a little bit more on the Chinese case. It is now somewhat near commonsense to regard China as the factory of the world, and this of course is tied to Chinese energy consumption and production. On the same line of reasoning, this must mean that in some way, the country's energy expenditure is connected to the amount of financial resources that it produces, the GDP. Looking at the plots in Figure 2.8, one can see that all these numbers are highly correlated. When we ponder on the case of Chinese AP, and wonder why has this problem not been addressed

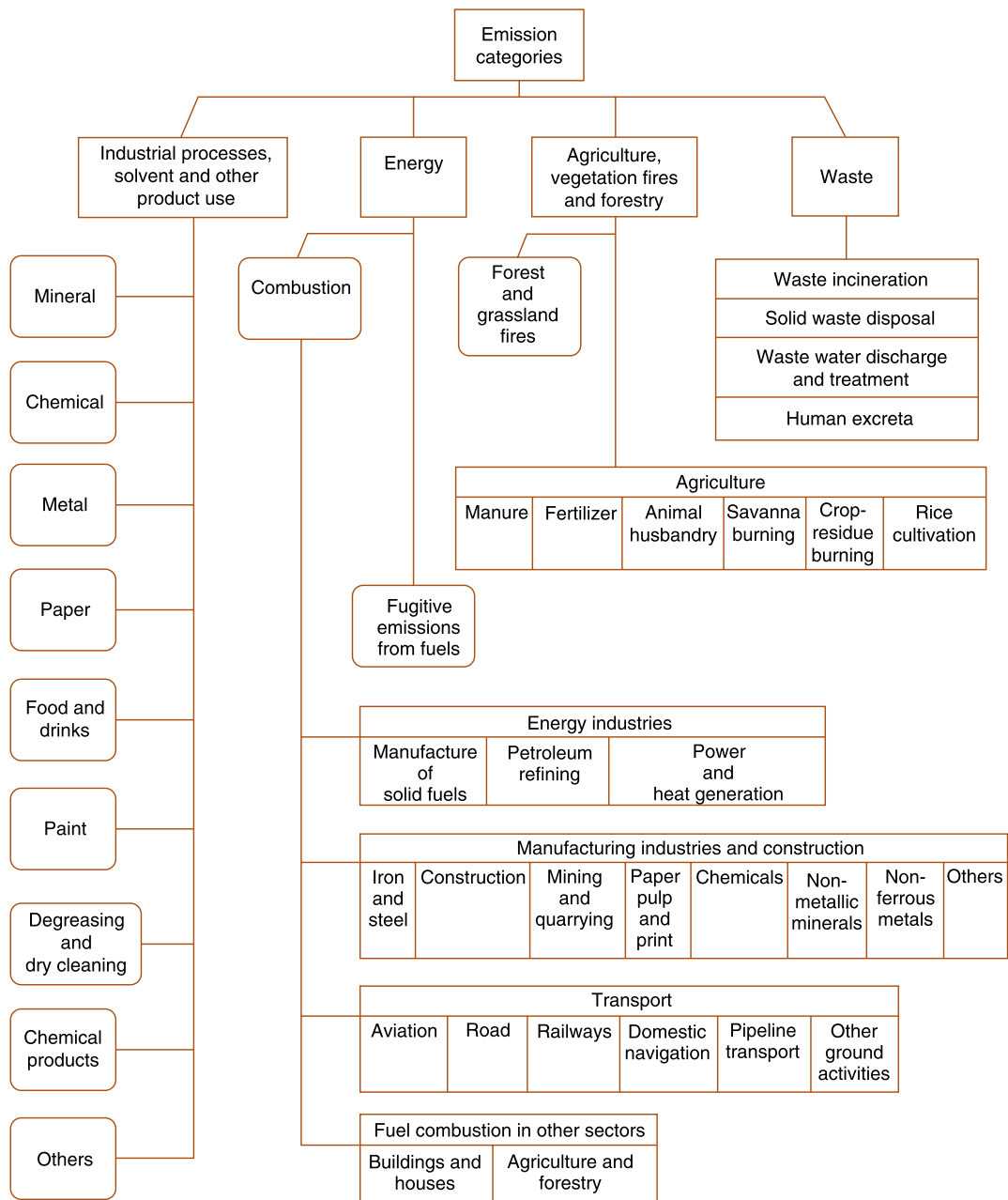


Figure 2.7: Schematic presentation on the sources of anthropogenic pollution and its categorisation according to the IPCC. Adapted from [14]

## CHAPTER 2. LITERATURE REVIEW

---

previously, given its imposing dimensions and growing importance, one must take into account that, given the indirect importance of AP on Chinese people's gains, it is highly likely that the country's governments will be reluctant to decrease it in any expedient form [14, 43, 89].

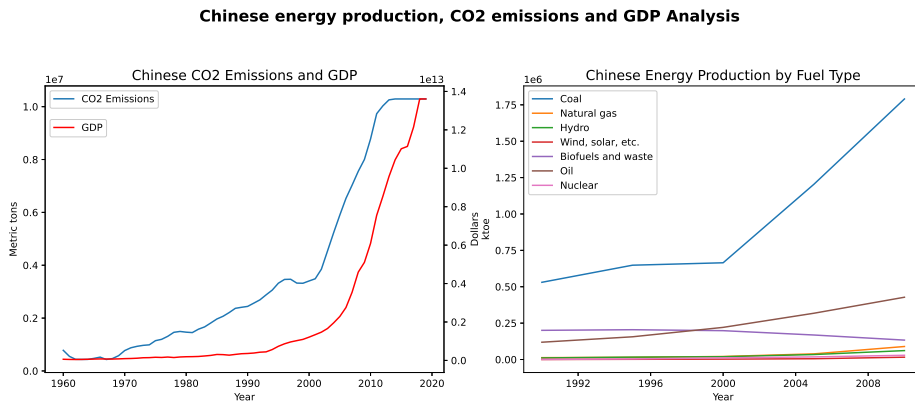


Figure 2.8: Chinese energy production, GDP and CO<sub>2</sub> emissions. Data collected from the World Bank and International Energy Agency websites [89, 43]

Another important conclusion that we can take from the plot in Figure 2.8 is that China has a large and historical dependence on the use of coal as fuel for energy production. This adds to the problem described in the above paragraphs, as coal is the single most damaging fossil fuel available. Not only does China get most of its energy from coal burning, but is also responsible for more than half of the world's production and consumption of this substance (see Table 2.1).

Table 2.1: Global energy production, divided according to the fuel used to obtain it and the production country.

Country	Liq. Fuel (M barrels / day)	Coal (BTU)	Nat. Gas (T cu. ft)	Renew. (BTU)	Nuc. (b kWh)
<b>China</b>	<b>10,6</b>	<b>80,6</b>	<b>5,1</b>	<b>10,6</b>	<b>93</b>
<b>USA</b>	<b>18,5</b>	<b>17,3</b>	<b>25,5</b>	<b>7,8</b>	<b>769</b>
<b>Europe</b>	<b>14,4</b>	<b>12,5</b>	<b>17,9</b>	<b>11,7</b>	<b>837</b>
<b>Middle East</b>	<b>16</b>	<b>0,1</b>	<b>14,8</b>	<b>0,2</b>	<b>1</b>
<b>India</b>	<b>3,6</b>	<b>12,6</b>	<b>2,1</b>	<b>3,5</b>	<b>30</b>
<b>Russia</b>	<b>3,4</b>	<b>4,5</b>	<b>15,7</b>	<b>1,7</b>	<b>166</b>
<b>Africa</b>	<b>3,5</b>	<b>4,3</b>	<b>2,7</b>	<b>4,7</b>	<b>12</b>
<b>Brazil</b>	<b>3,3</b>	<b>0,5</b>	<b>1,1</b>	<b>6,8</b>	<b>15</b>
<b>World</b>	<b>91,4</b>	<b>153,9</b>	<b>120,8</b>	<b>63,7</b>	<b>2345</b>

Internal Combustion Engine (ICE) are the single most important means for powering human transportation. Almost every vehicle in the world uses a kind of ICE. These motors operation is an application of the Otto cycle, in which the chemical energy in the fuel is converted to mechanical energy. These engines are as ubiquitous as the fossil fuels that have powered them since the beginning of the automobile revolution, in the early 20<sup>th</sup> century. Fossil fuels have several features that make them ideal to power our vehicles. Their energy density is high, they are incredibly safe to manipulate and use, and fossil fuel infrastructure can be found in almost every far

corner of the Earth. However, using them releases a number of gaseous and particle-condensed side products into the atmosphere, and this makes traffic one of the most important sources of AP. For instance, traffic pollution is the main responsible for human exposure to Nitrogen Oxides ( $\text{NO}_x$ ) gases. Without countermeasures, gasoline ICE equipping passenger vehicles emit around 1.8 g/km of these gases, while diesel emits 2.8 g/km and Liquefied Petroleum Gas (LPG) around 2.1 g/km. On heavy duty engines, like on trucks and tractors, these figures skyrocket to 14.7 g/km for diesel engines and around 5.1 g/km for LPG [14].

Energy production (including transportation) is clearly the single largest contributor to global AP. This does not mean that other human activities do not pollute or produce air pollutants. Pollutant contributions from the industry, the agricultural activities and waste disposal are also non-negligible. In fact, industries around the world are responsible for the production and emission of all the criteria pollutants. It is important to single out one particular activity, which is the burning of forest for land-use changes. Carbon Monoxide (CO) emissions for this purpose are very high due to the nature of the burning material, which emits more than 50 times more CO than fuel or coal [14].

#### 2.1.4.3 The European Case

Europe has for long been on the forefront of the fight against AP emissions. The European Union has put in place a number of policies aiming at cutting (or even eliminating) emissions of human health compromising pollutant components. Few places in the world have been so demanding regarding their environmental practices, and numbers are a clear reflection of these adaptation efforts. In their 2019 report, the EEA state that European emissions have globally declined, and have been declining since at least the year 2000. Moreover, and in contrast with China's case, the GDP does not seem to be connected to AP emissions. As can be seen in Figure 2.9, emissions are decoupled from economic growth, as there are now less emissions per GDP unit than before [28].

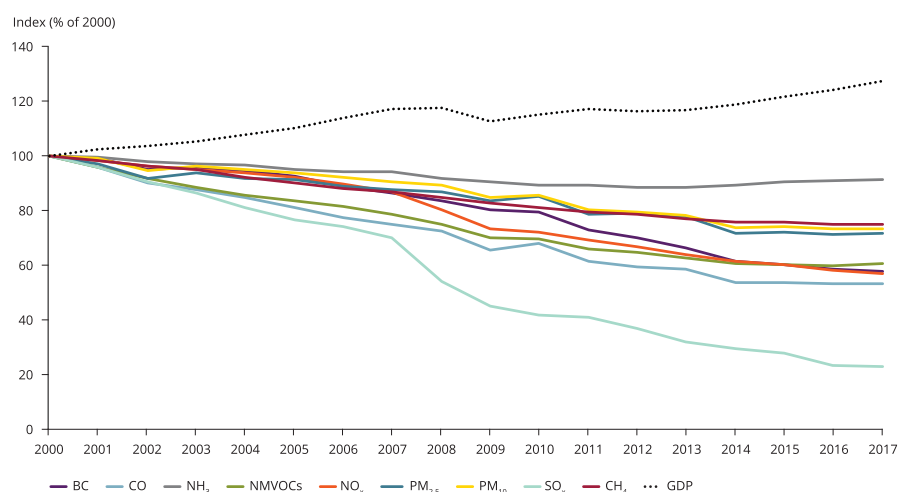


Figure 2.9: General trends for European emissions. Data presented in % emissions of year 2000. Note the downward global trend in pollutant emissions, and its decoupling with the European GDP [28].

## CHAPTER 2. LITERATURE REVIEW

---

If one extends this analysis further, and separates emissions by using their origin, the trends are approximately the same: except for Ammonia ( $\text{NH}_3$ ) (a side product of agricultural activities) a clear reduction is present in all sectors. These results can be seen in Figure 2.10 and were presented in [28].

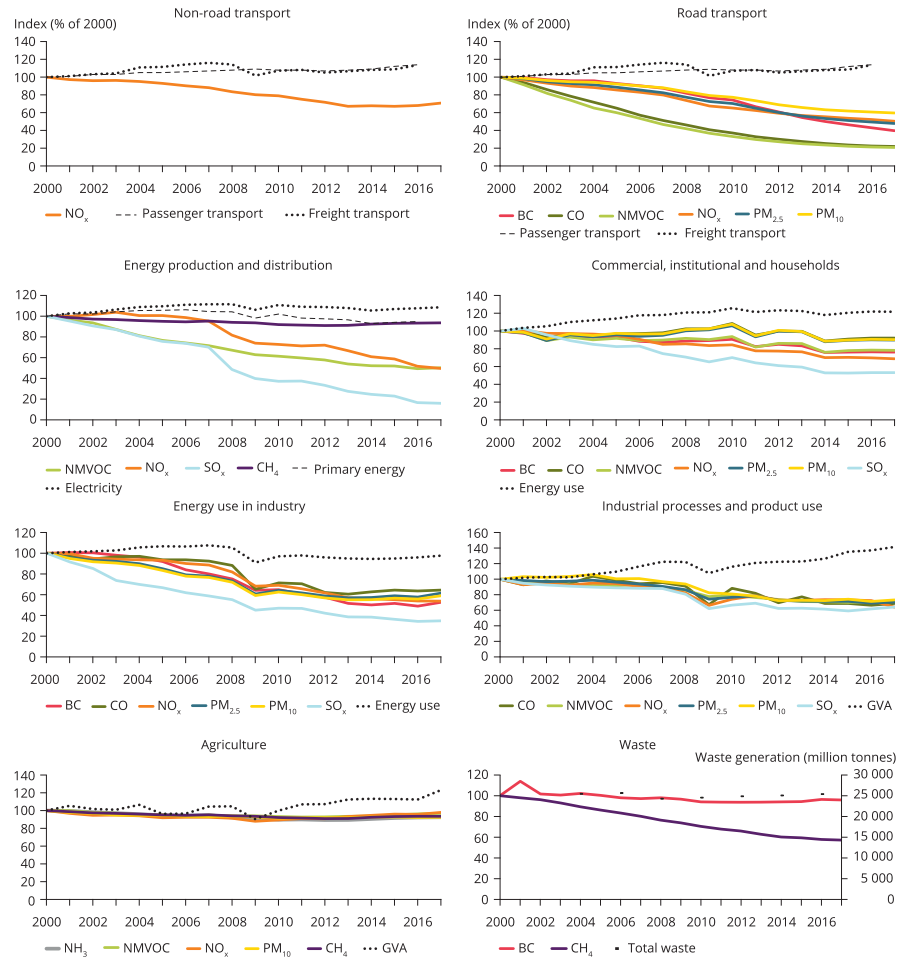


Figure 2.10: European emissions divided by activity sector. The global decreasing trend is confirmed, as industries all around are producing less and less AP with the passing years [28].

### 2.1.5 Detecting and Monitoring Air Pollution

There is no doubt that AP is a global threat that affects everyone, both in personal terms (through the degradation of their health) and in societal terms, through the investments and limitations that we as a whole have to commit to in order to prevent larger, unmanageable problems. Reducing AP is a priority and a requirement for today's modern societies. This demands immediate and effective actions, which in turn imply that we have a solid and profound understanding of how pollutants are created, transported and transformed in the atmosphere. The scale on which these interventions must be conducted requires them to be made on a concerted and collaborative manner, and always leveraged by technological development [28]. Many of the air pollutants cannot be detected solely by our senses, or even if they can is at already

dangerous concentrations. Technology is therefore a prerequisite to our fighting the problem of [Air Pollution](#) [84].

Pollution monitoring is itself based on the ability of a given measurement method to determine concentrations for trace gases, aerosols or radiation quantities. As with many other test techniques, in various fields, pollution monitoring techniques have three very important aspects to verify. The first of which is sensitivity, and also the most demanding. Important trace gases in atmospheric chemistry have sometimes vestigial concentrations, and the ability to correctly detect them is many times a technical challenge. The second most important is specificity, which is the ability of an atmospheric measurement to measure each compound independently, without a component influencing another component's measurement either positively or negatively. Finally, any usable monitoring technique must be sufficiently precise as to provide valid measurements.

[Air Pollution](#) monitoring techniques and devices are too many to address them all in this document. Besides, the physical principles involved are completely different from one to another, making it very difficult to make a broad generalization, other than the fact that they can be divided into local and remote sensing devices. The gold standard for air quality measurements remains those techniques in which a sample is collected in the field and then taken to the laboratory to be analyzed by very powerful analytical methods such as chromatography or mass spectroscopy. While undoubtedly providing the most accurate representation of the air composition at the time and place the sample was collected, it is also true that this method's results are too slow to use regularly in the field [84, 19, 6].

Another very important air quality monitoring method is the use of electrochemical sensors. The first variants (wet cells) of this kind of sensor became very popular in the field of industrial hygiene, where they were applied in many portable flue gas analyzers. They were very attractive to companies worldwide given their potential for very low costs in comparison to optical or other more complex techniques. Apart from the oxygen wet cell sensor, that has a slightly different configuration, these electrochemical devices are comprised of three electrodes - a sensing electrode, a counter electrode and a reference electrode - separated by a thin layer of electrolyte. The gas that is diffused to the surface of the electrode is either oxidized or reduced, thus changing the systems electrical properties, in a way that is then captured by an amplification circuit [19].

Wet cell electrochemical sensors were the precursors of the now more common solid state sensors. These sensors are the ones that we see in every subterranean parking lot, measuring several traffic related gases such as  $\text{CO}$ ,  $\text{CO}_2$  or  $\text{NO}_2$ . In general semiconductor gas detectors are comprised of two modules: a receptor and a transducer (see Figure 2.11). The receptor has in its composition a material (or set of materials) that, in contact with the target gas, induces a change in the systems inherent properties (work function, dielectric constant, resistance, etc.) or emits heat or light. The transducer is a device or circuit that converts the receptor's changes into an electrical signal [19, 6, 84].

Optical (spectroscopic) systems are fundamentally different from the other techniques that have already been presented. They can be used to perform remote sensing measurements (as far as being used for measurements aboard satellites). In the last few decades, these techniques have gained a lot of ground in atmospheric research,

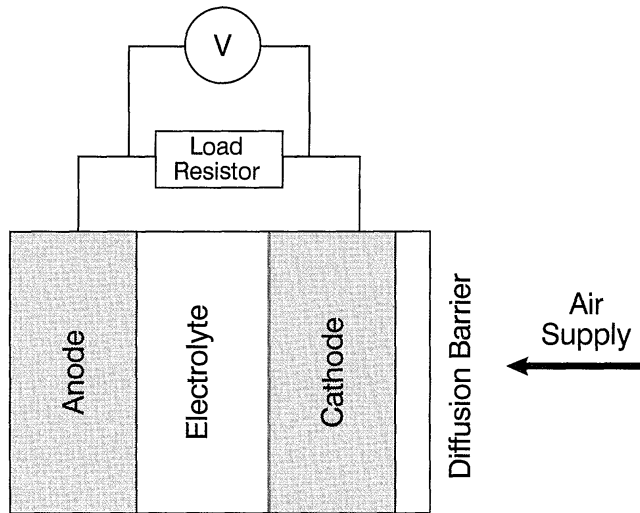


Figure 2.11: Semiconductor electrochemical sensor basic structure. There are many examples of this type of sensors, but in general they follow this architecture [19].

due to their high sensitivity and specificity and the universality of their applicability. Spectroscopic methods are based on Lambert-Beer's law (see Section 2.2 for a more thorough explanation), and make use of the fact that the way in which gases interact with light is well known and follows an exponential expression. There are many spectroscopic techniques for measuring AP. One of the most important atmospheric analysis methods, and especially in what concerns this document, is DOAS. While it is based on the same mathematical formulation as the other spectroscopic methods, it is also based on other factors, which shall be discussed in Section 2.2.

## 2.2 DOAS

**Differential Optical Absorption Spectroscopy** is a well established absorption spectroscopy technique that is widely used in the field of atmospheric studies [65]. In this section, I present a short introduction to the field. The first part of this introduction is based on [83], an article we have published in 2017, marking the conclusion of the initial studies for this PhD thesis. The second and last part refers to additional research that I have conducted since then.

DOAS itself is based on Lambert–Beer's law, which can be written as [65]

$$I(\lambda) = I_0(\lambda) \cdot \exp(-\sigma(\lambda) \cdot c \cdot L), \quad (2.1)$$

Where  $\lambda$  is the wavelength of the emitted light;  $I(\lambda)$  is the light intensity as measured by the system;  $I_0(\lambda)$  is the intensity of the light as emitted by the source; and  $\sigma(\lambda)$  is the absorption cross section of absorber, which is wavelength dependent;  $c$  is the concentration of the absorber we want to measure.

This law allows the definition of optical thickness ( $\tau$ ) [65]:

$$\tau(\lambda) = \ln \left( \frac{I_0(\lambda)}{I(\lambda)} \right) = \sigma(\lambda) \cdot c \cdot L. \quad (2.2)$$

In a laboratory setting, Eq. (2.1) or (2.2) can be used to directly calculate an absorber's concentration, provided there is knowledge of its cross section. In the open atmosphere, however, absorption spectroscopy techniques are far more complex. On one hand,  $I_0(\lambda)$  is not accessible since we measure from inside the medium we want to measure. On the other hand, there are several environmental and instrumental effects that influence measurement results. These effects include the following [65].

- Rayleigh scattering is due to small molecules present in the atmosphere and is heavily influenced by wavelength (hence the blue colour of the sky).
- Mie scattering is caused by particles and larger molecules suspended in the atmosphere and is not very dependent on the wavelength (hence the white colour of clouds).
- Instrumental and turbulence effects are the instrument's transmissivity and atmospheric turbulence in the optical path also limit light intensity.

In addition, we also have to take into account that, in the atmosphere, there are a number of trace gases that interfere with passing light. Another aspect worth mentioning is that our device is never pointed directly at the light source (the Sun) but always processes light that has been scattered at some unknown point in the optical path. This means that the light that reaches our detector is only the scattered fraction of the sunlight, depending on the system's position and geometry, as well as wavelength. The expansion of Lambert–Beer's equation to include all these effects results in Eq. (2.3).

$$\begin{aligned} \epsilon_{TG}(\lambda, s) &= \sum_i \sigma_i(\lambda, s) \cdot c_i(s) \\ I(\lambda) &= I_0(\lambda) \cdot A(\lambda, \dots) \cdot S(\lambda) \cdot \\ &\quad \cdot \exp \left[ - \int [\epsilon_{TG}(\lambda, s) + \epsilon_M(\lambda, s) + \epsilon_R(\lambda, s)] ds \right] \end{aligned} \quad (2.3)$$

Where  $A(\lambda, \dots)$  is the fraction of scattered light that reaches the device,  $S(\lambda)$  represents instrumental and turbulence effects,  $\sigma_i(\lambda, s)$  is the absorption cross section of absorber  $i$ ,  $c_i$  is the concentration of absorber  $i$ .  $\epsilon_{TG}(\lambda, s)$  is the absorption by the  $i$  trace gases,  $\epsilon_R(\lambda, s)$  represents Rayleigh's extinction coefficient and  $\epsilon_M(\lambda, s)$  represents Mie's extinction coefficient. The interest of this equation lies within the retrieval of  $c_i$ , a given absorber's concentration. Since the integral is taken along the total atmospheric path of the measured photons, and considering that their cross sections do not vary significantly in atmospheric conditions, it is possible to define the concept of slant column, which is of great importance [55].

$$SC_i = \int c_i(s) ds \quad (2.4)$$

This quantity, as Eq. (2.4) shows, equals the integral of an individual absorber's concentration along the atmospheric optical path of relevance. Now, without knowledge of  $I_0(\lambda)$ , these equations cannot give us absolute concentration values. We can, however, use another scattered light spectrum as reference in Eq. (2.2). Instead of absolute densities, this will yield relative changes in the atmosphere. We thus arrive at Eq. (2.5).

$$\begin{aligned} \ln\left(\frac{I_{\text{ref}}}{I}(\lambda)\right) &= \ln\left(\frac{A_{\text{ref}}}{A}(\lambda, \dots)\right) + \ln\left(\frac{S_{\text{ref}}}{S}(\lambda)\right) \\ &\quad + \sum_i (\sigma_i(\lambda) \cdot \Delta SC_i(\lambda)) + \Delta \tau_M(\lambda) \end{aligned}$$

Where  $\Delta SC_i$  is the relative slant column of absorber  $i$ ;  $\Delta \tau_M$  is the relative Mie scattering term, integrated to its optical thickness; and  $\Delta \tau_R$  is the relative Rayleigh scattering term, integrated to its optical thickness. This is where the principle of DOAS is applied. Instrument features, scattering and other atmospheric effects have broad absorption spectral profiles, which vary slowly with wavelength. Several trace absorbers have narrow and rapidly varying spectral signatures in at least a small section of the spectrum. By using Eq. (2.5), we can separate these contributions [21].

$$\sigma(\lambda) = \sigma'(\lambda) + \sigma_0(\lambda) \quad (2.5)$$

Here, the broad part of the optical thickness ( $\sigma_0(\lambda)$ ) can be separated from the narrow part ( $\sigma'(\lambda)$  – differential) by approximating it by a low-order polynomial, resulting in Eq. (2.6).

$$\ln\left(\frac{I_{\text{ref}}}{I}(\lambda)\right) = \sum_{i=1}^n \sigma'_i(\lambda) \cdot \Delta SC_i + \sum_{j=0}^m a_j \cdot \lambda^j \quad (2.6)$$

Where  $\sum_{i=1}^n \sigma'_i(\lambda) \cdot \Delta SC_i$  is the differential part (narrowband, rapidly varying with wavelength) and  $\sum_{j=0}^m a_j \cdot \lambda^j$  is a low-order polynomial, used to remove the broadband spectral features resulting from atmospheric and instrumental phenomena.

In practice, the mathematical solving of Eq. (2.6) is not enough since it does not account for the Ring effect or the non-linearities that result from stray light and wavelength shift in measured and cross-section spectra.

The Ring effect is a consequence of rotational Raman scattering: molecules in the atmosphere do not absorb photons in a purely elastic (Rayleigh scattering) fashion. A small portion of the light–matter interaction is in fact inelastic [8, 55]. This changes the light source frequencies as seen from the detector. This phenomenon was first noticed by Grainger and Ring in 1962. At the time, they noticed that the well-known Fraunhofer lines would slightly change when one observed them by using moonlight instead of scattered daylight [35]. Mathematically, the Ring effect is introduced into the DOAS expressions as a synthetically produced pseudo-absorber.

Up until this point, the DOAS problem can be solved by a system of linear equations of the form displayed in Equation 2.7.

$$\tau = A \cdot X \quad (2.7)$$

$A$  is an  $m \times n$  matrix. Its columns are the differential cross-sections for the measurement target gas,  $\sigma'_i(\lambda)$ , and the wavelength powers ( $\lambda, \lambda^2, \lambda^3, \dots$ ) according to the polynomial used for the broadband extraction described above,  $P(\lambda) = \sum_{j=0}^m a_j \lambda^j$ . The lines of matrix  $A$  are the wavelength window of study, as seen by the spectrometer used in the experiment. This leads to there being many more lines than columns in  $A$ . The system is thus overdetermined. Solving it requires the use of numerical approximations, and the most common approach is a least-squares approximation, in which the best solution minimises  $\chi^2 = [\tau - A \cdot X] [\tau - A \cdot X]^T$ . The upper script  $T$  used in this expression denotes the transpose of the preceding matrix [55, 65].

A crude DOAS algorithm might not go any forward. In effect, this is precisely the approach followed in [83] for smoke detection using machine learning techniques. A more refined measurement, aimed at quantification of the target trace gases and not at determining the presence of a particular type of atmospheric event requires an additional consideration, and some more algorithmic steps. There are in fact some nonlinearities in the complete retrieval process. These non-linearities are not retrievable through linear algorithms alone. These non-linear effects present themselves as shifts, stretches and offsets in the measured signal. They do not directly change the dependent variable values (i.e., the radiance), but instead "move" the scale of the independent variable (i.e., the wavelength). Therefore, linear approximations such as least-squares minimisation are not sensitive to them. A non-linear approximation algorithm such as Levenberg–Marquardt [66] can be used, and the expression that is being solved is presented in Equation 2.8.

$$\ln \left( \frac{I_{\text{ref}}(\lambda)}{I(\lambda + \text{shift}) + \text{offset}} \right) = \sum_{i=1}^n \sigma'_i(\lambda) \cdot \Delta S C_i + \sum_{j=0}^m a_j \cdot \lambda^j \quad (2.8)$$

Programming-wise, solving these equations is an iterative two-stage process, which runs until one of the following typical stop criteria are met.

**Maximum iteration number:** This is a self-explanatory criterion. It limits the number of times the algorithm's cycle can run;

**Minimum improvement threshold:** As the algorithm proceeds, this criterion ensures that it progresses in the correct direction, i.e., minimising  $\chi^2$ ;

**Minimisation target:** If  $\chi^2$  becomes lower than this given threshold, the cycle is terminated.

The cycle begins by the determination of the concentration values of the target trace gases and the  $\chi^2$  score is calculated. The wavelength window is shifted, stretched and offset according to the initial conditions. The  $\chi^2$  is re-calculated and compared to the previous value. This cycle is iteratively repeated in the best minimisation direction until any of the stop criteria are met and the cycle is terminated. The algorithm is illustrated (simplified) in Figure 2.12.

### 2.2.1 Types of DOAS experiments

There are two main families of DOAS assemblies, with different goals and capabilities:

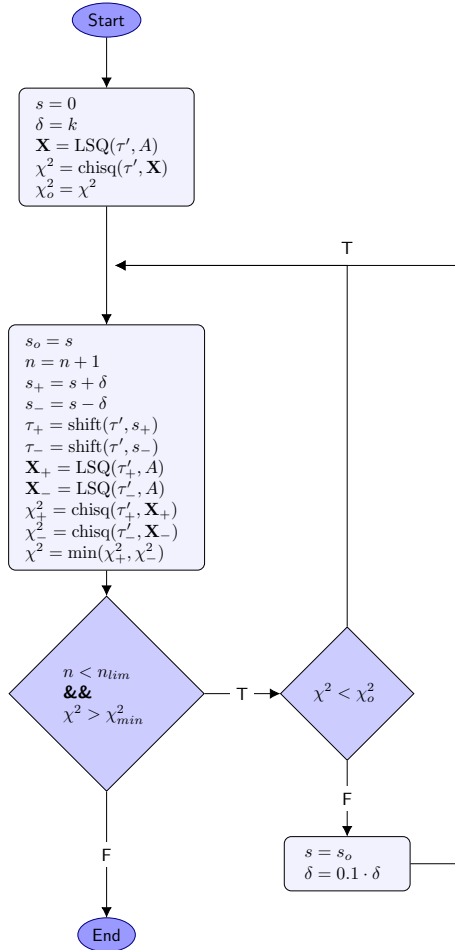


Figure 2.12: Simplified schematic flowchart of the DOAS algorithm, including the non-linear part.

- Active systems, of which a simple illustration is presented in Fig. 2.13, are characterized by relying on an artificial light source for their measurements. A spectrometer at the end of the light path performs spectroscopic detection. Active DOAS techniques are very similar to traditional in-lab absorption spectroscopy techniques [65];

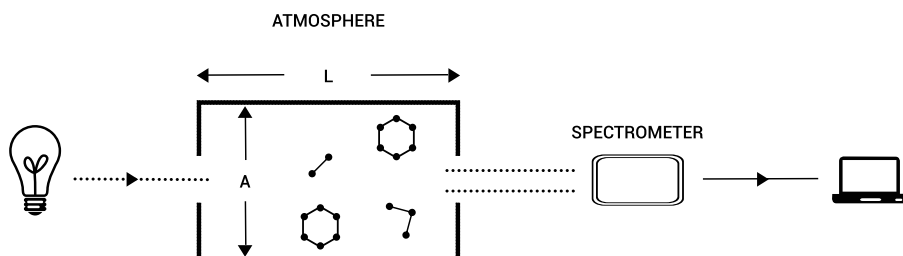


Figure 2.13: Active DOAS schematic.

- Passive DOAS techniques, illustrated in Fig. 2.14, use natural light sources, such as the Sun and the moon, in their measurement process. An optical system is pointed in certain elevation and azimuth angles and sends the captured light

into a spectrometer, connected to a computer. The system returns the total value of the light absorption in its path [65, 55].

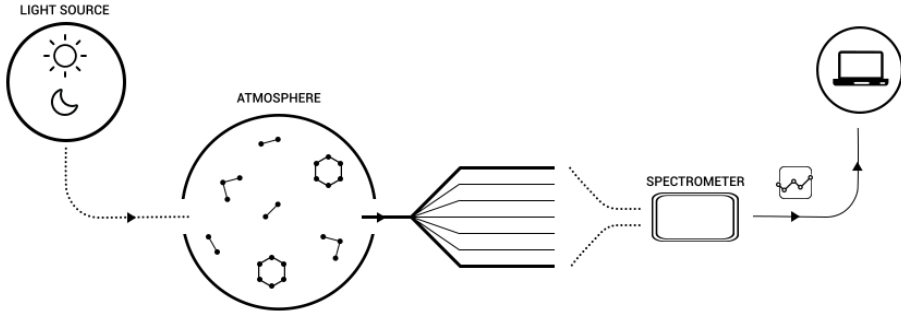


Figure 2.14: Passive DOAS schematic.

Within the two main **DOAS** families, there are several types of possible experiment. Differences in the design of these assemblies originate from a number of different target requirements. Active or passive applications can differ with relation to their intended spectral range, light throughput or resolution, among others.

In active experiments, the choice of the light source is the most critical aspect of the whole experimental design. Active **DOAS** light sources must be stable, have a very high throughput (these experiments are often conducted over long optical paths) and must have an adequate cost to purchase, maintain and operate. This is especially true in long-running experiments, which must remain working for months or even years. Moreover, the spectral range of the emitted light is also of central importance, because most trace gases have very particular spectral cross sections. The spectral structure of the emitted light is also an important feature to consider, for similar reasons.

The sun and the moon are the two most important light sources when it comes to passive **DOAS** applications. Sunlight can be used directly or after a scattering event, the latter being the more common. In these experiments, instead of pointing directly at the sun, the collector is pointed at a certain point in the atmosphere, entering the system after it has been scattered. There are many possible geometries to a scattered sunlight **DOAS** experiment. Some of them are schematically represented in Figure 2.15.

Although instrumentally simpler than their active counterpart, passive **DOAS** applications require more care in the retrieval process. In this kind of application, light sources are extremely far away. Additionally, they are normally highly structured. This means that one has to be extremely mindful when using it for the retrieval of small concentration changes. In addition to this, there is always the need to convert the system's direct measurement, a column density, into vertical densities. Since in scattered sunlight measurements, the optical path is impossible to calculate in a precise manner, this requires the use of complex radiative transfer models [65, 32].

### 2.2.1.1 Satellite Measurements

One particularly interesting use of passive **DOAS** are satellite measurements. There are three types satellite **DOAS** experiments:

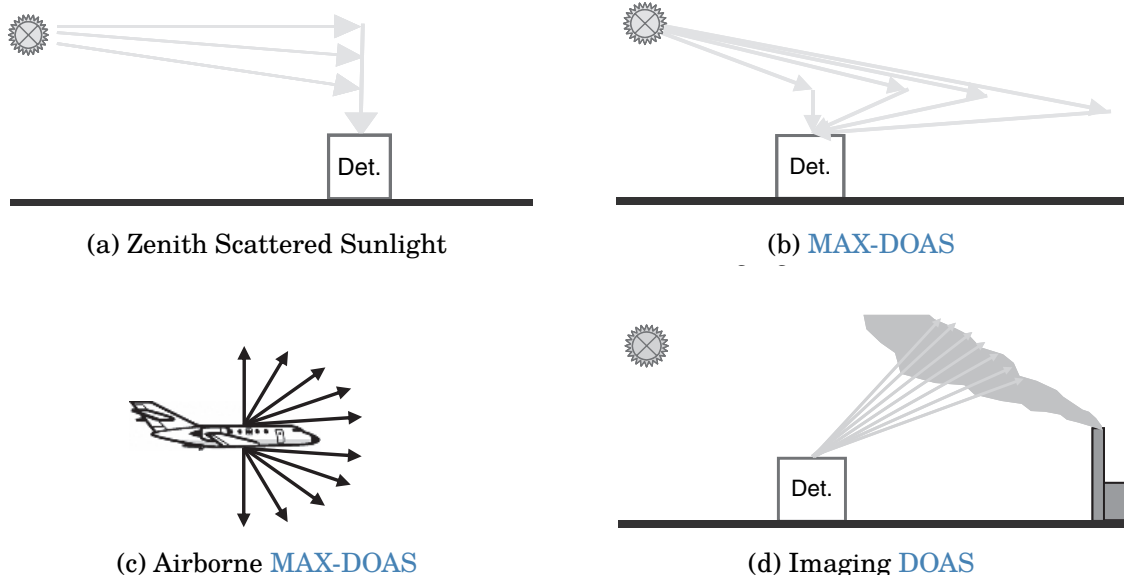


Figure 2.15: Several examples of possible passive DOAS experiment geometries. All these examples use only the light from an astronomical source to detect many atmospheric trace gases. All these examples were taken from [65].

**Occultation measurements:** this is a direct sunlight measurement. Light comes from the sun and traverses the Earth's atmosphere in a tangential manner before entering the satellite's light collector;



Figure 2.16: Occultation measurement schematic representation [65]

**Limb:** a scattered sunlight measurement, in which the collector is pointed towards the Earth, at an angle. Light reaches the detector after being scattered in the atmosphere, the ground, or both;

**Nadir:** this is the most common measurement geometry for satellite experiments. In this mode, light that gets reflected off the Earth's surface is captured by the collecting device, while it is pointing directly down.

Satellite based DOAS measurements have also been important because they have given rise to new trace gas retrieval techniques. Through them, new trace gases, previously unreachable through DOAS have been quantified on a global level, such as carbon monoxide through Weighting Function Modified Differential Optical Absorption Spectroscopy (WFM-DOAS) [12, 11].

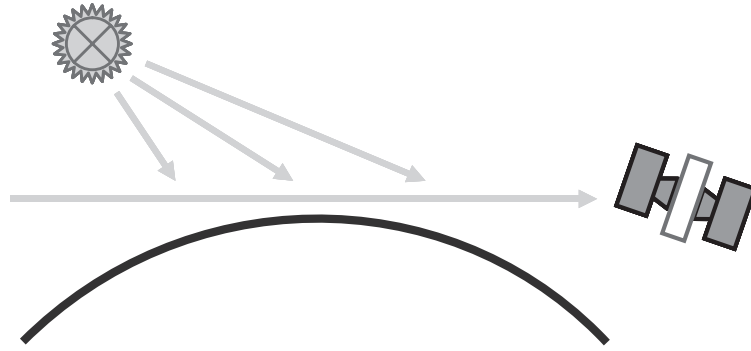


Figure 2.17: Schematic representation of the limb satellite measurement geometry.

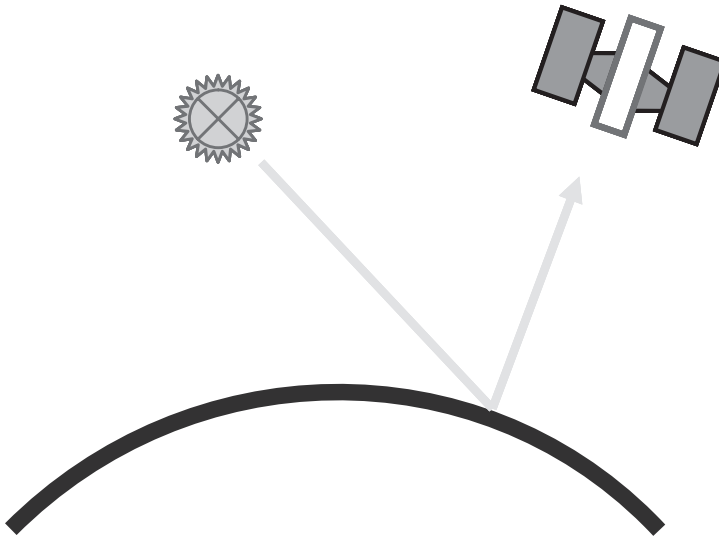


Figure 2.18: Schematic representation of the nadir satellite measurement geometry.

**WFM-DOAS** is a trace gas column retrieval algorithm, developed in the beginning of the 21<sup>st</sup> century, with the main goal of determining the total columns of gases such as CO, Water (H<sub>2</sub>O) or CO<sub>2</sub> from satellite nadir data [11]. Instead of using literature-obtained cross-section data for each target trace gas, the **WFM-DOAS** approach uses weighing functions, calculated through the application of a radiative transfer model, such as SCIATRAN [73]. Still, the retrieval is based on a fitting process. Equation 2.9, adapted from [12, 11] can be called the **WFM-DOAS** equation.

$$\left\| \ln I_i^{obs}(\mathbf{V}^t) - \left[ \ln I_i^{mod}(\bar{\mathbf{V}}) + \sum_{j=1}^J \frac{\partial \ln I_i^{mod}}{\partial V_j} \Bigg|_{\bar{V}_j} (\hat{V}_j - \bar{V}_j) + P_i(a_m) \right] \right\|^2 = \|RES\|^2 \rightarrow min \quad (2.9)$$

In Equation 2.9,  $I_i^{obs}$  is the observed sun-normalised radiance (the ratio between a nadir radiance measurement and solar irradiance) for the center wavelength  $\lambda_i$  of detector pixel number  $i$ .  $\mathbf{V}$  are the vector that have vertical columns as their components. These can be true,  $V^t$ , modelled,  $\bar{V}_j$ , or approximated,  $\hat{V}_j$ . The true columns

are unknown as we only have the radiance value and not the things on which it depends, modelled vertical columns are taken from the literature (they are climatological values) and  $\hat{V}_j$  are one of the fitting parameters. The other being  $a_m$ , the low order polynomial ( $P$ ) coefficients.  $RES$  is the fit residuum, which is minimised for the fitting.

## 2.3 Important Notes on DOAS in practice

Theoretically, the procedure described in Section 2.2 would be enough to obtain the target trace gas concentrations. In practice, this is an over-simplification. There are several additional required steps, most of them concerning a certain conditioning that one has to apply to both the collected and literature spectral signals.

### 2.3.1 Cross section conditioning

Unless conditions are absolutely stable, and one is able to record all data with the same device, which is impractical to the point of infeasibility, external literary sources are required for the DOAS analysis. These data are obtained with standardised trace gas sampling, extremely high resolution spectrometers and in carefully designed laboratory experimental setups.

To use external cross sections in one's own experiments, these data must be adapted to one's equipments. The very high resolution spectra coming from the literature are convolved with the instrument function of the real experiment's spectrometer. This function can be thought of as the device's impulse response. Since the spectrometer is inevitably imperfect, this response is not nearly as sharp as the impulse itself, and is normally modelled as a Gaussian curve fitted to a known source's well defined, impulse-like narrow structures. An Hg-Cd lamp was used in Merlaud's 2013 work, for instance [55]. For most spectrometers, this step is not actually required, as manufacturers already provide a very accurate spectral resolution value.

After calculating or fetching this value from the device's manual, it is a matter of creating a Gaussian kernel that can be used to filter the high resolution spectra through convolution. The **Full Width at Half Maximum (FWHM)** of the Gaussian kernel is equal to the spectrometer's resolution. One can ensure this by using the formula in Equation 2.10 which relates the width of the kernel with the standard deviation used to create it. The signal that results from the convolution of the literature cross sections and the gaussian kernel can be thought of as how the cross section would look if it had been acquired using the experiment's spectrometer.

$$FWHM = 2\sqrt{2\sigma^2 \ln 2} \rightarrow FWHM \approx 2.355 \cdot \sigma \quad (2.10)$$

The final step in this process of conditioning high resolution literature cross sections to the experiment that one is conducting is the discretisation of this signal. Physically, spectra are continuous signals. In practice, they were all captured using finite-resolution devices, and therefore are a digital signal. However, the resolution of the literature cross sections is so high in comparison to the usual resolution of a DOAS experiment spectrometer that one can think of this signal as being *quasi-continuous*. In order for them to be used in DOAS calculations, they have to be "re-discretised" onto the experiment's spectrometer sensor resolution. Since it is seldom the case (if ever)

that the literature and the low resolution pixels coincide, a mathematical routine is used to interpolate the former onto the latter. The most commonly used routine is the cubic spline interpolation, widely regarded as the best compromise between computational expense and accuracy [4]. Overall, cross sections used in DOAS undergo a process illustrated in Figure 2.19 [21, 4].

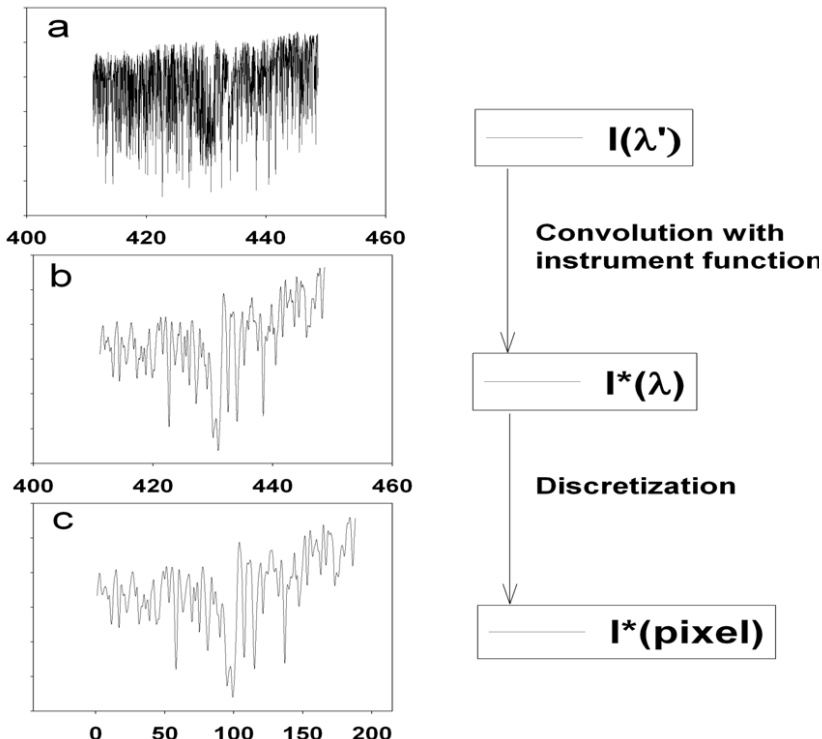


Figure 2.19: Before being used in DOAS calculations, literature trace gas cross section spectra must undergo a conditioning process to make sure they are compatible with the current experiment's instruments. Figure adapted from [4]

### 2.3.2 Spectral Calibration

One other small but important correction that can bias results is the lack of proper calibration between cross sections and collected spectra. Figure 2.20 shows how a conditioned cross section present slight wavelength related discrepancies.

These small nonconformities are caused not only because both types of data were captured by different spectrometers, but also because conditions most certainly changed. This means that situations in which calibration must be handled with care are the norm. This is done by running an iterative process that makes slight adjustments to the function mapping wavelength to pixel number, as explained in the next few paragraphs.

The light that enters the spectrometer is scattered by the diffraction grating before reaching the device's sensor, which is divided into pixels. These pixels have a well defined and finite width. At the centre of each one of them, the signal's intensity can

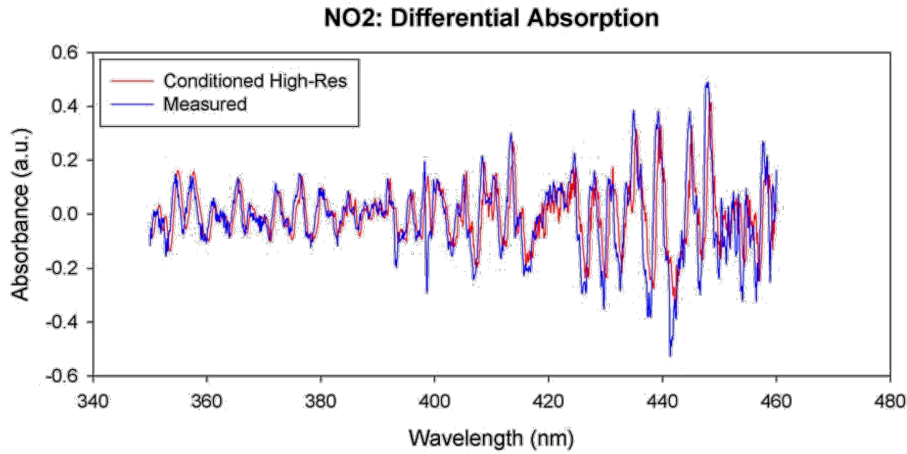


Figure 2.20: This figure, taken from [4], shows the difference between  $\text{NO}_2$  cross sections. The red line comes from the literature, and has been conditioned to the experiment spectrometer. The blue line was actually collected with that device. The slight discrepancies that can be observed are calibration defects.

be described by Equation 2.11, in which  $I$  is the intensity,  $i$  the pixel number and  $\lambda$  the wavelength.

$$I(i) = \int_{\lambda(i)}^{\lambda(i+1)} I(\lambda) d\lambda \quad (2.11)$$

The expression in Equation 2.11 assumes that the signal has been conditioned properly, as described in Section 2.3.1, through the convolution of the cross section data with the instrument function and adequate discretisation. The smaller  $\Delta\lambda = \lambda(i+1) - \lambda(i)$ , the finer the instrument's resolution. This is, of course, inherent to the system and cannot be changed. What can and should be changed during analysis is the central wavelength assigned to each pixel. This assignment is in fact what constitutes the instrument's calibration.

The most common way of conducting said calibration is by introducing a polynomial describing wavelength to pixel relationship. This polynomial is the wavelength-pixel mapping function, and can be written as in Equation 2.12.

$$\lambda(i) = \sum_{k=0}^q \gamma_k \cdot i^k \quad (2.12)$$

In Equation 2.12,  $\gamma_k$  determines how the pixels are mapped to the wavelength ( $\lambda$ ), and the type of mapping effect depends on  $k$ . Changing  $\gamma_0$  shifts the signal left or right; changing  $\gamma_1$  introduces linear distortions to the pixel mapping, i.e., stretching or squeezing of the signal. One can fit this polynomial up towards  $k = \infty$ , in theory, but normal spectrometer calibrations are only run up to the second or third degree. The Avantes spectrometers that were used in this dissertation are factory-calibrated to a fourth order polynomial.

The non-linear portion of the DOAS algorithm, described in Section 2.2, is indeed a wavelength calibration. However, it is important to previously calibrate every spectral signal before actually running the DOAS fitting process. This is because the types of

## 2.4. TOMOGRAPHIC ALGORITHMS AND RECONSTRUCTION TECHNIQUES

optimisation algorithm used in this technique, such as Levenberg–Marquardt, tend to find local minima or to not converge if there is significant misalignment between the spectra.

For passive applications using the sun as the light source, one can use a high resolution solar spectrum (see Figure 2.21), and the Fraunhofer bands in it (which have a very well defined wavelength that can be used as ground truth) to align the various spectra. For active applications, one can use the light source's own spectrum, either provided by the manufacturer or previously collected in the absence of atmospheric or other effects.

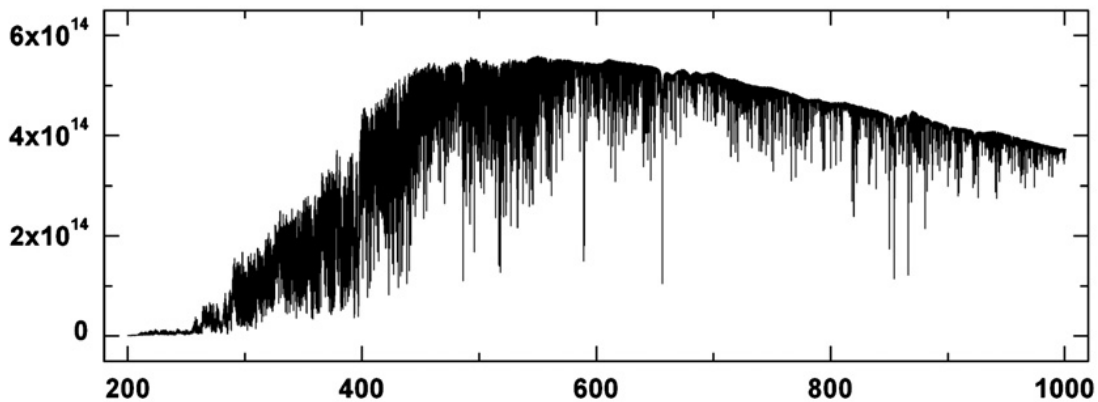


Figure 2.21: High resolution solar spectrum commonly used to calibrate the various spectral signals in DOAS experiments [18].

## 2.4 Tomographic algorithms and reconstruction techniques

Tomography is the cross-sectional imaging of an object through the use of transmitted or reflected waves, captured by the object exposure to the waves from a set of known angles. It has many different applications in science, industry, and most prominently, medicine. Since the invention of the Computed Tomography (CT) machine in 1972, by Hounsfield [37], tomographic imaging techniques have had a revolutionary impact, allowing doctors to see inside their patients, without having to subject them to more invasive procedures [46].

The central thought around tomographic image reconstruction is to recreate the information contained inside a target physical body, without having to cut it or open it in any way. The theory is based on Radon's idea that it is possible to "*represent a function written in  $\mathbb{R}$  in the space of straight lines ( $\mathbb{L}$ ) through its line integrals*" [71].

Say we have a body that we want to fully characterise without cutting open or destroying in any way. Now imagine we can traverse it with some kind of radiation, ray by ray, and that we are able to measure the rays after they traverse the target. What we would capture would be relative to the emitted radiation, of course, but it would also contain information on how that ray had interacted with the target body's matter. In the case of the ubiquitously used X-Ray radiation, the measurement would

be one of the total attenuation "imprinted" onto the ray by the target body's molecules, in the ray's particular direction. If said body is heterogeneous, the total attenuation can be derived by the infinitesimal sum of all different attenuation phenomena caused by the object's several different constituents (the same can be said of a homogeneous object, but in that case there is only one type of attenuation present). This means that each one of the rays contains information regarding the constitution of said body.

The question that arises is thus "*how we can use this information to create a spatially accurate representation of this target's interior composition?*". The answer to this question lies on many factors, but the most prominent of which are surely choosing the quantity that we are trying to find (that characterises the object) and assembling the projections (that is what we call the line integrals in tomographic imaging) in a way that allows solving an equation system for the aforementioned quantity. This assembly, a matrix of projections organised by their angles and position within the detector, is called sinogram. All tomography methods revolve around finding the relationship between it and the system's geometrical description [10, 46, 42, 40, 41, 24].

Let's consider the case in which we deal with a single ray of solar light entering the atmosphere at a given point. Since the atmosphere contains numerous absorbers and comparable atmospheric effects, the ray changes from the point where it enters the atmosphere to the point at which it is measured by a detector. Total absorption will depend on the pollutant species, their cross-section and their concentration, since it obeys Lambert-Beer's law. Looking from another angle, this absorption is also the line integral that we will use to reconstruct our image. With DOAS, it is possible to measure several pollutants at the same time, but for simplicity (and since it is one of the most studied compounds in the field), let's consider that the single pollutant in our atmospheric mixture is NO<sub>2</sub>.

The problem of tomographic reconstruction can be approached in a number of ways, depending mostly on the authors. In my literary search, I have found that Kak and Slaney [46] have certainly explained this problem in one of the clearer ways available. Therefore, I shall base the rest of my presentation in their writings, and complement with other authors' notes wherever necessary.

Considering the coordinate system displayed in Figure 2.22. In this schematic, the object is represented by the function  $f(x, y)$ . The  $(\theta, t)$  parameters can be used to define any line in this schematic. Line AB in particular can be written:

$$x \cdot \cos(\theta) + y \cdot \sin(\theta) = t \quad (2.13)$$

And if we were to write a line integral along this line, it would look like Equation 2.14, the Radon transform of function  $f(x, y)$ :

$$P_\theta(t) = \int_{-\infty}^{\infty} f(x, y) \cdot \delta(x \cdot \cos(\theta) + y \cdot \sin(\theta) - t) dx dy \quad (2.14)$$

Where  $\delta$ , the delta function, is defined in Equation 2.15.

$$\delta(\phi) = \begin{cases} 1, & \phi = 0 \\ 0, & \text{otherwise} \end{cases} \quad (2.15)$$

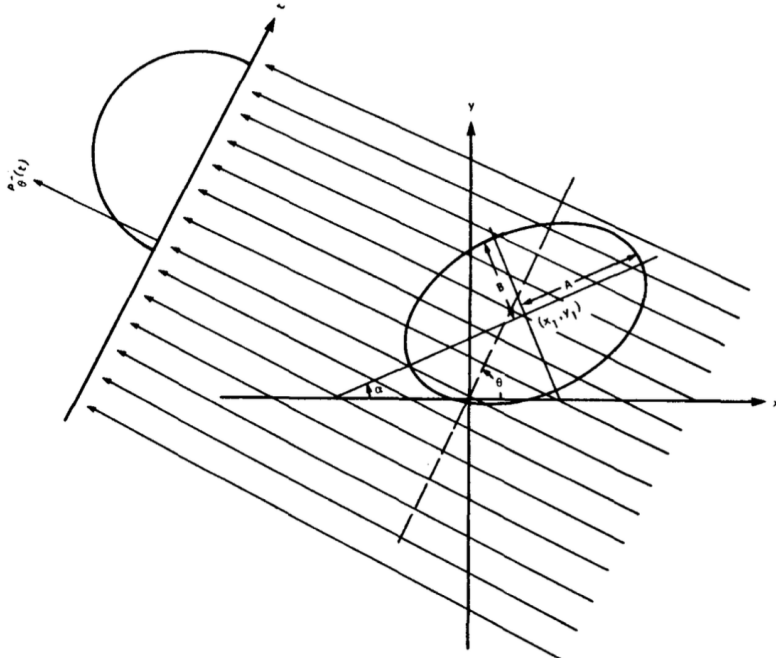


Figure 2.22: Schematic representation for coordinate setting. The image depicts a parallel projection setting [47].

As I have mentioned previously, a projection is a set of line integrals such as  $P_\theta(t)$ . Geometry plays a very important role in how the integrals are written and solved for reconstruction. The simplest case is the one where the set is acquired in a row, describing what is called a parallel geometry. Another more complex case is when a single point source is used as origin for all rays, forming a fan. This is called a fan-beam array. There are other possible geometries, but they fall out of the scope of this work and will therefore not be addressed any further.

The Fourier Slice Theorem (**FST**) is the most important component of the most important algorithm in tomographic inversion, the Filtered BackProjection algorithm (**FBP**). **FST** is based on the equality relation between the two-dimensional Fourier Transform (**Fourier Transform (FT)**) of the object function and the one-dimensional **FT** of the object's projection at an angle  $\theta$ . Let's start by writing the 2D **FT** for the object function, Equation 2.16, and the 1D **FT** of projection  $P_\theta$ , in Equation 2.17.

$$F(u, v) = \int_{-\infty}^{\infty} \int_{-\infty}^{\infty} f(x, y) \cdot \exp [-j2\pi(ux + vy)] dx dy \quad (2.16)$$

$$S_\theta(\omega) = \int_{-\infty}^{\infty} P_\theta \cdot \exp [-j2\pi\omega t] dt \quad (2.17)$$

For simplicity, let's consider the 2D **FT** at the line defined by  $v = 0$  in the frequency domain. We rewrite the 2D **FT** integral as:

$$F(u, 0) = \int_{-\infty}^{\infty} \int_{-\infty}^{\infty} f(x, y) \cdot \exp [-j2\pi\omega ux] dx dy \quad (2.18)$$

Notice that  $y$  is not present in the phase factor of the **FT** expression anymore, and this means we can rearrange the integral as:

$$F(u, 0) = \int_{-\infty}^{\infty} \left[ \int_{-\infty}^{\infty} \mathbf{f}(\mathbf{x}, \mathbf{y}) d\mathbf{y} \right] \cdot \exp [-j2\pi\omega ux] dx \quad (2.19)$$

Now, the **bold** part of Equation 2.19 is similar to Equation 2.14. It is precisely that equation, considering  $\theta = 0$  and a constant value of  $x$ , as in Equation 2.20.

$$P_{\theta=0}(x) = \int_{-\infty}^{\infty} f(x, y) dy \quad (2.20)$$

This in turn can be substituted in Equation 2.19, finally arriving at:

$$F(u, 0) = \int_{-\infty}^{\infty} P_{\theta=0}(x) \cdot \exp [-j2\pi ux] dx \quad (2.21)$$

And this is the one-dimensional **FT** for the projection at angle  $\theta = 0$ . Finally, the enunciation of the Fourier Slice Theorem:

**The Fourier Transform of a parallel projection of an image  $f(x, y)$  taken at angle  $\theta$  gives a slice of the two-dimensional Fourier Transform,  $F(u, v)$ , subtending an angle  $\theta$  with the  $u$ -axis (see Figure 2.23)**

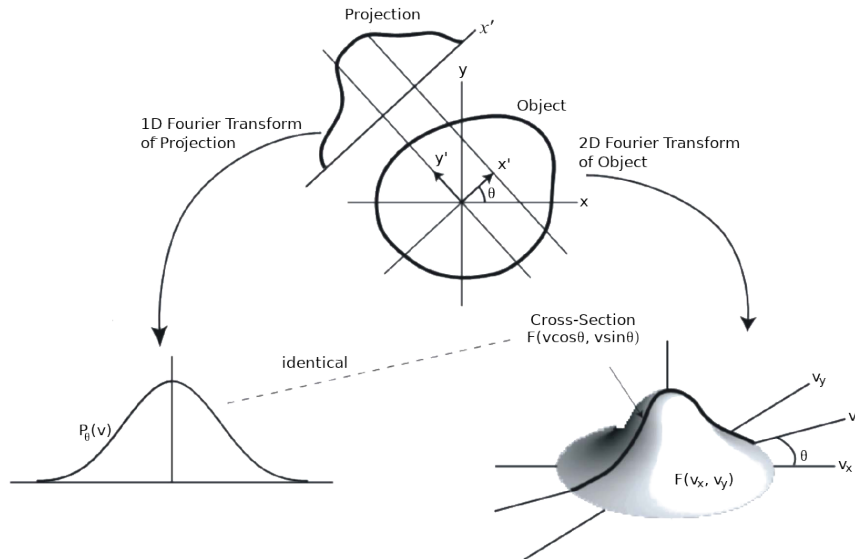


Figure 2.23: The **FST**, a schematic representation [3].

If one takes the **FST** into account, the idea behind the **FBP** seems to appear almost naturally. Say one has a single projection and its Fourier transform. From the **FST**, this projection is the same as the object's two-dimensional **FT** in a single line. A crude reconstruction of the original object would result if someone were to place this projection in its right place in the Fourier domain and then perform a two-dimensional **Inverse Fourier Transform (IFT)**, while assuming every other projection to be 0. The

## 2.4. TOMOGRAPHIC ALGORITHMS AND RECONSTRUCTION TECHNIQUES

---

result, in the image space, would be as if someone had smeared the object in the projections direction.

What is really needed for a correct reconstruction is to do this many times, with many projections. This brings a problem with the method: smearing the object in all directions will clearly produce a wrong *accumulation* in the center of the image, since every projection passes through the middle (remember we are still talking about parallel geometry projections) and are summed on top of each other, but on the outer edges, this does not occur. If one does not address this, the image intensity levels in the reconstructed image will be severely overestimated in the center and underestimated in the edges (due to normalization). The solution is conceptually easy: we multiply the Fourier transform by a weighting filter proportional to its frequency ( $\omega$ ) and that encompasses its relevance in the global scheme of projections. If there are  $K$  projections, then it is adequate for this value to be  $\frac{2\pi|\omega|}{K}$ . As an algorithm, **FBP** can be written as in Algorithm 1.

---

### **Algorithm 1:** The Filtered BackProjection Algorithm

---

**Result:** A reconstructed image of the projected object.  
**for**  $\theta \leftarrow 0$  **to**  $180$  **by**  $\frac{180}{K}$  **do**  
  measure projection  $P_{theta}(t)$ ;  
  FT( $P_{theta}(t)$ ), rendering  $S_{theta}(\omega)$ ;  
  Multiply by  $\frac{2\pi|\omega|}{K}$ ;  
  Sum the IFT of the result in the image space;  
**end**

---

Parallel projections, in which the object is scanned linearly from multiple directions, have the advantage of having a relatively simple reconstruction scheme. However, they usually result in acquisition times which are in the order of minutes. A faster way of collecting the data is one where all radiation emanates from a single point-source, which rotates around the target object (as well as the detectors). There are two types of fan-beam projections: equiangular and equally spaced. In this project, I have only worked with equiangular processes, so I will not include an explanation for equally spaced fan-beam projections. The reader may find this well described (much better than I would be able to) in [46] and [42].

Consider Figure 2.24. If our projection data were acquired through a parallel ray geometry, we would be able to say that ray SA belonged to a projection  $P_\theta(t)$ , in which  $\theta$  and  $t$  would be written:

$$\theta = \beta + \gamma \quad \text{and} \quad t = D \cdot \sin \gamma \quad (2.22)$$

In Equation 2.22,  $D$  is the distance between the source  $S$  and the origin  $O$ ;  $\gamma$  is the angle of a ray within a fan and  $\beta$  is the angle that the source  $S$  makes with a reference axis. Through these relationships one can *translate* the parallel projection's FBP algorithm to the fan-beam case, which involves several complex geometric transformations, although the overall rationale is exactly the same.

Another particularity of fan-beam projection data is the fact that they can be sorted into a parallel projection. For that, one starts with the premise that if one were to

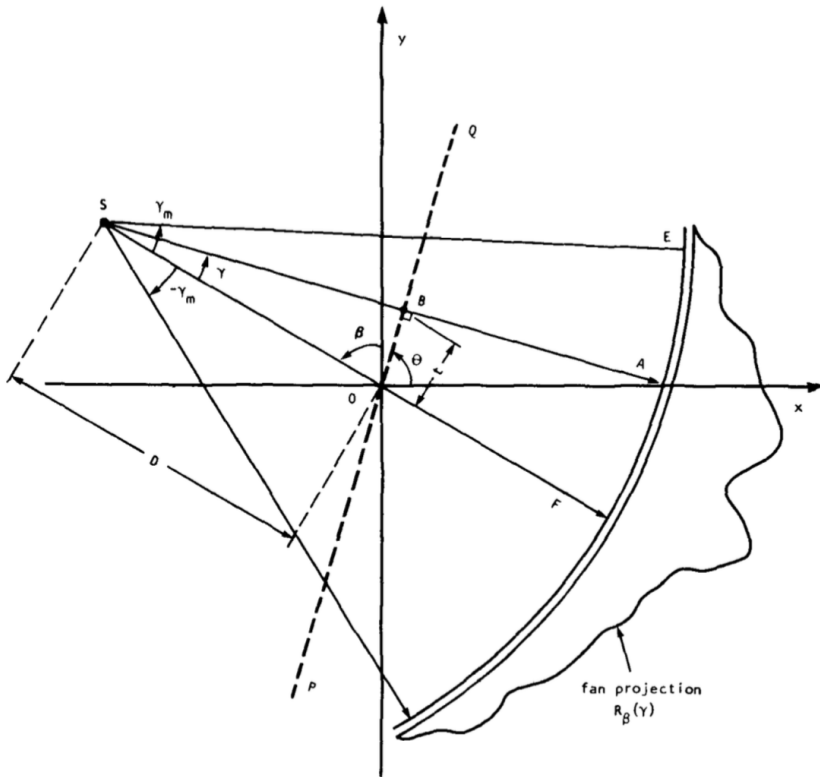


Figure 2.24: Schematic representation of an equiangular fan-beam projection, taken from [46].

substitute the fan geometry for parallel beams, most of the fan-beam rays would also appear in some projection of the parallel setup. This re-sorting algorithm starts with Equation 2.22. Now, if we call a fan-beam projection taken at angle  $\beta$   $R_\beta(\gamma)$ , and a parallel projection taken at angle  $\theta$   $P_\theta(t)$ , one could thus write Equation 2.23, which can already be used to re-sort any fan-beam projection into parallel beam geometry.

$$R_\beta(\gamma) = P_{\beta+\gamma}(D \cdot \sin \gamma) \quad (2.23)$$

Let's call the angular interval between fan-beam projections can be written  $\delta\beta$ , and the angular interval of rays within each fan is written  $\delta\gamma$ . In the case that they are the same ( $\beta = \gamma = \alpha$ ), then it is the case that they can both be replaced by multiples of that interval in Equation 2.23, which becomes Equation 2.24.

$$R_{m \cdot \alpha}(n \cdot \alpha) = P_{m \cdot \alpha + n \cdot \alpha}(D \cdot \sin n \cdot \alpha) \quad (2.24)$$

Or, in non-mathematical notation, the  $n^{\text{th}}$  ray of the  $m^{\text{th}}$  radial projection ( $R$ ) is the same as the  $n^{\text{th}}$  ray in the  $(m+n)^{\text{th}}$  parallel projection. Although being much simpler than directly applying the FBP algorithm to the fan-beam projection data, this method has a limitation, which is the non-uniformity of the generated parallel projections. This can usually be corrected through interpolation [47].

## 2.5 DOAS Tomography

In previous sections (Section 2.2) we have established that DOAS is a widespread spectroscopic technique with particular usage in the atmospheric research community. This technique uses either artificial or natural light to retrieve slant column densities, the number of molecules that interact with the said light in a given optical path. These values are described by Equation 2.4, and are indeed line integrals.

Also in a previous but different section (Section 2.4), we have seen that with enough of these integrals (which we can call projections), we can gather enough information to depict the interior structure of an object that we make traverse with radiation of some kind, as long as it is measurable and its behaviour is well known.

Joining the two notions, we can get to the idea that it would be possible to use DOAS in a tomographic manner, so long as we use sufficient light collection points. This has been proposed by Byer and Shepp [13] in 1979. At the time the authors did not mention specifically the DOAS technique, but the assembly they propose is essentially equivalent to one that would use this method. DOAS tomography was also mentioned in one of the main pieces of literature in the field, [65], as one of the most promising avenues available for DOAS progress in the future.

As a requirement for one of the courses that I chose to pursue during the curricular part of my doctorate, I had to complete an assignment that consisted in writing a Systematic Mapping Study on the subject of DOAS tomography. The study is included in full in Appendix ???. It aims at characterising the literary panorama regarding the subject and tries to arrive at a standard application with respect to software, algorithms and instrumentation.

This type of study has a particular methodology focused on repeatability. Its complete explanation is out of scope of this section and even this document, but a simplified schematic is included in Figure 2.25. A more detailed and extensive description of this method can be found in several works available in the literature, namely [49, 50, 76].

After defining search terms and conducting the actual search, we arrived at a total of 9 relevant papers. These were analysed under the light of the study's main goal, which was to identify a standard DOAS tomography device and application.

The first identifiable pattern is the marked prevalence of active DOAS systems. 11 out of the 13 retrieved papers describe or consider an active DOAS system of some kind. As stated in Section 2.2, active DOAS systems do have better analytical capabilities than their passive counterparts, although that comes at the cost of increased instrument complexity and operational costs.

Another immediate conclusion is that there is a "dominant" study. Almost half of the papers found originated from the BABII campaign, in which a group of researchers set out to quantify pollution through DOAS tomography along a busy German motorway, in the beginning of the 21<sup>st</sup> century [39, 38, 51, 68, 70, 69, 56].

All of the active DOAS systems were purposely built for their corresponding experiment (or group of experiments). BABII researchers used two telescopes with around 200mm diameter and 1m focal length to simultaneously illuminate 8 retroreflectors that were assembled onto two towers located on each side of the road. In one of the papers associated with this initiative, the same telescope instrumentation was used

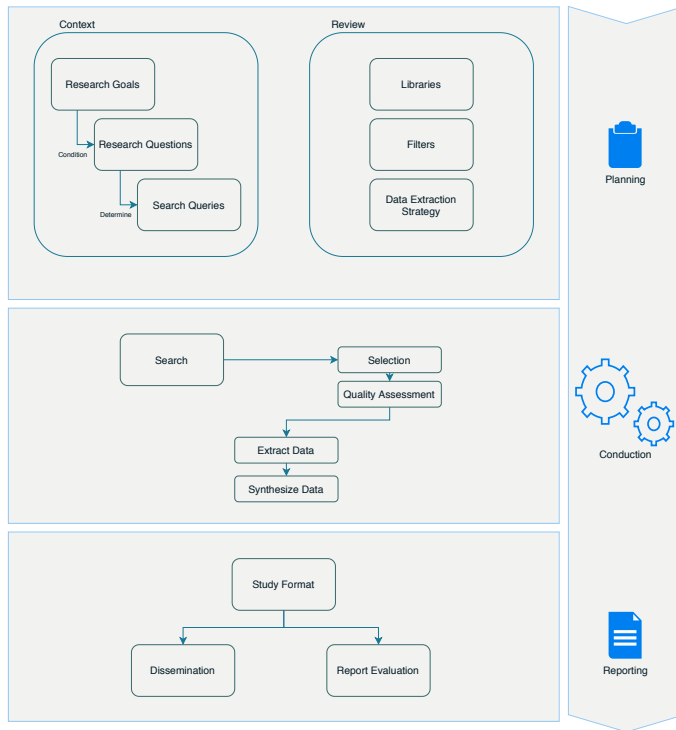


Figure 2.25: Simplified diagram of the [SMS](#) method. This type of study is focused on registering every step of the search and the reading of the retrieved material, in an effort to make the process completely repeatable. Adapted from [49].

to validate the 2D reconstruction technique that was going to be used in the other papers. The campaign's main assembly is illustrated in Figure 2.26.

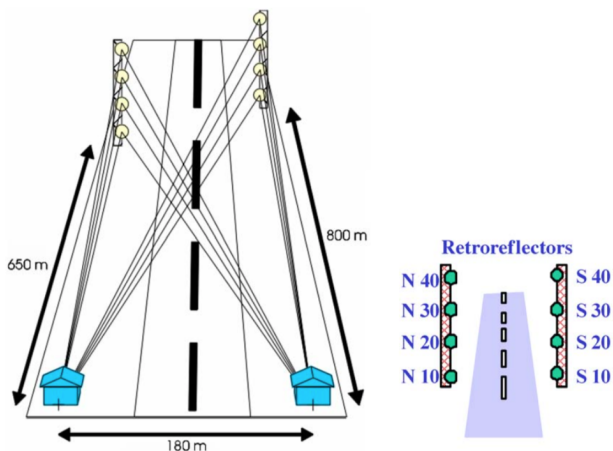


Figure 2.26: BABII assembly geometry. In this experiment campaign, the telescopes illuminated retroreflecting targets that were positioned in two steel towers on both sides of a busy motorway in Germany, connecting Heidelberg to Mannheim [69].

Another important initiative with respect to [DOAS](#) tomography was the study conducted in 2016 by Stutz et al [79]. The approach in this case was to use a similar telescope to detect the light emitted by a narrow interval UV LED light source (290nm) to create a fence line monitoring system for Benzenes, Toluene and Xylene. The team

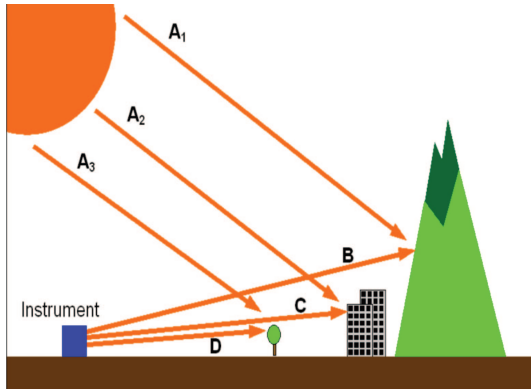
managed to apply this system in a successful manner in refineries in Los Angeles and Houston. One of the most interesting aspects of this study is that it details a tomographic system that could easily be commercially deployed.

Another type of DOAS tomography system was proposed by researchers in the Cork Institute of Technology [59, 60, 57]. In their three papers, the authors describe 1) a new multipath instrument that significantly increases the amount of projection information in this kind of application; 2) a tomographic reconstruction algorithm based on evolutionary algorithms; and 3) the application of DOAS tomography to a simulated urban canyon scenario. Although all three papers present technological innovation, it would not be fair not to say that from a strictly literary point of view, these were among the weakest retrieved by the search process.

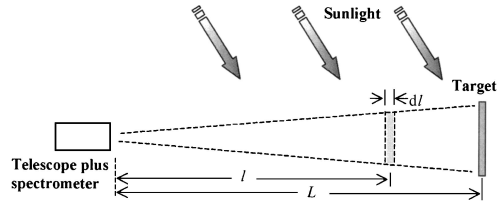
Regarding passive DOAS applications, the two papers we have found come with two completely different paradigms. The first article [45] was written in 2009 and details the application of a tomographic inversion algorithm to a scanning DOAS application, designed to work with trace gas plumes like the ones above volcanoes or power stations. The team present a system composed of two DOAS devices, with sufficient distance with themselves as to allow tomographic reconstruction, but sufficiently small to allow the light path to be considered a straight line from the point of last scattering to the detector. The authors applied an adapted version of the Lower Third Derivative (LTD) algorithm to the projections obtained by pointing the set of fixed DOAS apparatus towards the plume in different angles. Besides simulations for their proposed method, the authors have also conducted practical experiments, both over a power plant in Spain and a volcano in Italy. Results from these experiments display a good agreement between reality and simulation results, proving the technique's validity.

The second Passive DOAS application is a paper published by Frins et al. [32]. In this study, the researchers detail a particular application in which they measure light coming from bright and nonreflecting sun-illuminated objects in their field of view. They use this light to retrieve column density values for a number of trace gases. The proposed method also includes a way with which to remove the stratospheric contribution that appears in the measured light besides the target column. The authors discuss how radiative transfer can influence measurements, but they also present a number of approaches to mitigate this problem, ensuring the validity of their approach. Besides presenting the method, the authors also describe an experiment they conducted by assembling and manoeuvring a DOAS system on top of a building in Heidelberg, Germany.

In summary, the search has found that active tomographic DOAS is far more common than the passive counterpart (11 out of 13 articles discussed this method). This preference can be explained by the fact that the results produced by this kind of system are generally superior to those obtained by passive methods. However, passive applications are normally much less demanding on a technical level, and are simpler to run and assemble. Much as a result of this, we have also identified that the systems used in the literature were not mobile or had a very low mobility level which in turn caused that all the systems were working with low projection numbers. This should be taken into account in future research on the topic. As a final note, we would also like to point out that there is no commercially available systems for this kind of application, although some of the articles, like the one by Stutz in 2016 [79] detail systems which



(a) Schematic representation of Frins's assembly [32].



(b) The physical principle behind Frins's paper [32].

Figure 2.27: Erna Frins's paper [32] proposes a very relevant passive DOAS application that can conceptually be employed in a DOAS tomography scenario. In this 2006 paper, the authors use multi-axis measurements of sun-illuminated targets to estimate absorption paths without using radiative transfer models.

could easily be adapted to that end.

## METHODS

Macroscopically, the approach to the **RQ** was conducted by working with two hypothesis:

**First Hypothesis:** The definition of a particular set of algorithmically defined projections in such a manner that they might be used for tomographic reconstruction of column densities of trace gases in the atmosphere, in a given **ROI**;

**Second Hypothesis:** We can retrieve the column density for a given trace gas (or set of trace gases) between two points by performing a spectral measurement in both of these points in the same direction and subtracting them one from the other.

To test the first hypothesis, I have used a number of computational methods to define and create projection and backprojection matrix operators, resulting in a dedicated simulation software tool that proves without a doubt that the devised projection gathering strategy is able to produce projection information in sufficient quantity as to perform tomographic reconstruction. This procedure is detailed in Section [3.1](#).

The second hypothesis was experimentally tested, by the conduction of a number of field experiments designed to determine the validity of measurement hypothesis with the equipments to which I have current access. The experiment and the protocol that was followed is detailed in Section [3.2](#). This chapter is heavily based on one of the two articles generated by the work of this thesis.

### 3.1 Tomosim

Tomosim was the (somewhat unoriginal) name given to the tomographic simulation software tool that was designed and built as part of this project. It was created to tackle the trajectory-related hypothesis, briefly described in this chapter's introduction.

The final system must be able to gather projection information by reading spectral information, in this case the **DOAS**-retrieved column density for an atmospheric trace gas (or several) from a set of predetermined directions. In "normal"tomographic **DOAS** application, these directions are fixed and depend on the experiment infrastructure's geometry (see Section [2.5](#)). One of the main novelties that I am trying to create with this project is a very high degree of geometric freedom. A mobile system has no

custom infrastructure, and therefore has no fixed positions to which it is tied. Instead its ability measure and monitor its atmospheric surroundings relies on its movement.

A ground-based mobile DOAS-tomography system would have too strong a dependency on open spaces and the topography of its ROI to be useful in any *real world* scenario. A much more interesting and feasible approach would be to use some kind of flying machine that could carry spectroscopic equipment, and that could be programmed to fly in a precise manner. Fortunately, current day technology provides a very strong immediate candidate: a UAV of the n-copter type, such as the one in Figure 3.1.



Figure 3.1: Hexacopter in flight. Image taken from LevelFiveSupplies[52], for illustration purposes only.

A natural choice as it may seem as means for the measurements I am describing in this document, its programming is almost as important as the hardware itself (if not more). The vehicle must be programmed to describe a very precise (taking into account the type of operation we are proposing) trajectory. In flight, the drone should be able to carry and point an optical system towards any direction and in a short time. Said optical system should be attached to a computer-controlled spectrometer. This would allow the whole system to determine target trace gas concentration on demand and programmatically.

The programmed trajectory should make use of these capabilities and gather enough information for tomographic reconstruction. This also means that the trajectory must be comprised of a sufficient number of spectral projection acquisition opportunities.

Of the several geometries that are described in the literature for tomographic reconstructions, the one that seemed to be more promising in terms of the balance between reconstruction complexity and the information / flight time ratio was the fanbeam assembly (described in Section 2.4). It was the feasibility of this trajectory for the proposed purposes that this simulation aimed to prove.

In essence, the drone's trajectory (illustrated in Figure 3.2) is a horizontal circle which is parametrised to be at a certain height and to have a certain diameter. Both of these dimensions are set at experiment / measurement time. The drone stops on this circle at regular angular intervals, say  $\alpha$  degrees. Each one of these stops ( $360 / \alpha$  stops) will generate a fanbeam projection, by pointing the optical system inwards (with respect to the circular macro-trajectory) and performing a series of spectroscopic measurements in different directions and also at regular intervals, say  $\gamma$  degrees. The

particular case in which  $\alpha = \gamma$  is very interesting, because it then opens the possibility for resorting the fanbeams into parallel virtual-projections that are much easier to reconstruct tomographically, as introduced in Section 2.4.

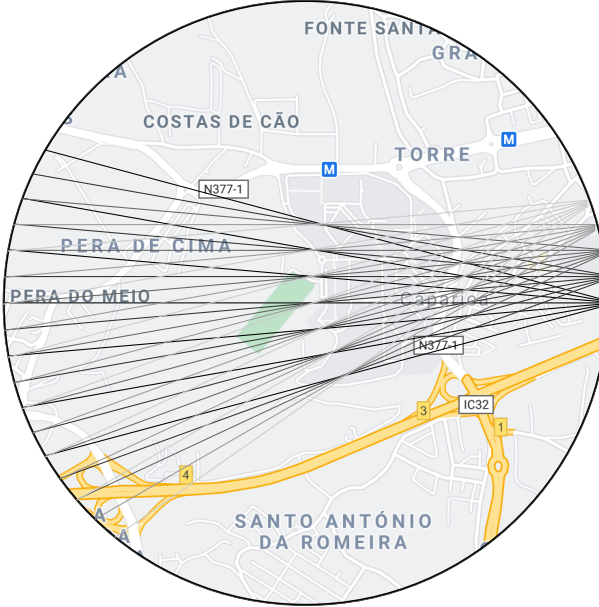


Figure 3.2: Illustration of the projection gathering algorithm based on the assembly of groups of acquisitions as fanbeam projections. The lines presented on the drawing come from the right to the left. Each is a ray in fan, corresponding to one stop of the drone. In the second measurement moment, the drone moves to the exit point on the left and repeats the first moment collection. Here, both fans and rays are separated by 5 degrees and there are 6 rays within each fan. A "real life" acquisition would feature a lot more rays, but that would be graphically complicated for the reader. Both ray and fan angular distance are customisable at runtime. Map taken from Google Maps in 2019. ©Google.

### 3.1.1 Discretisation

Discretisation is the process by which the **ROI** is digitised into a computational platform. There are several algorithms designed for this effect that are available in the literature. One of the easiest to implement that is also adequate to this application (unsurprisingly) comes from the medical imaging field. It was published in 1985 by Robert Siddon [75].

The Siddon algorithm is one of the foremost path calculation algorithms in the medical field of radiology. It is not only used for the discretisation of tomographic fields, but also in the dose calculation process of radiation therapy patients. The idea behind the algorithm is that the total dose of a radiation ray, i.e., its path, is given by the sum of the length within each pixel that this ray traverses multiplied by the density of said pixel. In mathematical notation, one can write this as in Equation 3.1.

$$d = \sum_i \sum_j \sum_k kl(i, j, k) \cdot \rho(i, j, k) \quad (3.1)$$

In Equation 3.1,  $d$  is the radiological path (the projection value),  $i, j, k$  are the coordinate vectors,  $l$  is the length within a pixel and  $\rho$  is the pixel density. In our case, this last value is the trace gas column density for that pixel.

The main reason for Siddon's algorithm being easy to implement is its treatment of pixels (or voxels if in 3D). Instead of considering pixels as *atomic*<sup>1</sup> units, it defines them as the intersections of orthogonal sets of equally spaced lines (planes in 3D). Pixel lengths are determined by the looking at the intersections between the orthogonal lines and the radiation ray.

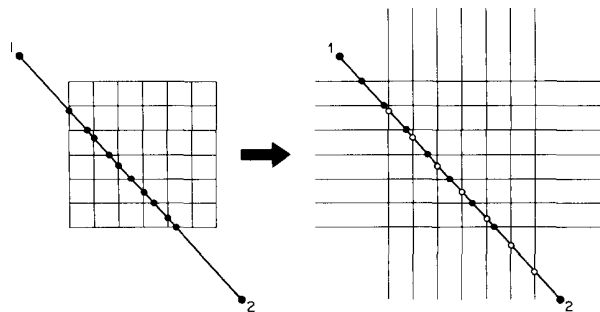


Figure 3.3: Grid and pixel definition, as they appear in the original article by Robert Siddon [75]. Pixels are "formed" by intersecting the ray (here going from point 1 to point 2) with the superimposed grid.

Since lines are orthogonal and equally spaced, all intersections can be calculated recursively after knowing where the first intersection is located. The calculation of the radiologic path is achieved by determining the subset of the intersections between the orthogonal lines and the light ray that identifies individual pixels.

If  $P_1 \rightarrow (X_1, Y_1)$  and  $P_2 \rightarrow (X_2, Y_2)$  are the start and end of the radiologic path within the ROI, the line between them can be parametrically written as in Equation 3.2.

$$\begin{aligned} X(\alpha) &= X_1 + \alpha \cdot (X_2 - X_1) \\ Y(\alpha) &= Y_1 + \alpha \cdot (Y_2 - Y_1) \end{aligned} \tag{3.2}$$

In Equation 3.2,  $\alpha$  is 0 at  $P_1$  and 1 at point  $P_2$ . Values of  $\alpha$  within the ROI vary according to the positions of  $P_1$  and  $P_2$  with respect to the ROI. By determining  $\alpha$  values of each intersection (in both directions), one can determine the length of the ray within the pixel by the difference of adjacent intersections. The whole algorithm

---

<sup>1</sup>In their undivisible sense.

can be written as in Algorithm 2.

---

**Algorithm 2:** Siddon's algorithm's procedural steps. After running this algorithm, one is able to represent any continuous ray through the analysis field as a sum of discrete lengths

---

**Result:** Discretised ROI space.

- calculate range of parametric values;
  - calculate range of pixel indices;
  - calculate parametric sets;
  - merge sets;
  - calculate pixel(or voxel) lengths;
  - calculate pixel indices;
- 

Detailing the two-dimensional case<sup>2</sup> should start by the definition of the discretisation grid itself, as in Equation 3.3. The equation reflects the recursive nature of the grid definition. In it,  $d_x$  and  $d_y$  are the distances between the  $x$  and  $y$  planes, which correspond to the lengths of the pixels in those coordinates.  $N_x$  and  $N_y$  are the number of pixels in  $x$  and  $y$  that are contained in the grid.

$$\begin{aligned} X_{\text{plane}}(1) &= X_{\text{plane}}(1) + (i - 1) \cdot d_x \\ Y_{\text{plane}}(1) &= Y_{\text{plane}}(1) + (j - 1) \cdot d_y \end{aligned} \quad (3.3)$$

The parametric values  $\alpha_{\min}$  and  $\alpha_{\max}$  are given by the intersections of the ray with the sides of the grid ( $i = 1$  and  $i = N_x$ ) and can be written as in Equation 3.4.

$$\begin{aligned} \alpha_{\min} &= \max \{0, \min [\alpha_x(1), \alpha_x(N_x)], \min [\alpha_y(1), \alpha_y(N_y)]\} \\ \alpha_{\max} &= \min \{1, \max [\alpha_x(1), \alpha_x(N_x)], \max [\alpha_y(1), \alpha_y(N_y)]\} \end{aligned} \quad (3.4)$$

Not all line intersections have a corresponding parametric value. The ones that do are comprised within index ranges that are defined by Equation 3.5. This equation presents the case for the first coordinate ( $x$ ), with the second coordinate having an identical expression.

$$\begin{aligned} i_{\min} &= N_x - \frac{X_{\text{plane}}(N_x) - \alpha_{\min}(X_2 - X_1) - X_1}{d_x} \\ i_{\max} &= 1 + \frac{X_1 + \alpha_{\max}(X_2 - X_1) - X_{\text{plane}}(1)}{d_x} \end{aligned} \quad (3.5)$$

Equation 3.5 defines a range of possible indices for the pixels, in parametric fashion. We can use this range to construct the set of used parametric indices, given in Equation 3.6 for the  $x$  coordinate.

$$\{\alpha_x\} = \{\alpha_x(i_{\min}), \dots, \alpha_x(i_{\max})\} \quad (3.6)$$

Although Equation 3.6 only presents the expression for the first coordinate, there are similar expressions for the other coordinates at play. After determining the set of possible indices for  $x$  and  $y$ , these sets must be arranged in ascending order, creating

---

<sup>2</sup>A three-dimensional case would be just the same but with an additional coordinate.

an index superset. To this the minimum and maximum values, calculated in Equation 3.4, are appended. The resulting and final set of parametric values is presented in Equation 3.7.

$$\begin{aligned}\alpha^* &= \text{merge}(\alpha_x, \alpha_y) \\ \{\alpha\} &= \{\alpha_{min}, \alpha^*, \alpha_{max}\} \\ &= \alpha(0), \dots, \alpha(n)\end{aligned}\tag{3.7}$$

Where the last term,  $n$ , is given by the sum of all index range numbers, as in Equation 3.8, again for the two-dimensional case.

$$n = (i_{max} - i_{min} + 1) + (j_{max} - j_{min} + 1)\tag{3.8}$$

Each element of the array defined in Equation 3.7 is an intersection between the ray and a given pixel. Since they are ordered, it is possible to calculate the array of pixel lengths for each ray, using the expression in Equation 3.9.

$$l_m = d_{12}[\alpha(m) - \alpha(m - 1)] \quad (m = 1 \dots n)\tag{3.9}$$

With  $d_{12}$  being the distance between  $P_1$  and  $P_2$ , calculated through the Euclidean formula for distance between two points. In Tomosim, this distance is always equal to the trajectory's diameter.

Pixel  $[i(m), j(m)]$  is located in the midpoint between the  $m^{\text{th}}$  and the  $(m-1)^{\text{th}}$  intersections. It is given by the expression in Equation 3.10.

$$\begin{aligned}\alpha_{mid} &= \frac{\alpha(m) + \alpha(m - 1)}{2} \\ i(m) &= 1 + \frac{X_1 + \alpha_{mid} \cdot (X_2 - X_1) - X_{plane}(1)}{d_x} \\ j(m) &= 1 + \frac{Y_1 + \alpha_{mid} \cdot (Y_2 - Y_1) - Y_{plane}(1)}{d_y}\end{aligned}\tag{3.10}$$

Knowing the pixels and the ray lengths for each of them makes the application of the radiological path equation (Equation 3.1) trivial. From another perspective, Siddon's algorithm produces an even more important piece of information. One gets total geometric knowledge of the tomographic assembly. If matrix form, this is called the system matrix, and it is an essential part of the application of any iterative algorithm.

Figure ?? aims to graphically explain the formation of this matrix. Each line in the matrix can be thought of as a flattened matrix of the same size as the tomographic image to reconstruct. There are as many of these lines as there are rays in the tomographic assembly. Each element of the matrix contains the length of the ray corresponding to each line, as it is calculated (through the application of Siddon's algorithm) for the corresponding pixel of the aforementioned flattened matrix.

### 3.1.1.1 Exit Point Calculation

Figure 3.4 is a schematic snapshot of a point in which the drone is taking a spectrum in one of its stops. Here, the drone's position ( $P_1$ ) is given by the distance  $D$  and the angle  $\beta$ . The gimbal is pointing at a direction at an angular distance of  $\gamma$  from line  $0P_1$ . Point

$P_2$ , which is not known, is at the intersection between the trajectory's circumference and line  $P_1P_2$ . Now, any point on this line can be expressed parametrically, with the sum of a point and a vector; while to say a point is on a circumference is the same as saying the distance between that point and the centre of this circumference is equal to its radius. The situation can be described by the expressions in Equation 3.11.

$$\begin{aligned} X &= P_1 + t \cdot (P_2 - P_1) \\ |P_2| &= D^2 \end{aligned} \quad (3.11)$$

Unravelling these expressions, and making use of the algebraic property that says that  $|A|^2 = A \cdot A$ , the expression becomes a second degree equation, as stated in Equation 3.12, writing  $P_2 - P_1$  as  $V$ .

$$t^2 V^2 + 2 \cdot V \cdot P_1 \cdot t + P_1^2 - D^2 = 0 \quad (3.12)$$

If line  $P_1P_2$  non-tangentially intersects the circumference, solving Equation 3.12 renders two values for  $t$  (which correspond to  $P_1$  and  $P_2$ ). Selection is made by determining the returned value of  $t$  which maximises the euclidean distance between the produced point and  $P_1$ .

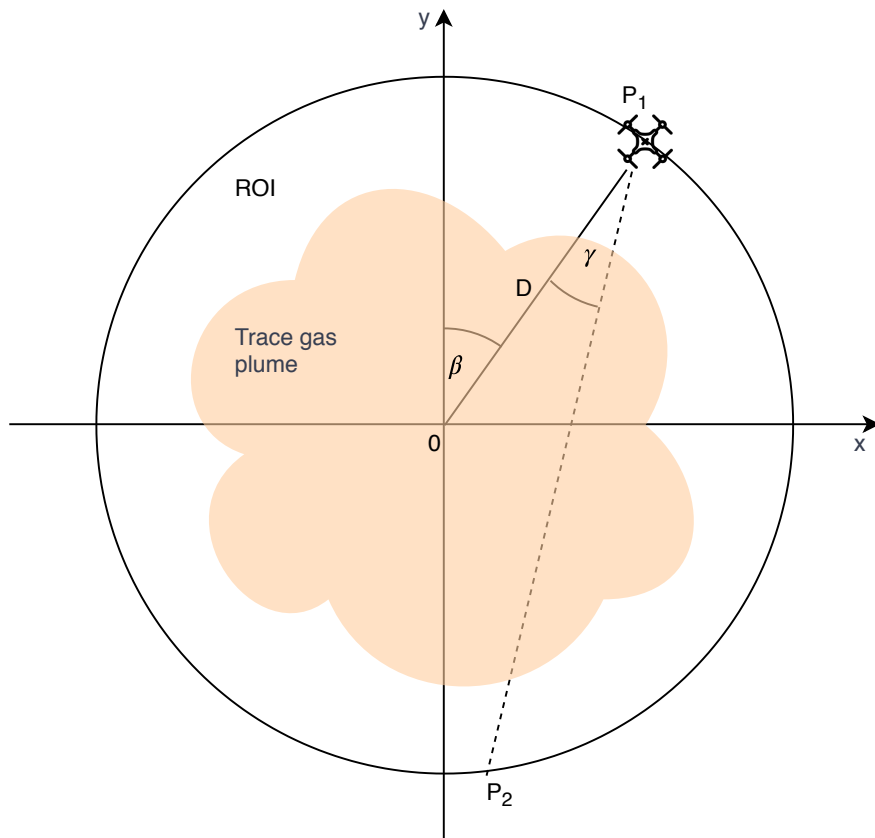


Figure 3.4:  $P_2$  Calculation. The software uses the position of the drone, as defined by the vertical angle,  $\beta$ , and the distance between the drone and the centre of the trajectory,  $D$ , to determine  $P_2$  through the solution of a second degree equation.

### 3.1.2 Phantoms

A phantom is a device that represents the human body or some of its parts. They have been used in medical physics since the beginning of the field. In medical imaging, for instance, phantoms started being used in the late nineteenth century and early twentieth century. At the time, it was very difficult to find volunteers for any kind of experiment that involved radiation, due to the common effects that were rapidly reported by the first people subject to this kind of intervention [25]. In spite of this difficulty, scientists and researchers still had to determine the dosimetry properties and physical limitations of their radiative devices, so medical physicists had to develop their own test models, or phantoms, for this effect. More recently, phantoms have been designed to develop computed tomography applications and algorithms. These phantoms mimic the body's attenuation properties in the X-Ray section of the electromagnetic spectrum, for instance.

Although the system that I propose does not aim at measuring or using the human body (or any other animal's), the concept still stands. To evaluate our reconstruction methods and the validity of our data gathering strategies, I needed an atmospheric phantom.

The distribution of gases in the atmosphere is completely different from biological tissue. Therefore, medical imaging phantoms were not adequate. The design that I have created is based on the premise that a two-dimensional Gaussian peak is more appropriate to describe the smoother nature of gaseous distribution [77]. This in contrast with the crisply defined edges of a medical tomography phantom such as Shepp-Logan's head phantom [74].

To design the phantom itself, I used a library called TomoPhantom [48], a tomographic phantom generator that provides a Python [Application Programming Interface \(API\)](#), making it trivial to include in the Tomosim simulator. The new phantom is comprised of 5 Gaussian profiles, depicting a static gas mixture. An ellipse is also in the phantom, near one of the corners. This serves mainly as a reference point for reconstruction, given its more solid and crisp nature. The new phantom can be seen in Figure 3.5 and its features are stated in Table 3.1.

Table 3.1: Table summarising the new phantom's construction details, as a sum of 5 Gaussian profiles and an ellipse designed using TomoPhantom. In this table, Co is the object's amplitude, Xo and Yo are its center coordinates, and a and b are the objects half-widths. The table is constructed using TomoPhantom's particular syntax and more information can be obtained at [48].

Type	Co	Xo	Yo	a	b	Angle
Gaussian	1	-0,1	-0,1	0,25	0,5	-45
Gaussian	1	0,6	0	0,65	0,45	-45
Gaussian	1	-0,6	-0,4	0,8	0,8	0
Gaussian	1	-0,4	0,8	0,7	0,7	0
Ellipse	1	0,4	-0,8	0,3	0,15	0

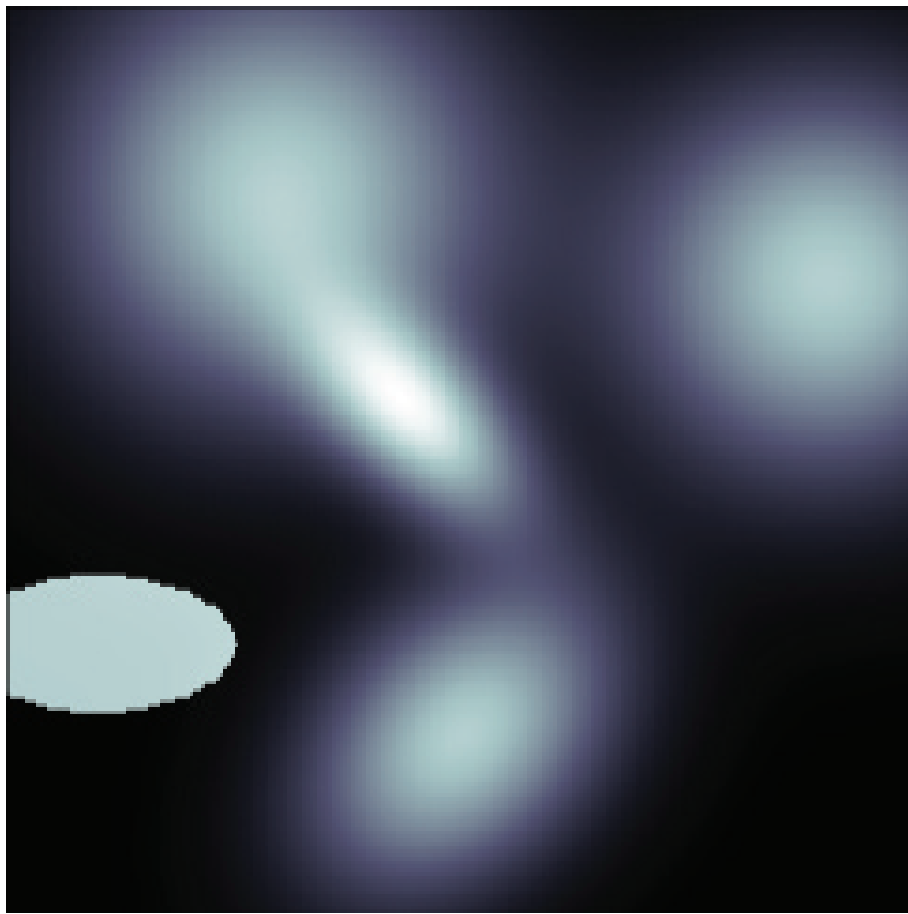


Figure 3.5: A graphical representation of the new spectral phantom, custom built for the TomoSim application.

### 3.1.3 Error Estimation

Error sources for the Tomosim simulator come in four different natures: time errors, geometric errors, spectroscopic errors and reconstruction errors.

Time errors come from the fact that there are two moments of measurement. In a dynamic system, the time that passes between the two is enough for concentrations to change significantly. Tomosim does not address these errors, because they can be eliminated by the introduction of a second drone carrying the same type of equipment, which would eliminate said time difference.

Geometric errors exist due to the drone not being able to situate itself perfectly. There is always a positioning error, no matter how sophisticated the onboard equipment is. This type of error is addressed in the simulation through a Monte Carlo like approach.

Positioning and pointing errors are assumed to have normal distributions. Each time a point is calculated by the drone, a normally distributed random number, with a mean of 0 and a standard deviation equal to the nominal error of the positioning system. This number is then added to the theoretical point. Figure 3.6 is a graphical representation of the reasoning behind the calculation of the geometric error. The image deals with two types of error. One comes from the [Real Time Kinematic Global](#)

**Positioning System (RTK GPS)** positioning system (the positioning error,  $\epsilon_p$ ); and the other that comes from the gimbal (the pointing error,  $\epsilon_\gamma$ ). The two  $\epsilon$  values are the nominal error for the positioning and the pointing devices. The error is introduced in the simulation through the values of  $\beta$  and  $D$  (see Figure 3.4) while calculating  $P_2$ . Given the very low nominal error for the gimbal, the small angle approximation is valid ( $\sin \theta = \theta$ ). This is used to determine the theoretical value of  $P_2$ , located on the device's circular trajectory. Finally, the software adds the positioning error, using the same process as in  $P_1$ 's case. The error depiction in Figure 3.6 is extremely exaggerated for visibility.

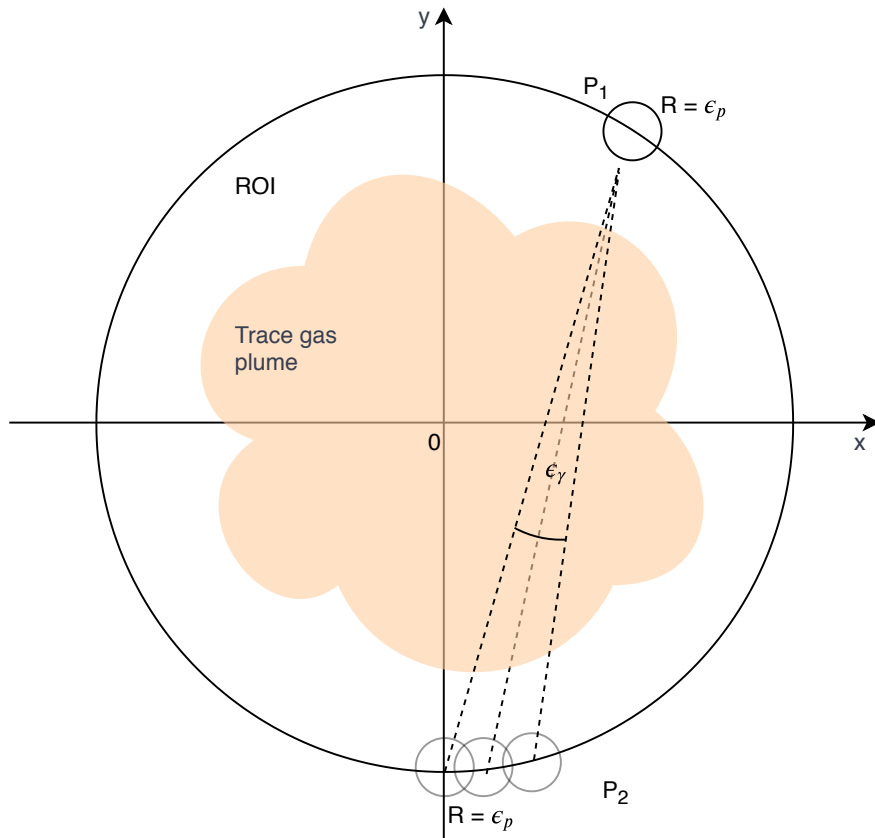


Figure 3.6: Error estimation graphical representation. Note errors are extremely exaggerated for visualisation purposes.

The third type of error are the spectroscopic errors. These come from the spectroscopic equipment that is used to gather projections. To take this noise into account, the simulator adds a Gaussian noise spectrum to each measurement, which is configurable through its standard deviation, as was previously done in [78]. This is a valid approach, insofar as the captured spectra are perfectly calibrated regarding spectral shift and squeeze. Since this is a simulation software, this is an acceptable assumption.

The final type of error that the system needs to contend with is the reconstruction error. In tomographic inversion problems, it is common to use techniques such as the **Mean Squared Error (MSE)** as a metric for an algorithm's performance. Tomosim was also evaluated in this light and in two separate ways. The first was to calculate the **MSE** for each pixel of the whole image. This information can still be viewed as an

image (it is a two-dimensional grid of values) and paints an immediate picture of the general behaviour of the reconstruction algorithm. Moreover, it can tell the viewer if there are any types of shapes or areas in which the algorithm has more difficulties. The second way of using MSE to evaluate the reconstruction is to calculate a score through Equation 3.13. In this equation, and with respect to this simulator,  $f$  is the original image and  $g$  the one reconstructed from projections.

$$E = \sqrt{\frac{\sum |g(x, y) - f(x, y)|^2}{\sum |f(x, y)|^2}} \quad (3.13)$$

### 3.1.4 Reconstruction Results

Until now, this section was dedicated to explaining the theoretical and computational aspects of the TomoSim software program. In this subsection, I will focus on the results that it produced, namely in what concerns the tomographic reconstruction of an image based on the concentration of selected atmospheric trace gases.

In TomoSim, a projection is the sum of the pixel lengths (the lengths of the rays that traverse each pixel) for each ray and for the grid mentioned in Section 3.1. Unlike a real life situation, the contents of the ROI are completely known and correspond to the phantoms also described in Section 3.1 multiplied by a given maximum number of molecules. Siddon's algorithm is used in this process, and the final results of its application are the sinogram and the system matrix. Figure 3.7 contains some examples of these matrices, before and after the resorting operation described in the last lines of Section 2.4.

Images corresponding to the trace gas distribution within the ROI were reconstructed using iterative and analytical methods. In Figure 3.8, one can see the reconstruction results for the three tested methods when applied to the new spectral phantom; Figure 3.9 shows the graphical representation of the reconstruction errors for the spectral phantom and is accompanied by Table 3.2; and in Figure 3.10, a comparison between reconstructions with different  $\Delta$  values is presented, also for the new spectral phantom.

Table 3.2: Reconstruction error table for the new spectral phantom at several projection intervals. The MLEM routine used pure fan-beam data while the other two used resorted parallel information. Errors presented were calculated using the Root Mean Square Errors, normalised to the range of the reconstructed image.

<b>Algorithm</b>	<b>Projection Intervals</b>				
	<b>1</b>	<b>2</b>	<b>3</b>	<b>4</b>	<b>5</b>
<b>FBP</b>	0,2365	0,2408	0,2609	0,2948	0,3465
<b>SART</b>	0,2225	0,2278	0,2771	0,3537	0,3302
<b>MLEM</b>	0,8705	0,9723	0,9986	0,9744	0,9890

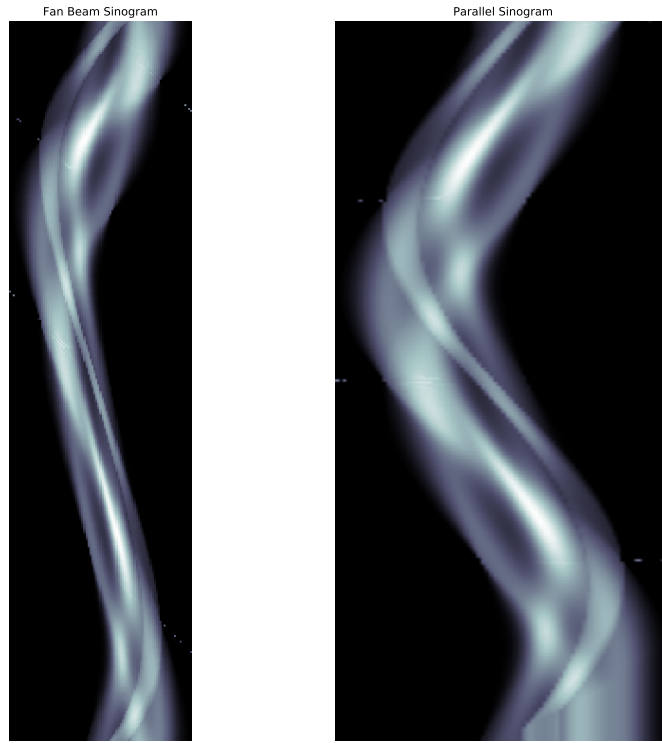


Figure 3.7: Sinogram examples: the new spectral phantom projection data at a projection interval of 1 degree. On the left, the projection data before resorting; on the right, the parallel projection data obtained after resorting the fan-beam line integrals.

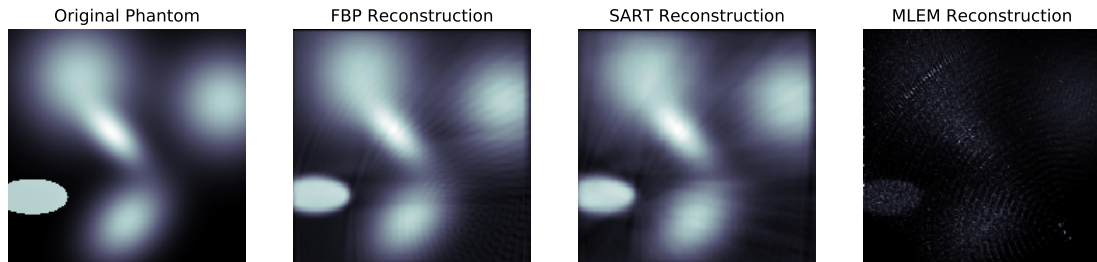


Figure 3.8: Tomographic reconstruction results, projection interval of 1 degree. From left to right: original phantom, FBP reconstruction, SART reconstruction, MLEM reconstruction

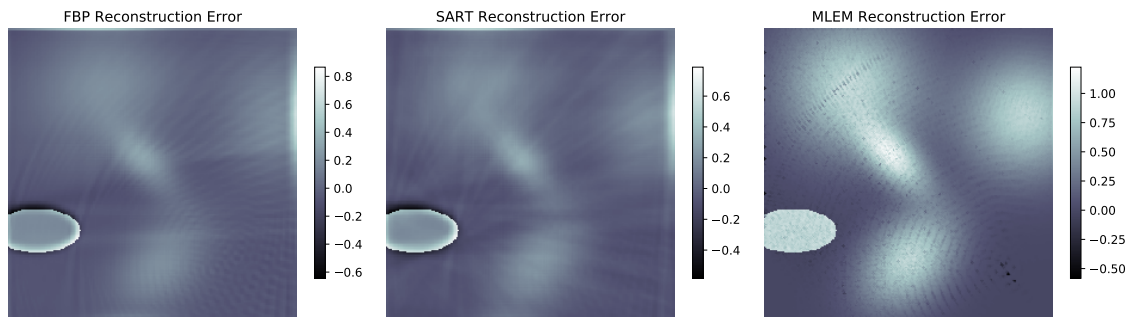


Figure 3.9: Tomographic reconstruction errors. Each one of these images was constructed by subtracting the respective reconstruction matrix, displayed in Figure 3.8, from the original phantom matrix. Error value is normalised to the pixel values, i.e., 32 bit floating point numbers with values between 0 and 1.



Figure 3.10: Reconstruction degradation: the projection interval was crucial for reconstruction. Note the image degradation going from a projection interval of 1 degree to 5 degrees (left to right). Images reconstructed using the FBP algorithm.

## 3.2 The Experiment

As stated in this chapter's introductory notes, this thesis main body of work revolves around two base assumptions, our hypothesis. The first one, about the information capturing by the idealised system, was addressed in Subsection 3.1.1. The second, more physical in nature, is the subject matter of this section. Our hypothesis states that the light absorption between points  $A$  and  $B$  (let's call it  $A_{AB}$ ) should be equal to the difference of the absorptions in  $A$  and  $B$ . We can write this, in a *Lambertian* manner as in Equation 3.14.

$$I_B = I_A \cdot \exp \left[ -AB \cdot \sum_i \sigma_{ABi} \cdot c_{ABi} \right] \quad (3.14)$$

This is to say that the light intensity reaching point  $B$  is given by the intensity reaching  $A$ , exponentially decreased by the absorbers at interval  $AB$ . The intensities at  $A$  and  $B$  are written as in Equation 3.15.

$$\begin{aligned} I_B &= I_0 \cdot \exp \left[ -L_B \cdot \sum_i \sigma_{Bi} \cdot c_{Bi} \right] \\ I_A &= I_0 \cdot \exp \left[ -L_A \cdot \sum_i \sigma_{Ai} \cdot c_{Ai} \right] \end{aligned} \quad (3.15)$$

If we join all this information in the same expression, the equation is transformed into its final form, presented in Equation 3.16.

$$I_0 \cdot \exp \left[ -L_B \cdot \sum_i \sigma_{Bi} \cdot c_{Bi} \right] = I_0 \cdot \exp \left[ -L_A \cdot \sum_i \sigma_{Ai} \cdot c_{Ai} \right] \cdot \left[ -AB \cdot \sum_i \sigma_{ABi} \cdot c_{ABi} \right] \quad (3.16)$$

Equation 3.16 can be greatly simplified: we take the natural logarithm of both sides and we state that  $\sum_i \sigma_{Xi} \cdot c_{Xi} = S_i$ . These operations result in the simplified form of Equation 3.17.

$$L_B \cdot S_B = L_A \cdot S_A + L_{AB} \cdot S_{AB} \quad (3.17)$$

Now,  $L_X \cdot S_X$  can be thought of as the wavelength dependent light absorption in path  $X$ . In this case, the wavelength interval is always the same. We can therefore conclude that, theoretically, our hypothesis is valid: light absorption between points  $A$  and  $B$  can be expressed in terms of the absorption on both these points and corresponds to their difference.

Although mathematically this seems clear-cut, in the real world things can become more problematic, since we have to deal with the imperfections that characterise a real physical system. Noise, instrumental limitations, adverse environmental effects, etc.. The experiment we describe in the next few paragraphs aimed at determining target trace gas concentration in a set analysis field. This field is dimension-wise compatible with those that would be employed in the final working system. This experiment is represented in Figure 3.11.

The goal of the experiment was to compare passive and active DOAS measurements performed with a very short time difference between them. The passive measurement

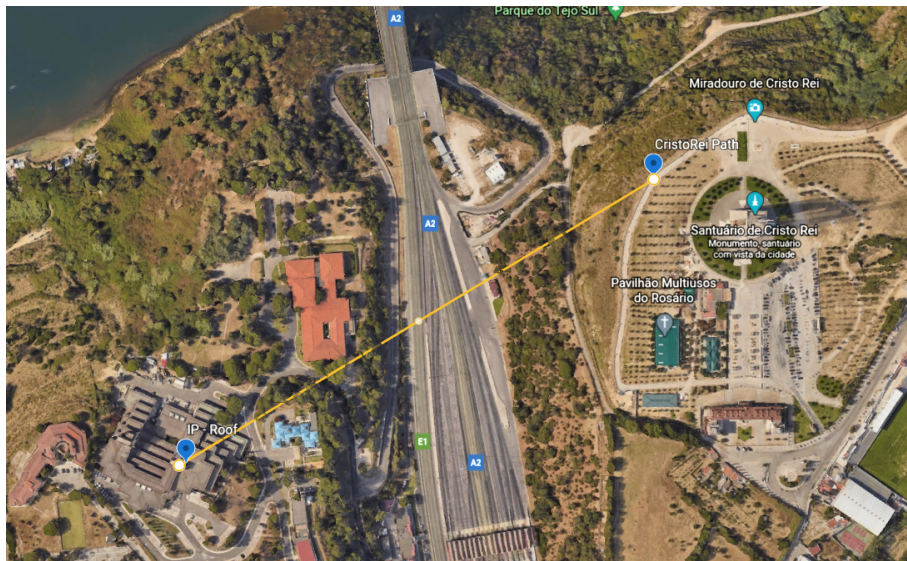


Figure 3.11: Location of observer points for the physical experiment.

would employ the same acquisition strategy as the drone is expected to use. This comparison will be used to test our second hypothesis.

Finding two appropriate experiment sites proved to be the first difficulty: both telescopes should see sky on the back of the other telescope. Otherwise, the contribution from the terrain's reflection would have to be taken into account and the experiment conditions would be very different from the ones the drone will have. There are not many site pairs that provide this, and most of the ones that exist are private and authorisations are not easy to obtain. In the end, we managed to run the experiment in the facilities of *InfraEstruturas de Portugal (IEP)* and the *Cristo-Rei* sanctuary, near our own base.

### 3.2.1 Protocol and conduction

The experiment involved two different optical assemblies, which are summarised in Table 3.3. Both assemblies play two roles, which reflect the comparison between active and passive that is the entire aim of the test. To simplify, we will address the two as West Bank and East Bank. The West Bank is, as the name implies, the assembly that is placed further West, i.e., the one that is installed on IEP's roof. By exclusion, the East Bank assembly is the one placed on the sanctuary. The West Bank assembly is comprised of a telescope and tripod, a spectrometer (with the necessary fibre optics attached) and a laptop.

The East Bank assembly has exactly the same parts, but in addition to them, it features a hand-held torch that sports an XHP50.2 CREE LED. The manufacturer states that this torch is capable of illuminating by itself up to a distance of 300 m and produces luminous flux of at least 1500 lm. By fitting this torch on the telescope's eyepiece channel, we are able to further collimate the light that it produces, making it reach much further distances than originally stated, and being easily picked up by the other telescope. This is plain to see in Figure 3.14. The light spectrum that pertains to the CREE LED in use is published in this device's datasheet, and presented in

## CHAPTER 3. METHODS

---

Figure 3.12, which largely corroborates the spectrum in Figure 3.13, taken by the same spectrometers that were used in the experiment, at a distance of approximately 50 m from the torchlight.

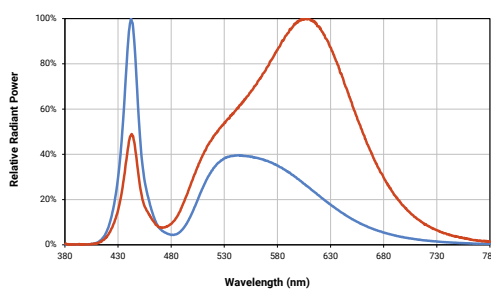


Figure 3.12: Published spectrum of the CREE XHP50.2 LED light. The LED that was used in this experiment corresponds to the blue line [20].

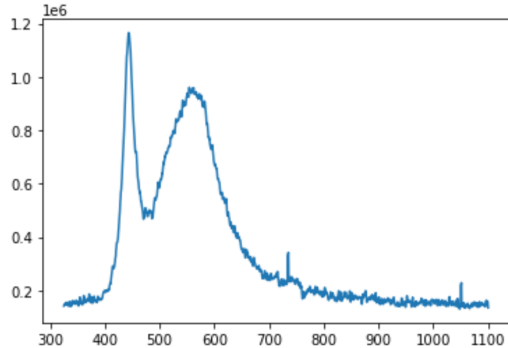


Figure 3.13: Spectrum measured with the experiment spectrometers, at a distance of approximately 50 m from the torchlight.

Table 3.3: Summary table for the two experiment assemblies. Note the difference in terms of material, due to the two different roles both assemblies play during the experiment. This is translated into not having the need of an artificial light source in the West Bank's assembly.

	West Bank	East Bank
<b>Spectrometer</b>	Avantes USB 2048 channels	Avantes USB 2048 channels
<b>Telescope</b>	Meade ET90	Meade ET90
<b>Artificial Light Source</b>	N/A	Goobay CREE XHP50.2 torch
<b>Laptop</b>	Windows 10 laptop	Windows 10 laptop
<b>Software</b>	AvaSoft 8.11	AvaSoft 8.11

The experiment itself is scheduled to start at around 06:00 A.M.. It consists in capturing spectral measurements in both modes (active and passive) periodically, with the least amount of time possible between measurements in the same capture. In this case, I am calling capture to a particular group of actions that are defined in Table 3.4. Captures are defined according to the time at which they are run, and are summarised in Table 3.5. Closing time for this experiment was set on 11:00 A.M.. This time window ensures measurements are taken during sunrise and until after the morning rush hour is over.

As displayed in Table 3.3, the spectrometers are both the same model, manufactured by Avantes and with 2048 channels, powered through the same [Universal Serial Bus \(USB\)](#) cable that is used for data transfer. The spectra are acquired through Avantes' own collection software, AvaSoft 8. The spectrometer are configured to have an integration time of 20ms and immediately store every measurement on an [American Standard Code for Information Interchange \(ASCII\)](#) file. With the kind of lighting conditions that we are dealing with, this integration time allows us not to worry about saturation. However, to build usable spectra we need to sum the collected files. This

Table 3.4: Actions are the indivisible unit upon which each capture is built. The prescribed actions for this experiment are described in this table.

Action ID	Action	Description
A	Active trace gas concentration determination	With the two telescopes facing each other, we collect spectra for two minutes with the light source turned off and another 2 min with the light source turned on.
B	Passive trace gas concentration determination	With the two telescopes aligned and approximately facing West, we collect spectra for 2 minutes.
C	Passive reference collection	The West telescope points upwards and collects data for 2 minutes.

Table 3.5: Captures are particular sets of actions that are conducted according to a specific order, depending on the time of day on which the capture is run. This table describes the prescribed captures on which this experiment consisted.

Time Frame	Period	Action
05:00 - Sunrise	15 minutes	A
Sunrise	Once	C
Sunrise - 11:00	15 minutes	A and B

is valid because given the very little time it takes to make a measurement (2 minutes), the sun can be considered a constant light source, and therefore we can consider the photons to have a Poissonian statistic distribution [30].

### 3.2.2 First Run

The first attempt at running this experiment took place on June 7<sup>th</sup> 2021. Weather conditions were optimal for this kind of measurement, with no wind, clear sky and very low optical density, as can be testified by Figure 3.14. The experiment started with a small delay, caused by a problem on the charger of the East bank laptop. Besides this delay, this was not a problem for the experiment itself. It was the other laptop's battery that did not hold enough charge for the experiment to reach its determined end, and there was no means to charge it on IEP's roof. Given this circumstance, we were able to retrieve spectral measurements from around 06:20 A.M. to 08:20 A.M., in a total of 6 measurements which are produced in Table 3.6.

On the one hand, it is clear from Table 3.6 that we do not have data on the active baseline spectra <sup>3</sup> (likely due to some operation error); on the other hand, we have too few data points to make any claim of validation or refutation of the principle we were to measure. It was thus clear that another run was necessary to get the necessary results.

<sup>3</sup>In this case, the baseline spectrum is one taken in the exact same direction and approximately simultaneously, with the light turned off to allow removal of solar contribution.

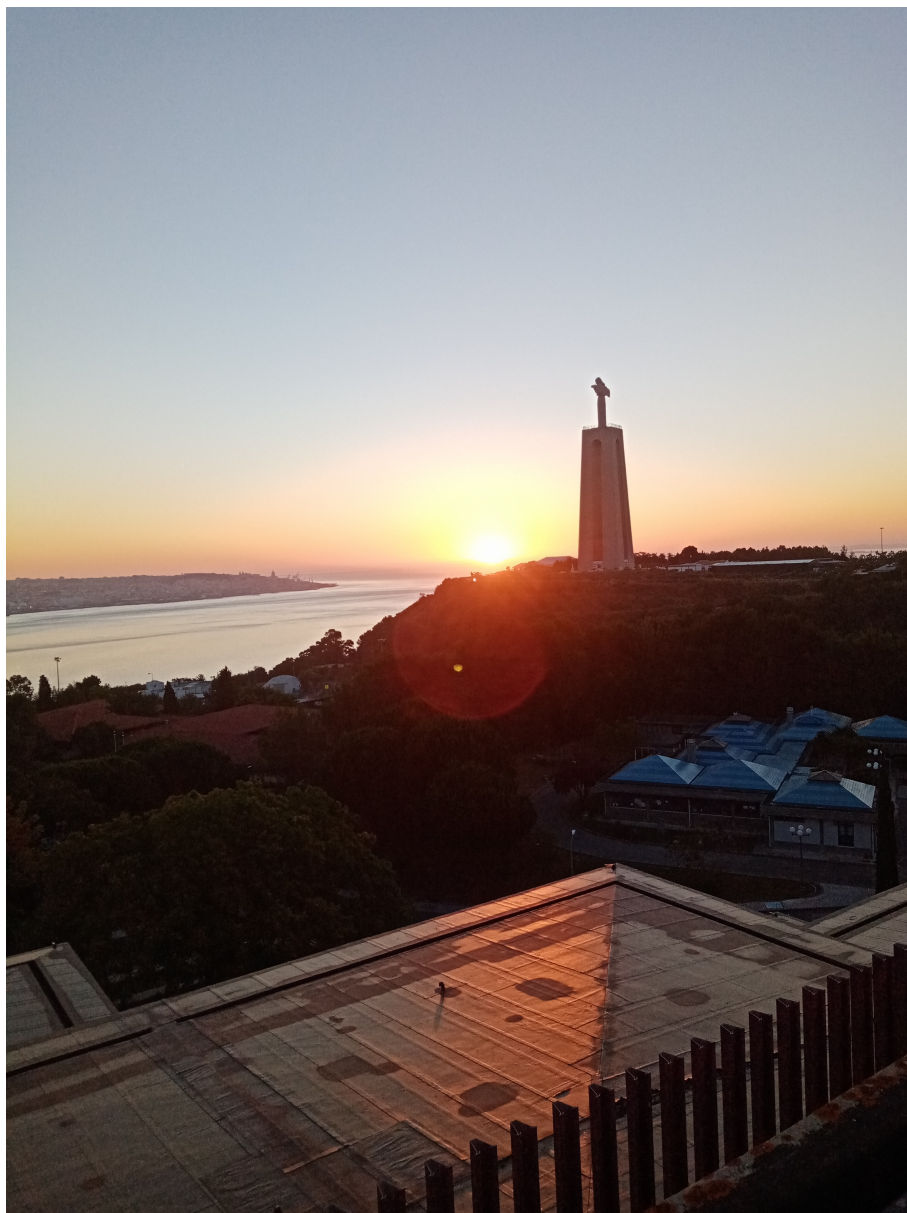


Figure 3.14: View from West Bank assembly at sunrise during the first run of the experiment. Note that even with the sun appearing in the back, the light from the torch is perfectly visible at this distance.

Table 3.6: First run: measurement table.

#	<b>Passive meas.</b>	<b>Passive ref.</b>	<b>Active mean.</b>	<b>Active ref.</b>
1	06:20	06:23	06:15	—
2	06:46	06:50	06:41	—
3	07:04	07:07	07:00	—
4	07:25	07:27	07:21	—
5	07:48	07:50	07:45	—
6	08:10	08:12	08:06	08:08

Although it was not possible to produce convincing results from these data, they were of good individual quality and allowed some preliminary analysis to be run. Using the first measurement as the reference spectrum, it was possible to calculate optical densities for each one of the measurement moments, as well as  $\text{NO}_2$  concentration. The graphical appearance of the optical density signal for each measurement is presented in Figure 3.15 and Figure 3.16, while the concentration chart for the various moments comprises Figure 3.17.

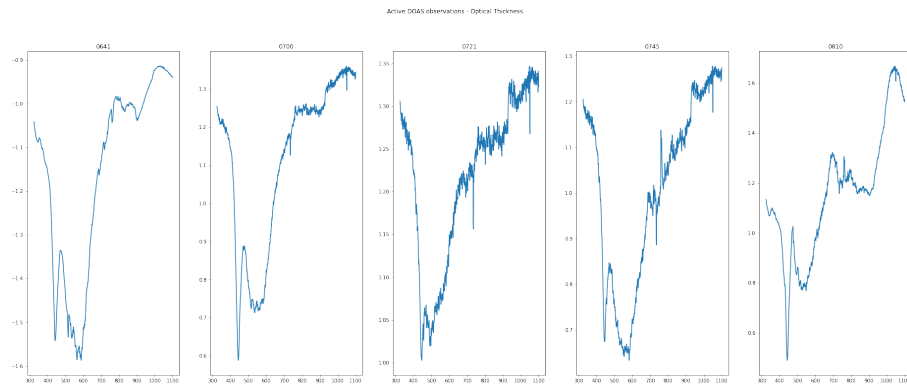


Figure 3.15: Optical densities calculated with reference to measurement #1 for the other measurement moments in the active DOAS mode.

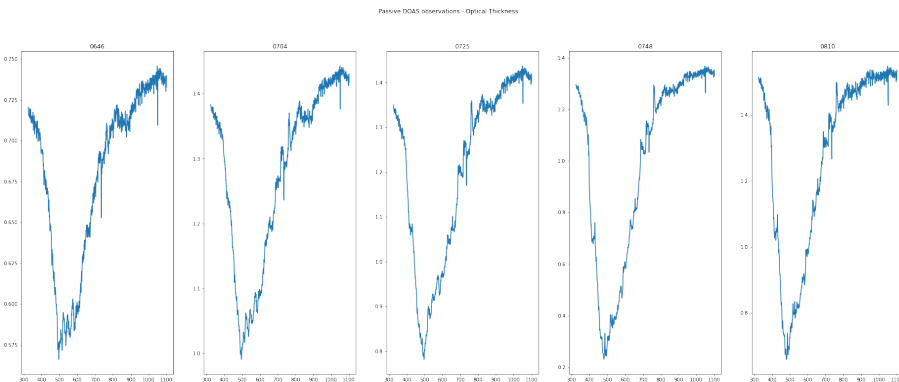


Figure 3.16: Optical densities calculated with reference to measurement #1 for the other measurement moments in the passive DOAS mode.

Although admittedly incomplete, these data allows some preliminary remarks. The first and most important one is that the highest concentration detected appears in the first measurement point for both active and passive modes. The passive mode measurement could be discarded because this measurement was taken during sunrise and the relevant spectra could be considered too noisy. However, its active counterpart produces the exact same result, as the chart in Figure 3.17 shows. The second data point had the lowest detected concentration, and from that point forward, the concentration evolves as expected (rising). One other remark that could be addressed towards this first stage analysis is that there seems to be a good agreement between active and passive measurements. This remark might be considered invalid, as there is no data for the active baseline. However, since this analysis was focused on  $\text{NO}_2$  concentration, and the relevant spectral window for this trace gas is usually between

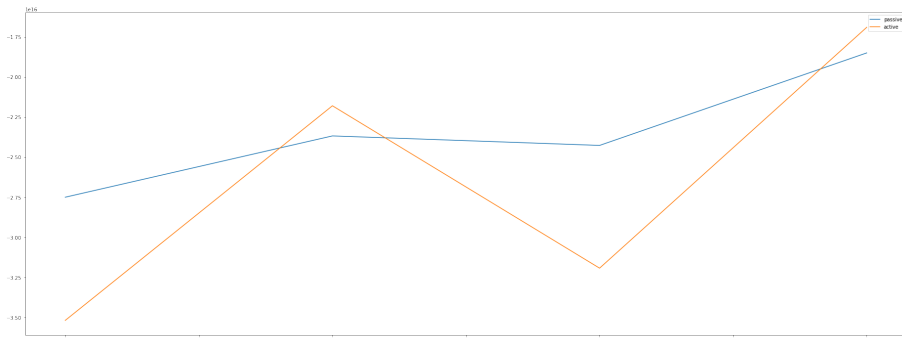


Figure 3.17: Calculated  $\text{NO}_2$  concentrations for the various measurement moments. Each integer in the horizontal axis corresponds to a moment, organized chronologically.

400nm and 500nm, this is not the case. In effect, the scattered-sunlight-originated photon counts in this interval will be always much smaller than the artificial ones, thus having an equivalently smaller influence in the final results.

### 3.2.3 Second run

The second run of this experiment took place on the 23<sup>rd</sup> of June. The weather was not as perfect as it had been in the first day, with a few scattered clouds dotting the sky, and a lot more wind. These clouds were on a completely different azimuth than the field of study, so they had no influence whatsoever on the results. The exact spot of the experiment also changed slightly. On the first run, the East bank assembly was closer to the western limit of the sanctuary. This run was conducted putting the East bank assembly farther to the East. This change improved (but also made more difficult) the artificial light measurements, by providing a better background. It also improved operational conditions, decreasing human error probability. This position difference is illustrated in Figure 3.18.

Unlike the first run, the second run started without any logistic hiccup, on time, and we were able to continue measuring until 10:00. The total number of measurements reached 12. This was slightly under the 16 target measurements, but much better than what we had achieved in the previous day. Table 3.7 contains the time for each of the performed spectral collections.

Spectroscopically, the collected data were of good quality. Unfortunately, in terms of the experiment itself, some had to be discarded. This is chiefly true with regard to the artificial light portion of the experiment. With the change in position described in the previous paragraph, the light came to fill a much smaller visual slice than in the first run. This meant that it was much more difficult to pick up the torch with the telescope on the West bank. Although I have tried to align both telescopes in order to only capture the light that I was interested in, in more than one occasion, this alignment was (probably by the wind) destroyed. Since the light was so small in comparison with the field of vision, the final resulting spectrum is one of the background instead of the torch. In the end, only 8 measurements were viable. Analytical parameters are found in Table 3.8. Figure 3.19 and Figures 3.20 are plots of the measured concentration of  $\text{NO}_2$ . Figures 3.21, Figure ?? and Figure ?? are the plots showing the actual DOAS fits.

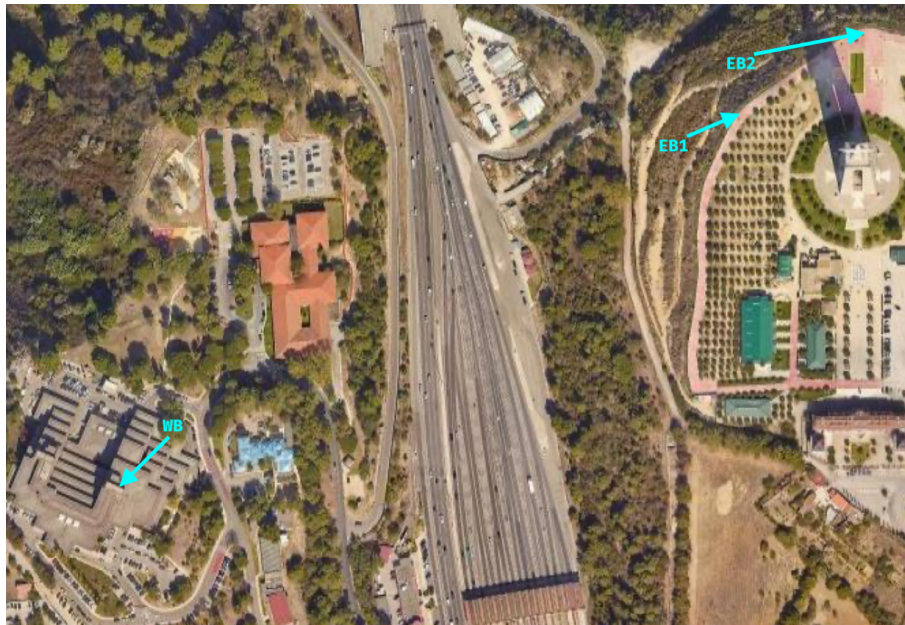


Figure 3.18: This image, built using Google Maps, illustrates the East Bank relocation that took place in the second leg of the experiment. The first location is presented as EB<sub>1</sub>, while the second is naturally EB<sub>2</sub>. The West Bank is also presented for some geographic reference, and identified by WB.

Table 3.7: Second run: time of measurements table.

<b>Active</b>	<b>Active Reference</b>	<b>Passive</b>
06:07	05:57	06:14
06:35	06:30	06:40
06:50		06:50
07:10	07:15	07:00
07:50	07:40	07:10
08:08	08:03	07:25
08:18	08:21	07:53
08:35	08:30	08:35
09:00	08:53	09:02
09:45	09:50	09:24
10:00	10:05	09:53

Table 3.8: Parameters for the DOAS measurements relative to the second run of the experiment.

Parameter	Value
Analysis Window - Active Experiment	[400, 450] nm
Analysis Window - Passive Experiment	[430, 455] nm
Order of Filtering Polynomial	2
Spectral Resolution	2.4 nm

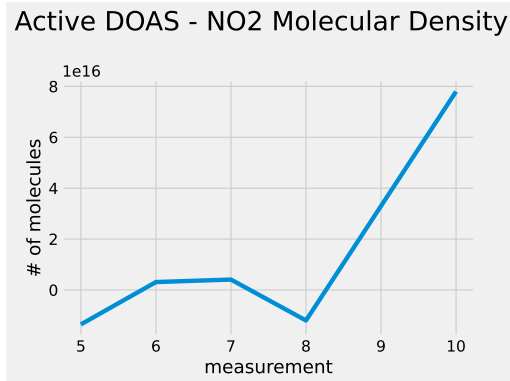


Figure 3.19: Active DOAS molecular density for  $\text{NO}_2$ , varying with the measurement number.

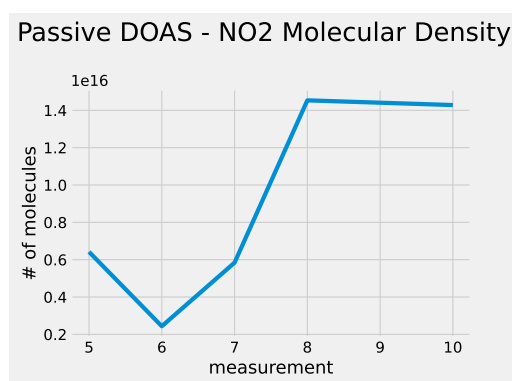


Figure 3.20: Passive DOAS molecular density for  $\text{NO}_2$ , varying with the measurement number. Note that this is the difference between the density obtained at the two experiment assemblies, as per hypothesis 2 (see 4.2).

### 3.2.4 Data Processing

While the rest of this section is dedicated to the gathering of spectral data and even the results that it returns, it is important to mention and to provide a (brief, high level) description of what is being done to said data.

AvaSoft, Avantes' spectrometer handling software application, allows one to store collected data in several formats. Most of these formats are binary in nature. These are more compact in terms of occupied disk space and are commonly used in this kind of application because spectra are most likely being collected for later processing through another computer program. However, they are not good if one needs to quickly check if the data are being correctly gathered or to see if there was any kind of operation error in the collection process, since they are completely unintelligible for humans. For this purpose, Avantes make the Avantes ASCII file format available. This is, as its name might imply, an ASCII formatted file that can be quickly inspected by anyone that can read the English language and understand the Latin characters. The files have a particular structure which is illustrated by Figure 3.24.

Some light string parsing operations are the compromise that is required to use this kind of file format in analytical software. In the case of this thesis' application, the files are opened and parsed using an OOP approach that takes advantage of the

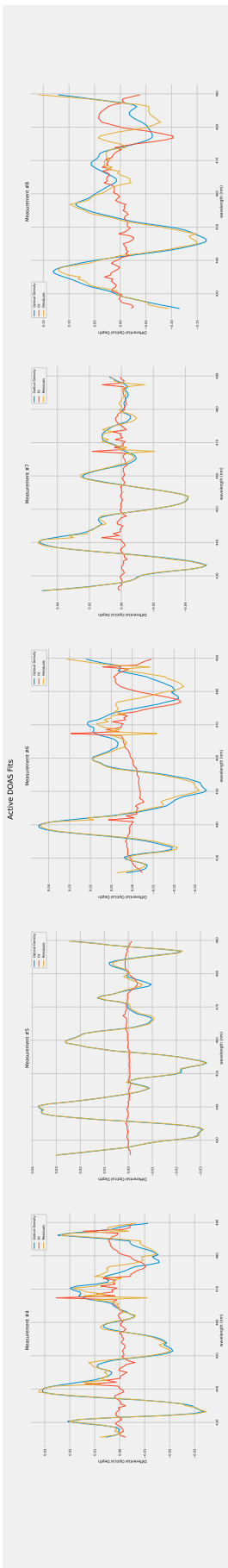


Figure 3.21: Active DOAS fit results. Each plot corresponds to one measurement moment.

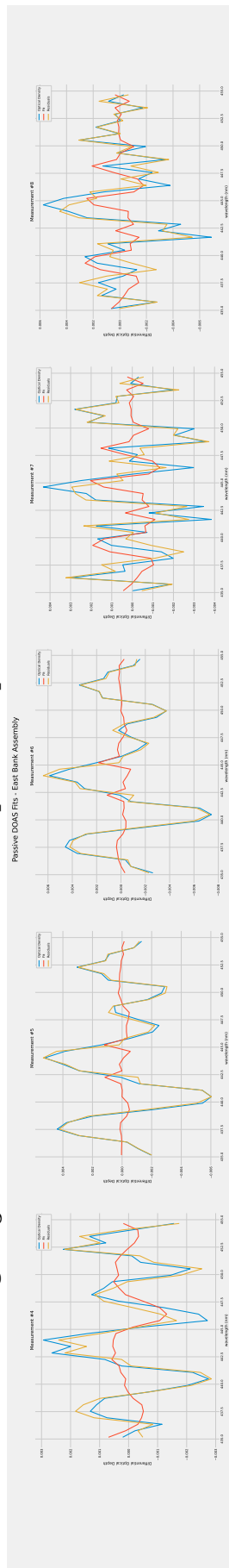


Figure 3.22: Passive DOAS fit results, from the system on the East Bank. Each plot corresponds to one measurement moment.

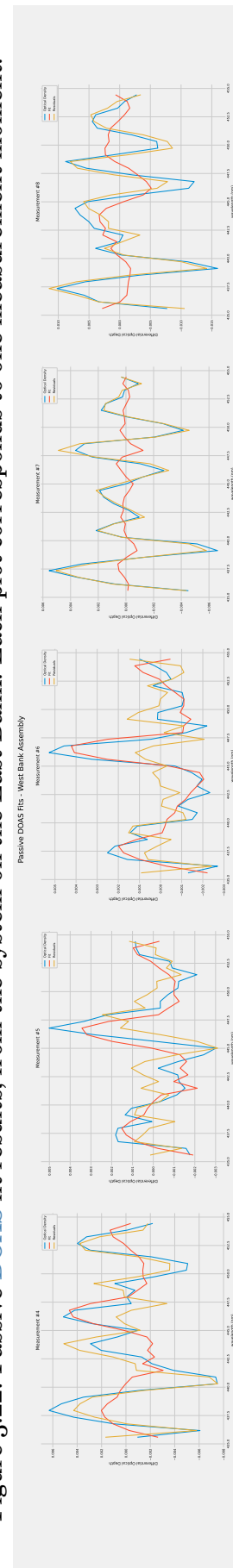


Figure 3.23: Passive DOAS fit results, from the system on the West Bank. Each plot corresponds to one measurement moment.

## CHAPTER 3. METHODS

---

```
1 0606013U1_07Jun21_064745_0007.Raw8.txt
0
1 Integration time [ms]: 120,000
2 Averaging Nr. [scans]: 1
3 Smoothing Nr. [pixels]: 1
4 Data measured with spectrometer [name]: 0606013U1
5 Wave ;Sample ;Dark ;Reference;Scope
6 [nm] ;[counts] ;[counts] ;[counts]
7
8 324,829; 2056,000; 0,000; 0,000
9 325,424; 2070,667; 0,000; 0,000
10 326,019; 2080,000; 0,000; 0,000
11 326,613; 2085,333; 0,000; 0,000
12 327,208; 2096,000; 0,000; 0,000
13 327,803; 2098,667; 0,000; 0,000
14 328,397; 2117,333; 0,000; 0,000
15 328,992; 2100,000; 0,000; 0,000
16 329,586; 2096,000; 0,000; 0,000
17 330,181; 2085,333; 0,000; 0,000
```

Figure 3.24: The Avantes ASCII file format. This is a screenshot of a file of this type opened in the VIM text editor. Note its particular structure, around which the file / folder parsing objects described by Figure 3.26 and Figure 3.27 are constructed.

organisational structure of the several files involved in the process. Each file originates an AvantesASCII object, which loads the data, parses its values and stores them in a Pandas DataFrame internal object <sup>4</sup>. For each folder that contains this kind of file, the parsing library creates an AvantesASCIIFolder object, which loads all files inside that folder and runs global data operations such as summation and integration-time-normalisation. A general schematic of this approach is provided in Figure 3.25, while a flowchart for the file loading routine is presented in Figure 3.26 and the folder loading process is illustrated by Figure 3.27.

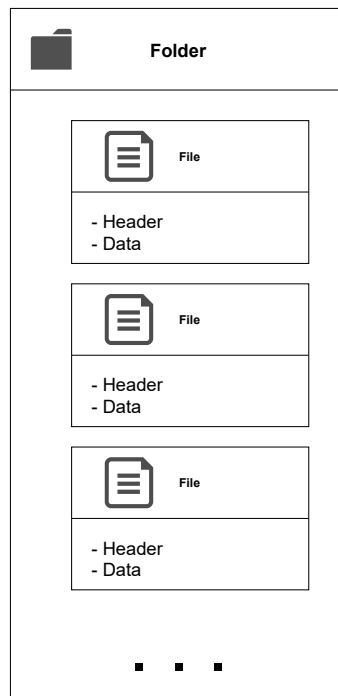


Figure 3.25: The Data processing. The OOP approach that was taken attempts to take advantage of the organisational structure of the spectral data, by modelling it into Python objects.

<sup>4</sup>Pandas is a data processing library used in Python that provides a very efficient way to access and manipulate tabular data by leveraging the use of C code through Python commands.

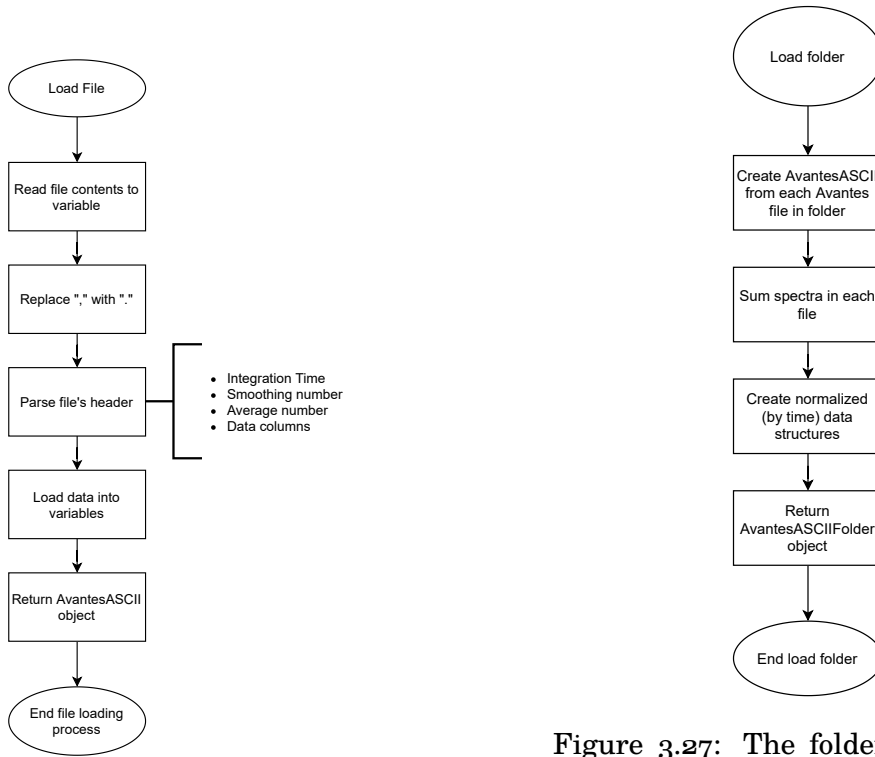


Figure 3.26: The file loading process. An Avantes ASCII file originates an AvantesASCII object, which besides a series of string-parsing operations stores the data in a Pandas DataFrame, for easy access and control.

Figure 3.27: The folder loading process. Each folder can have many files. The way in which the data is gathered (described in Subsection 3.2.2) requires some global operations performed on groups of files, like summation and normalisation (with reference to the integration time). The AvantesASCIIFolder object provides such operations.

### 3.2.5 The DOAS Library

The **DOAS** software library is a Python package developed specifically for this thesis data processing operations. It was, as other components, designed using an **OOP** approach and following the SOLID principles of **Object Oriented Programming**. This piece of software was written in response to the initial research that I undertook and that returned no usable results in terms of modular, compact Python libraries for **DOAS** applications, that I could use in my work. It is, as far as I know, the only **DOAS** solving application with this kind of structure.

The library (**Unified Modelling Language (UML)**) diagram presented in Figure 3.28) models a **DOAS** application through the instrumentation lens. A **DOAS** application is always parametrised through its spectrometer’s physical features and limitations, which in turn determine the structure of the analysed spectral data, and even the differential cross sections of the trace gases that are to be studied. Of course, this library is much more limited in its capabilities than some specific programs that have become commonplace in this kind of application, such as QDOAS [21], but the fact that it can be operated through a Python program and that one can manipulate the data

## CHAPTER 3. METHODS

---

through such tools as Pandas DataFrames more than make up for this lack. Moreover, since it is in effect a software library, it is also as flexible as one is willing to expand it.

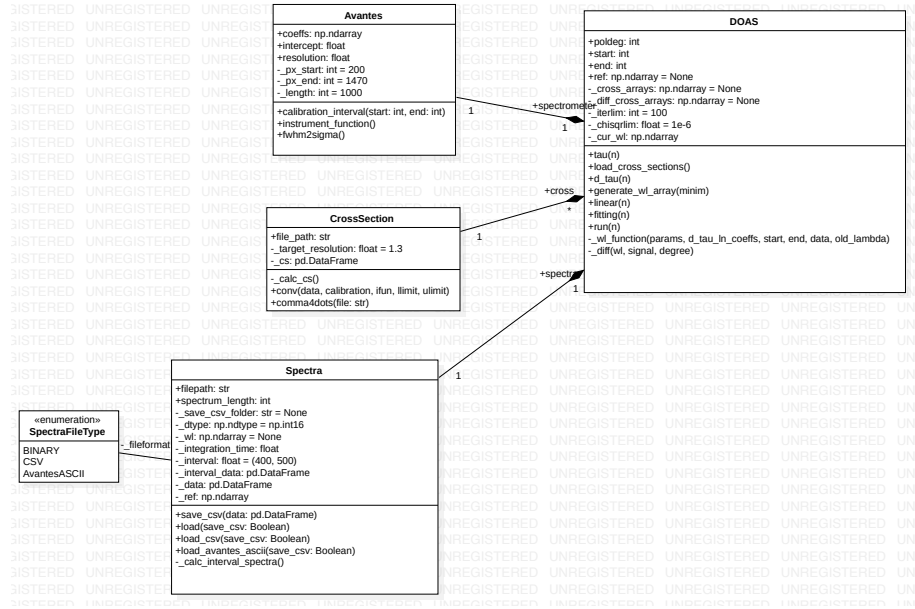


Figure 3.28: UML diagram for the **DOAS** library. The **OOP** approach that was followed allows for an instrument-oriented experiment parametrisation, which is not available in any other software

An important side note that attests to this library's relevance is that it has been fully integrated in FutureCompta's Bee2Fire software, with further developments being conducted through this team's efforts. This is the first commercially applicable result provided by the work in this thesis.

## DISCUSSION

### 4.1 First Hypothesis

Results presented in Section 3.1 raise a series of pertinent observations that should be addressed in discussion. The first remark goes to the fact that the number of projections used seemed adequate to perform the tomographic reconstruction in adequate fashion, although there are tomographic applications with many more projections (orders of magnitude more projections). This was not an unexpected result, as there are already several examples of studies in which a considerably lower number of projections was used, still producing satisfactory results [68]. Moreover, and since the simulation software automatically includes errors in the calculations, this number also proves that geometric error plays a very limited role in changing the result of the reconstruction due to the difference in size between the drone's trajectory and the geometric error, this was also a predicted result.

Even with the relatively low number of projections produced by the drone's trajectory and measurement strategy, all reconstruction algorithms were able to produce a reconstructed image that resembled the phantom that generated it.  $\Delta$ , the angular interval between projections, revealed itself to be crucial. This was expected as the number of captured projections is obtained by dividing 360 by  $\Delta$ . This is, also as expected, confirmed by the upward trend of the error when increasing the value of the angular projection interval, as can be seen numerically in Table 3.2 and qualitatively in Figure 3.10. With respect to the algorithms used, the custom-made MLEM routine produces clearly outlier results, which are not on par with the other two reconstruction methods used. This is plain to see both in Figure 3.8 and in Table 3.2, in which this algorithm's NRMSE is almost four times the second best result (FBP) for the smallest projection interval. This difference could to some extent be expected. SART and FBP algorithms were implemented using some of the most relevant and consistently used Python libraries (SciPy, for instance [87]). Given the amount of attention these libraries get from the scientific programming community, levels of optimisation are extremely high. Although it is nowhere near the other two approaches, the MLEM routine is still useful, as it is the only truly geometry-independent algorithm in this study (SART is also geometry independent, but this particular implementation expects a parallel projection sinogram as input).

As stated in Section 3.1.3, three different kinds of error influence the reconstruction

results: geometric, spectroscopic and reconstruction errors. The first kind of error is directly included in projection calculations, through the application of a Monte Carlo-like method to the geometry described in the same section. The second kind of uncertainty comes from the spectrum acquisition process itself, which is not perfect. If one considers there are no systematic errors present in the results, which is an acceptable premise in a simulation, then these errors can be simulated by the inclusion of Gaussian noise in the spectral measurements. This approach is based on the one used in [78], in which a Gaussian noise spectrum is added to the spectrum of interest in order to simulate how the error behaves with a degraded signal. Finally, reconstruction errors come from the finite precision of the calculations that render the images. These errors were presented in Subsection 3.1.4.

The three methods were also evaluated as to how they perform computationally, by measuring the time it took to produce the images in Figure 3.8 using a Paperspace P4000 cloud computing instance. In this regard, the fastest method was FBP, which took around 3 seconds to reconstruct. The second was MLEM, with around 50 seconds for 1000 iterations, and finally came SART, with 1 minute and 50 seconds for 1 iteration. One relevant observation comes from the fact that MLEM was significantly faster than SART, even taking into account the difference in optimisation, which was not an expected result and may indicate some reconstruction enhancing technique on SART's side, as the literature seems to indicate that this technique is faster than MLEM [24].

All things considered, the FBP algorithm produces a very good reconstruction, equivalent to SART's, while being more than 10 times faster, indicating that for this kind of application and with this kind of projection information, it is the best reconstruction algorithm.

## 4.2 Second Hypothesis

Read the first leg of the experiment again; add some official data; check to see if it plays out ok.

The proposed hypothesis was, as explained in Section 1.5, that one could obtain a trace gas' column density between two points by determining this value on both said points and then subtracting them one from another. Moreover, this was achievable with the kind of distances that the proposed monitoring system would be designed to use. To test this, I have setup an experiment comprising two spectroscopic assemblies. With them, I was able to test my approach against an active DOAS system. The expected results included similar levels of detected molecules for the passive and the active systems.

I defined the protocol and divided into measurements, which are comprised of sets of unitary actions. These actions included not only the measurements themselves, but also the collection of reference data for each measurement moment. In order to guide the conduction of the experiment, both on my behalf and on the volunteer's, a written protocol was created and made available to participants. This protocol constitutes an important part of Appendix ??.

The experiment was conducted in two "runs". The first run took place on 07/06/2021. A slight logistics-related delay complicated matters. The first measurement was taken at 06:20, some minutes after sunrise. Although meteorological conditions were optimal

and there were no hassles, work was interrupted at around 08:20, when the battery of one of the laptops that were being used ran out. The collected data on this first run were not as perfect as they seemed to be. An undetected operational error (with probable protocol breach) caused some of the data to be missing, and some of the collected spectra were "contaminated- meaning measurement interruptions were not correctly registered. This alone dictated the need to have another go at the experiment. Even with the missing data, I ran the processing routines on the data that existed. Part of the results were as expected, another part puzzling. The puzzling part was that the highest registered column density happened on the second measurement, before 07:00. After that, the number of detected molecules evolves as one would expect: rising with traffic intensity. The expected (and positive) part was that density evolution was the same for both the passive and the active DOAS systems.

The second run of the experiment happened later in the same month, on the 23<sup>rd</sup>. A new challenge came from the fact that the experiment's site was re-located to a better place (in terms of measuring capabilities), the alignment became more difficult, and revealed itself to be of paramount importance, rendering several measurements useless. Also, in this second day of experiments, there was a lot more wind than in the first day, which also played an important part in this alignment problem. With the 8 viable measurements that were left, I calculated molecular densities for NO<sub>2</sub> and gls03, which are displayed in Figure ???. The DOAS fits that led to these concentration values are also displayed, in Figure ???. Official numbers for NO<sub>2</sub> concentrations are provided by QualAR, a Portuguese public initiative that measures air quality throughout the country [agencia2019]. The QualAR chart for the relevant day is presented in Figure ??.

There are two important levels of analysis for the density plots presented in Figure ???:

**Internal analysis:** did the experiment confirm or deny the hypothesis it was meant to test (see Section 4.2)?

**External analysis:** are the collected data comparable in any way with the official data coming from QualAR?

With regards to the first angle of analysis, a first glance comparison of active and passive-related measurement charts might indicate that the hypothesis was firmly denied. However, one should look at the charts with some care. Both types of chart are always in the same scale, meaning that whatever is being measured, it appears to have approximately the same effect on both measurements. Moreover, if it is true that they exhibit different behaviours, it is also true that with respect to a trend, they seem to agree. The analysed data are too different in order to issue a confirmation of the proposed hypothesis, but they are also too close to conclude the opposite. Once misalignment issues are factored in, this becomes ever more evident. The hypothesis remains plausible, even if not confirmed.

The second lens through which one must look at the charts is the external analysis. This must also be done with some care. The first important thing to consider is that absolute quantities are of no importance here. The data collected through this experiment was not processed with the goal of providing a vertical column density

## CHAPTER 4. DISCUSSION

---

that could be compared to the official numbers. Besides this, although the air quality station that provided the QualAR data is not far from the place in which I ran the experiment, it is still sufficiently far that the absolute values should not be the same.

The QualAR chart tells us that, from 0700 onwards,  $\text{NO}_2$  concentration only goes down. This is in direct agreement with the  $\text{NO}_2$  cycle described in Section 2.1.1. Although not being as monotonic as the official data, our density charts (see Figure ??) confirm this. Two factors can be used to explain the behaviour difference that can be seen between our charts and QualAR's:

- misalignment issues may have introduced this discrepancy as an error;
- measurements may have been too close to the noise level, and therefore some instability is expected.

The second hypothesis is clearly the more worrisome, as it threatens the validity of the whole experiment. However, the fit charts in Figure ?? make this unlikely, since one can clearly see the signal above the noise.

## CONCLUSIONS

Lorem ipsum dolor sit amet, consectetur adipiscing elit. Ut purus elit, vestibulum ut, placerat ac, adipiscing vitae, felis. Curabitur dictum gravida mauris. Nam arcu libero, nonummy eget, consectetur id, vulputate a, magna. Donec vehicula augue eu neque. Pellentesque habitant morbi tristique senectus et netus et malesuada fames ac turpis egestas. Mauris ut leo. Cras viverra metus rhoncus sem. Nulla et lectus vestibulum urna fringilla ultrices. Phasellus eu tellus sit amet tortor gravida placerat. Integer sapien est, iaculis in, pretium quis, viverra ac, nunc. Praesent eget sem vel leo ultrices bibendum. Aenean faucibus. Morbi dolor nulla, malesuada eu, pulvinar at, mollis ac, nulla. Curabitur auctor semper nulla. Donec varius orci eget risus. Duis nibh mi, congue eu, accumsan eleifend, sagittis quis, diam. Duis eget orci sit amet orci dignissim rutrum.

Nam dui ligula, fringilla a, euismod sodales, sollicitudin vel, wisi. Morbi auctor lorem non justo. Nam lacus libero, pretium at, lobortis vitae, ultricies et, tellus. Donec aliquet, tortor sed accumsan bibendum, erat ligula aliquet magna, vitae ornare odio metus a mi. Morbi ac orci et nisl hendrerit mollis. Suspendisse ut massa. Cras nec ante. Pellentesque a nulla. Cum sociis natoque penatibus et magnis dis parturient montes, nascetur ridiculus mus. Aliquam tincidunt urna. Nulla ullamcorper vestibulum turpis. Pellentesque cursus luctus mauris.

Nulla malesuada porttitor diam. Donec felis erat, congue non, volutpat at, tincidunt tristique, libero. Vivamus viverra fermentum felis. Donec nonummy pellentesque ante. Phasellus adipiscing semper elit. Proin fermentum massa ac quam. Sed diam turpis, molestie vitae, placerat a, molestie nec, leo. Maecenas lacinia. Nam ipsum ligula, eleifend at, accumsan nec, suscipit a, ipsum. Morbi blandit ligula feugiat magna. Nunc eleifend consequat lorem. Sed lacinia nulla vitae enim. Pellentesque tincidunt purus vel magna. Integer non enim. Praesent euismod nunc eu purus. Donec bibendum quam in tellus. Nullam cursus pulvinar lectus. Donec et mi. Nam vulputate metus eu enim. Vestibulum pellentesque felis eu massa.

Quisque ullamcorper placerat ipsum. Cras nibh. Morbi vel justo vitae lacus tincidunt ultrices. Lorem ipsum dolor sit amet, consectetur adipiscing elit. In hac habitasse platea dictumst. Integer tempus convallis augue. Etiam facilisis. Nunc elementum fermentum wisi. Aenean placerat. Ut imperdiet, enim sed gravida sollicitudin, felis odio placerat quam, ac pulvinar elit purus eget enim. Nunc vitae tortor. Proin tempus nibh sit amet nisl. Vivamus quis tortor vitae risus porta vehicula.

## CHAPTER 5. CONCLUSIONS

---

Fusce mauris. Vestibulum luctus nibh at lectus. Sed bibendum, nulla a faucibus semper, leo velit ultricies tellus, ac venenatis arcu wisi vel nisl. Vestibulum diam. Aliquam pellentesque, augue quis sagittis posuere, turpis lacus congue quam, in hendrerit risus eros eget felis. Maecenas eget erat in sapien mattis porttitor. Vestibulum porttitor. Nulla facilisi. Sed a turpis eu lacus commodo facilisis. Morbi fringilla, wisi in dignissim interdum, justo lectus sagittis dui, et vehicula libero dui cursus dui. Mauris tempor ligula sed lacus. Duis cursus enim ut augue. Cras ac magna. Cras nulla. Nulla egestas. Curabitur a leo. Quisque egestas wisi eget nunc. Nam feugiat lacus vel est. Curabitur consectetur.

Suspendisse vel felis. Ut lorem lorem, interdum eu, tincidunt sit amet, laoreet vitae, arcu. Aenean faucibus pede eu ante. Praesent enim elit, rutrum at, molestie non, nonummy vel, nisl. Ut lectus eros, malesuada sit amet, fermentum eu, sodales cursus, magna. Donec eu purus. Quisque vehicula, urna sed ultricies auctor, pede lorem egestas dui, et convallis elit erat sed nulla. Donec luctus. Curabitur et nunc. Aliquam dolor odio, commodo pretium, ultricies non, pharetra in, velit. Integer arcu est, nonummy in, fermentum faucibus, egestas vel, odio.

Sed commodo posuere pede. Mauris ut est. Ut quis purus. Sed ac odio. Sed vehicula hendrerit sem. Duis non odio. Morbi ut dui. Sed accumsan risus eget odio. In hac habitasse platea dictumst. Pellentesque non elit. Fusce sed justo eu urna porta tincidunt. Mauris felis odio, sollicitudin sed, volutpat a, ornare ac, erat. Morbi quis dolor. Donec pellentesque, erat ac sagittis semper, nunc dui lobortis purus, quis congue purus metus ultricies tellus. Proin et quam. Class aptent taciti sociosqu ad litora torquent per conubia nostra, per inceptos hymenaeos. Praesent sapien turpis, fermentum vel, eleifend faucibus, vehicula eu, lacus.(5)

## BIBLIOGRAPHY

- [1] 2 Degrees Institute. *CO<sub>2</sub> Levels*. 2020. URL: <https://www.co2levels.org/> (visited on 04/14/2020) (cit. on p. 22).
- [2] U. S. D. of Agriculture. *Early History of the NCRS*. 2012. URL: <https://www.nrcs.usda.gov/wps/portal/nrcs/detail/national/about/history/?cid=stelprdb1049437> (visited on 04/11/2020) (cit. on p. 19).
- [3] M. N. Asl and A. Sadremomtaz. “Analytical image reconstruction methods in emission tomography”. In: *Journal of Biomedical Science and Engineering* 06.01 (2013), pp. 100–107. ISSN: 1937-6871. DOI: [10.4236/jbise.2013.61013](https://doi.org/10.4236/jbise.2013.61013). URL: <http://www.scirp.org/journal/doi.aspx?DOI=10.4236/jbise.2013.61013> (cit. on p. 42).
- [4] C. Beekman. “Differential Optical Absorption Spectroscopy of Trace Gas Species and Aerosols in the Upper Ohio River Valley”. PhD thesis. Ohio State University, 2010 (cit. on pp. 37, 38).
- [5] M. L. Bell, D. L. Davis, and T. Fletcher. “A retrospective assessment of mortality from the london smog episode of 1952: The role of influenza and pollution”. In: *Urban Ecology: An International Perspective on the Interaction Between Humans and Nature* 6.1 (2008), pp. 263–268. DOI: [10.1007/978-0-387-73412-5\\_15](https://doi.org/10.1007/978-0-387-73412-5_15) (cit. on p. 10).
- [6] G. P. Bishop, J. L. E. Flack, and M. Campbell. *Sensor Systems for Environmental Monitoring, Volume 2*. 1996. ISBN: 9789401065337 (cit. on p. 27).
- [7] T. Bourdrel et al. “Cardiovascular effects of air pollution”. In: *Archives of Cardiovascular Diseases* 110.11 (Nov. 2017), pp. 634–642. ISSN: 18752136. DOI: [10.1016/j.acvd.2017.05.003](https://doi.org/10.1016/j.acvd.2017.05.003). URL: <https://linkinghub.elsevier.com/retrieve/pii/S1875213617301304> (cit. on p. 14).
- [8] R. T. Brinkmann. “Rotational Raman scattering in planetary atmospheres”. In: *Astrophys J* 154 (1968), pp. 1087–1093. ISSN: 0004-637X. DOI: [10.1086/149827](https://doi.org/10.1086/149827) (cit. on p. 30).
- [9] R. D. Brook. “Cardiovascular effects of air pollution”. In: *Clinical Science* 115.5-6 (2008), pp. 175–187. ISSN: 01435221. DOI: [10.1042/CS20070444](https://doi.org/10.1042/CS20070444) (cit. on p. 13).

## BIBLIOGRAPHY

---

- [10] P. P. Bruyant. “Analytic and iterative reconstruction algorithms in SPECT.” In: *Journal of nuclear medicine : official publication, Society of Nuclear Medicine* 43.10 (2002), pp. 1343–58. ISSN: 0161-5505. URL: <http://jnm.snmjournals.org/cgi/content/abstract/43/10/1343%5Cnhttp://jnm.snmjournals.org/cgi/content/full/43/10/1343%5Cnhttp://www.ncbi.nlm.nih.gov/pubmed/12368373> (cit. on pp. 3, 40).
- [11] M. Buchwitz et al. “Global carbon monoxide as retrieved from SCIAMACHY by WFM-DOAS”. In: *Atmospheric Chemistry and Physics* 4.7 (Sept. 2004), pp. 1945–1960. ISSN: 16807316. DOI: [10.5194/acp-4-1945-2004](https://doi.org/10.5194/acp-4-1945-2004). URL: [www.atmos-chem-phys.org/acp/4/1945/](http://www.atmos-chem-phys.org/acp/4/1945/) (cit. on pp. 34, 35).
- [12] M. Buchwitz, V. V. Rozanov, and J. P. Burrows. “A near-infrared optimized DOAS method for the fast global retrieval of atmospheric CH<sub>4</sub>, CO, CO<sub>2</sub>, H<sub>2</sub>O, and N<sub>2</sub>O total column amounts from SCIAMACHY Envisat-1 nadir radiances”. In: *Journal of Geophysical Research: Atmospheres* 105.D12 (June 2000), pp. 15231–15245. ISSN: 01480227. DOI: [10.1029/2000JD900191](https://doi.org/10.1029/2000JD900191). URL: <http://doi.wiley.com/10.1029/2000JD900191> (cit. on pp. 34, 35).
- [13] R. L. Byer and L. A. Shepp. “Two-dimensional remote air-pollution monitoring via tomography”. In: *Optics Letters* 4.3 (Mar. 1979), p. 75. ISSN: 0146-9592. DOI: [10.1364/OL.4.000075](https://doi.org/10.1364/OL.4.000075). URL: <https://www.osapublishing.org/abstract.cfm?URI=ol-4-3-75> (cit. on pp. 5, 45).
- [14] CABI. *Air Pollution: Sources, Impacts and Controls*. Ed. by P. Saxena and V. Naik. 1st. Vol. 53. 9. Oxfordshire, UK: CAB International, 2019, pp. 1689–1699. ISBN: 9781786393890 (cit. on pp. 6, 13, 22–25).
- [15] L. Calderón-Garcidueñas et al. “Air pollution and detrimental effects on children’s brain. The need for a multidisciplinary approach to the issue complexity and challenges”. In: *Frontiers in Human Neuroscience* 8.AUG (2014), pp. 1–7. ISSN: 16625161. DOI: [10.3389/fnhum.2014.00613](https://doi.org/10.3389/fnhum.2014.00613) (cit. on p. 16).
- [16] N. Casaballe et al. “Comparison Between Regularized Optimization Algorithms for Tomographic Reconstruction of Plume Cross Sections in the Atmosphere”. In: *Earth and Space Science* 4.12 (Dec. 2017), pp. 723–736. ISSN: 23335084. DOI: [10.1002/2017EA000341](https://doi.org/10.1002/2017EA000341). URL: <http://doi.wiley.com/10.1002/2017EA000341> (cit. on p. 8).
- [17] CE Delft. *Health impacts and costs of diesel emissions in the EU*. Tech. rep. Delft: CE Delft, 2018, p. 72. URL: [www.cedelft.eu](http://www.cedelft.eu) (cit. on p. 3).
- [18] K. Chance and R. L. Kurucz. “An improved high-resolution solar reference spectrum for earth’s atmosphere measurements in the ultraviolet, visible, and near infrared”. In: *Journal of Quantitative Spectroscopy and Radiative Transfer* 111.9 (2010), pp. 1289–1295. ISSN: 00224073. DOI: [10.1016/j.jqsrt.2010.01.036](https://doi.org/10.1016/j.jqsrt.2010.01.036). URL: <http://dx.doi.org/10.1016/j.jqsrt.2010.01.036> (cit. on p. 39).
- [19] A. G. Clark. *Industrial Air Pollution Monitoring*. 1997. ISBN: 9789401071437. DOI: [10.1007/978-94-009-1435-3](https://doi.org/10.1007/978-94-009-1435-3) (cit. on pp. 27, 28).
- [20] CREE. *XLamp ® XHP50.2 LEDs Datasheet*. 2021 (cit. on p. 64).

- [21] T. Danckaert et al. *QDOAS*. 2015. URL: <http://uv-vis.aeronomie.be/software/QDOAS/> (cit. on pp. 30, 37, 73).
- [22] L. De Chiffre et al. “Industrial applications of computed tomography”. In: *CIRP Annals - Manufacturing Technology* 63.2 (2014), pp. 655–677. ISSN: 17260604. DOI: [10.1016/j.cirp.2014.05.011](https://doi.org/10.1016/j.cirp.2014.05.011). URL: <http://dx.doi.org/10.1016/j.cirp.2014.05.011> (cit. on p. 3).
- [23] P. de Prado Bert et al. “The Effects of Air Pollution on the Brain: a Review of Studies Interfacing Environmental Epidemiology and Neuroimaging”. In: *Current environmental health reports* 5.3 (2018), pp. 351–364. ISSN: 21965412. DOI: [10.1007/s40572-018-0209-9](https://doi.org/10.1007/s40572-018-0209-9) (cit. on pp. 16, 17).
- [24] M. Defrise, P. E. Kinahan, and C. J. Michel. *Positron Emission Tomography*. Ed. by D. L. Baley et al. London: Springer London, 2005, pp. 63–91 (cit. on pp. 3, 40, 76).
- [25] L. A. Dewerd and M. Kissick. *The Phantoms of Medical and Health Physics*. Ed. by L. A. DeWerd and M. Kissick. Biological and Medical Physics, Biomedical Engineering. New York, NY: Springer New York, 2014, p. 286. ISBN: 978-1-4614-8303-8. DOI: [10.1007/978-1-4614-8304-5](https://doi.org/10.1007/978-1-4614-8304-5). URL: <http://www.springer.com/series/3740%20http://link.springer.com/10.1007/978-1-4614-8304-5> (cit. on p. 56).
- [26] EEA. *Air pollution in Europe 1990–2004*. Tech. rep. 2. 2007 (cit. on p. 11).
- [27] EEA. *Air quality in Europe*. Tech. rep. 28. 2016, p. 83. DOI: [10.2800/80982](https://doi.org/10.2800/80982) (cit. on pp. 11, 13).
- [28] EEA. *European Environmental Agency*. 2019. URL: <https://www.eea.europa.eu> (visited on 09/23/2019) (cit. on pp. 25, 26).
- [29] D. M. Etheridge et al. *Historical CO<sub>2</sub> record from the Law Dome DE08, DE08-2 and DSS ice cores*. Tech. rep. Aspendale, Victoria, Australia: Division of Atmospheric Research, CSIRO. URL: <http://cdiac.ornl.gov/ftp/trends/co2/lawdome.combined.dat> (cit. on p. 22).
- [30] M. Fox. *Quantum optics*. Oxford, UK: Oxford University Press, 2006. ISBN: 9780198566724 (cit. on p. 65).
- [31] P. Frank and M. A. Ottoboni. *The Dose Makes The Poison: A Plain Language Guide to Toxicology*. 3rd Editio. Hoboken, New Jersey: John Wiley & Sons, Inc, 2011. ISBN: 9780470381120 (cit. on p. 11).
- [32] E. Frins et al. “Tomographic multiaxis-differential optical absorption spectroscopy observations of Sun-illuminated targets: a technique providing well-defined absorption paths in the boundary layer.” In: *Appl. Opt.* 45.24 (2006), pp. 6227–6240. ISSN: 0003-6935. DOI: [10.1364/AO.45.006227](https://doi.org/10.1364/AO.45.006227) (cit. on pp. 6, 8, 33, 47, 48).
- [33] S. Genc et al. “The adverse effects of air pollution on the nervous system”. In: *Journal of Toxicology* 2012 (2012). ISSN: 16878191. DOI: [10.1155/2012/782462](https://doi.org/10.1155/2012/782462) (cit. on pp. 16, 17).

## BIBLIOGRAPHY

---

- [34] F. C. Goldizen, P. D. Sly, and L. D. Knibbs. “Respiratory effects of air pollution on children”. In: *Pediatric pulmonology* 51.1 (2016), pp. 94–108. ISSN: 10990496. DOI: [10.1002/ppul.23262](https://doi.org/10.1002/ppul.23262) (cit. on p. 13).
- [35] J. F. GRAINGER and J. RING. “Anomalous Fraunhofer Line Profiles”. In: *Nature* 193.4817 (Feb. 1962), pp. 762–762. ISSN: 0028-0836. DOI: [10.1038/193762a0](https://doi.org/10.1038/193762a0). URL: <http://www.nature.com/doifinder/10.1038/193762a0> (cit. on p. 30).
- [36] C. Guerreiro, J. Soares, and A. G. Ortiz. *Air quality in Europe — 2019 report*. 5. Luxembourg: Publications Office of the European Union, 2019. ISBN: 9789294800886. DOI: [10.2800/822355](https://doi.org/10.2800/822355). URL: [papers2://publication/uuid/1D25F41B-C673-4FDA-AB71-CC5A2AD97FDD](https://papers2://publication/uuid/1D25F41B-C673-4FDA-AB71-CC5A2AD97FDD) (cit. on p. 3).
- [37] R. Gunderman. *Essential Radiology: Clinical Presentation, Pathophysiology, Imaging*, 2nd ed. 2nd ed. Thieme, 2006. ISBN: 9781588900821 (cit. on pp. 3, 39).
- [38] A. Hartl, B. C. Song, and I. Pundt. “Atmospheric Chemistry and Physics 2-D reconstruction of atmospheric concentration peaks from horizontal long path DOAS tomographic measurements: parametrisation and geometry within a discrete approach”. In: *Atmos. Chem. Phys* 6.3 (Mar. 2006), pp. 847–861. ISSN: 1680-7324. DOI: [10.5194/acpd-5-11781-2005](https://doi.org/10.5194/acpd-5-11781-2005). URL: <http://www.atmos-chem-phys.net/6/847/2006/> (cit. on p. 45).
- [39] A. Hartl et al. “2d tomographic reconstruction of trace gas distributions from long-path DOAS measurements: General approach, validation and outlook on an experiment on an urban site”. In: *Proceedings, 31st International Symposium on Remote Sensing of Environment, ISRSE 2005: Global Monitoring for Sustainability and Security* 2 (2005) (cit. on p. 45).
- [40] G. T. Herman. “Image Reconstruction From Projections”. In: *Real-Time Imaging* 1.1 (1995), pp. 3–18. ISSN: 10772014. DOI: [10.1006/rtim.1995.1002](https://doi.org/10.1006/rtim.1995.1002) (cit. on pp. 3, 40).
- [41] G. T. Herman. *Fundamentals of Computerized Tomography. Advances in Pattern Recognition*. London: Springer London, 2009. ISBN: 978-1-85233-617-2. DOI: [10.1007/978-1-84628-723-7](https://doi.org/10.1007/978-1-84628-723-7). URL: <http://link.springer.com/10.1007/978-1-84628-723-7> (cit. on pp. 3, 4, 40).
- [42] G. T. Herman, A. Lent, and S. W. Rowland. “ART: Mathematics and applications. A report on the mathematical foundations and on the applicability to real data of the algebraic reconstruction techniques”. In: *Journal of Theoretical Biology* 42.1 (1973). ISSN: 10958541. DOI: [10.1016/0022-5193\(73\)90145-8](https://doi.org/10.1016/0022-5193(73)90145-8) (cit. on pp. 3, 40, 43).
- [43] IEA. *Data & Statistics - International Energy Agency*. URL: [https://www.iea.org/data-and-statistics?country=World&fuel=Energy&20supply%5C&indicator=Total%20primary%20energy%20supply%20\(TPES\)%20by%20source](https://www.iea.org/data-and-statistics?country=World&fuel=Energy&20supply%5C&indicator=Total%20primary%20energy%20supply%20(TPES)%20by%20source) (visited on 04/17/2020) (cit. on p. 24).
- [44] International Agency for Research on Cancer. *Outdoor Air Pollution. IARC Monograph* 109. Vol. 109. 2016, p. 454. ISBN: 9789283201755 (cit. on p. 22).

- [45] M. Johansson et al. “Tomographic reconstruction of gas plumes using scanning DOAS”. In: *Bulletin of Volcanology* 71.10 (Dec. 2009), pp. 1169–1178. ISSN: 0258-8900. DOI: 10.1007/s00445-009-0292-8. URL: <http://link.springer.com/10.1007/s00445-009-0292-8> (cit. on pp. 8, 47).
- [46] A. Kak and M. Slaney. *Principles of Computerized Tomographic Imaging*. Society of Industrial and Applied Mathematics, 2001 (cit. on pp. 3, 4, 39, 40, 43, 44).
- [47] A. C. Kak and M. Slaney. *Principles of Computerized Tomographic Imaging*. 1. Society for Industrial and Applied Mathematics, Jan. 2001, pp. 49–112. ISBN: 978-0-89871-494-4. DOI: 10.1137/1.9780898719277. URL: <http://pubs.siam.org/doi/book/10.1137/1.9780898719277> (cit. on pp. 41, 44).
- [48] D. Kazantsev et al. “TomoPhantom, a software package to generate 2D–4D analytical phantoms for CT image reconstruction algorithm benchmarks”. In: *SoftwareX* 7 (Jan. 2018), pp. 150–155. ISSN: 2352-7110. DOI: 10.1016/J.SOFTX.2018.05.003. URL: <https://www.sciencedirect.com/science/article/pii/S2352711018300335?via%5C3Dihub> (cit. on p. 56).
- [49] B. Kitchenham and S. Charters. “Guidelines for performing Systematic Literature reviews in Software Engineering Version 2.3”. In: *Engineering* 45.4ve (2007), p. 1051. ISSN: 00010782. DOI: 10.1145/1134285.1134500. arXiv: 1304.1186. URL: <http://scholar.google.com/scholar?hl=en&btnG=Search%5C&q=intitle:Guidelines+for+performing+Systematic+Literature+Reviews+in+Software+Engineering#0%5C5Cnhttp://www.dur.ac.uk/ebse/resources/Systematic-reviews-5-8.pdf> (cit. on pp. 45, 46).
- [50] B. Kitchenham et al. “Systematic literature reviews in software engineering - A systematic literature review”. In: *Information and Software Technology* 51.1 (2009), pp. 7–15. ISSN: 09505849. DOI: 10.1016/j.infsof.2008.09.009. URL: <http://dx.doi.org/10.1016/j.infsof.2008.09.009> (cit. on p. 45).
- [51] T. Laepple et al. “Longpath DOAS tomography on a motorway exhaust gas plume: numerical studies and application to data from the BAB II campaign”. In: *Atmospheric Chemistry and Physics Discussions* 4.3 (May 2004), pp. 2435–2484. ISSN: 1680-7375. DOI: 10.5194/acpd-4-2435-2004. URL: [www.atmos-chem-phys.org/acp/4/1323/%20http://www.atmos-chem-phys-discuss.net/4/2435/2004/](http://www.atmos-chem-phys.org/acp/4/1323/%20http://www.atmos-chem-phys-discuss.net/4/2435/2004/) (cit. on pp. 6, 45).
- [52] LevelFiveSupplies. *LevelFiveSupplies*. 2021. (Visited on 06/21/2021) (cit. on p. 50).
- [53] S. Li et al. “Effect of ambient air pollution on premature SGA in Changzhou city, 2013-2016: A retrospective study”. In: *BMC Public Health* 19.1 (2019), pp. 1–10. ISSN: 14712458. DOI: 10.1186/s12889-019-7055-z (cit. on p. 14).
- [54] G. M. Lovett et al. “Effects of Air Pollution on Ecosystems and Biological Diversity in the Eastern United States”. In: *Annals of the New York Academy of Sciences* 1162.1 (Apr. 2009), pp. 99–135. ISSN: 00778923. DOI: 10.1111/j.1749-6632.2009.04153.x. URL: <http://doi.wiley.com/10.1111/j.1749-6632.2009.04153.x> (cit. on p. 18).

## BIBLIOGRAPHY

---

- [55] A. Merlaud. “Development and use of compact instruments for tropospheric investigations based on optical spectroscopy from mobile platforms”. PhD Thesis. Louvain: Faculté des Sciences - Université Catholique de Louvain, 2013. ISBN: 978-2-87558-128-0. URL: <http://books.google.com/books?hl=en&lr=%5C&id=inXVSyR82zwc%5C&oi=fnd%5C&pg=PR3%5C&dq=Development+and+use+of+compact+instruments+for+tropospheric+investigations+based+on+optical+spectroscopy+from+mobile+platforms+sciences%5C&ots=VdebeDBQMc%5C&sig=4G0eVEvthJXuqd8WI3IWjjVXuXc> (cit. on pp. 5, 29–31, 33, 36).
- [56] K. U. Mettendorf, A. Hartl, and I. Pundt. “An indoor test campaign of the tomography long path differential optical absorption spectroscopy technique”. In: (2005). DOI: [10.1039/b511337g](https://doi.org/10.1039/b511337g) (cit. on p. 45).
- [57] J. G. Murphy, S. O'Driscoll, and N. J. Smith. “Multipath DOAS for tomographic measurements”. In: *Opto-Ireland 2002: Optics and Photonics Technologies and Applications*. Ed. by T. J. Glynn. Vol. 4876. Mar. 2003, p. 875. DOI: [10.1117/12.463960](https://doi.org/10.1117/12.463960). URL: <http://proceedings.spiedigitallibrary.org/proceeding.aspx?doi=10.1117/12.463960> (cit. on p. 47).
- [58] G. E. Nilsson. *Respiratory Physiology of Vertebrates Life with and without oxygen*. Ed. by G. E. Nilsson. Oslo, Norway: Cambridge University Press, 2010. ISBN: 9780521878548 (cit. on pp. 11, 12).
- [59] S. O'Driscoll, J. G. Murphy, and N. J. Smith. “Computed tomography of air pollutants in street canyons”. In: *Spie 4876* (2003), pp. 958–967. DOI: [10.1117/12.463985](https://doi.org/10.1117/12.463985) (cit. on p. 47).
- [60] S. O'Driscoll, J. G. Murphy, and N. J. Smith. “Computed tomography of air pollutants in street canyons”. In: ed. by T. J. Glynn. Mar. 2003, p. 958. DOI: [10.1117/12.463985](https://doi.org/10.1117/12.463985). URL: <http://proceedings.spiedigitallibrary.org/proceeding.aspx?doi=10.1117/12.463985> (cit. on p. 47).
- [61] M. Office. *The Great Smog of 1952*. 2019. URL: <https://www.metoffice.gov.uk/weather/learn-about/weather/case-studies/great-smog> (visited on 09/23/2019) (cit. on p. 10).
- [62] D. Olsson, I. Mogren, and B. Forsberg. “Air pollution exposure in early pregnancy and adverse pregnancy outcomes: A register-based cohort study”. In: *BMJ Open* 3.2 (2013), pp. 1–8. ISSN: 20446055. DOI: [10.1136/bmjopen-2012-001955](https://doi.org/10.1136/bmjopen-2012-001955) (cit. on p. 15).
- [63] Oxford Press. *Lexico English Dictionary*. 2020. URL: <https://www.lexico.com/> (visited on 02/27/2020) (cit. on p. 17).
- [64] D. Perner et al. “OH - Radicals in the lower troposphere”. In: *Geophysical Research Letters* 3.8 (Aug. 1976), pp. 466–468. ISSN: 00948276. DOI: [10.1029/GL003i008p00466](https://doi.wiley.com/10.1029/GL003i008p00466). URL: <http://doi.wiley.com/10.1029/GL003i008p00466> (cit. on p. 5).
- [65] U. Platt and J. Stutz. *Differential Optical Absorption Spectroscopy - Principles and Applications*. Ed. by R. Guzzi et al. Heidelberg, Germany: Springer-Verlag Heidelberg Berlin, 2008. ISBN: 9783540211938 (cit. on pp. 5, 10, 11, 28, 29, 31–34, 45).

- [66] W. H. Press et al. *Numerical Recipes: The Art of Scientific Computing*. 3rd Editio. 2007. ISBN: 9788578110796. arXiv: [arXiv:1011.1669v3](https://arxiv.org/abs/1011.1669v3) (cit. on p. 31).
- [67] D. /. ProTeste. *Radão: perigo que se esconde no granito*. 2003. URL: <https://www.deco.proteste.pt/institucionalemedia/imprensa/comunicados/2003/radao-perigo-que-se-esconde-no-granito> (visited on 04/11/2020) (cit. on p. 21).
- [68] I. Pundt et al. “Mapping of tropospheric trace gas concentration distributions from ground and aircraft by DOAS-tomography (Tom-DOAS)”. In: () (cit. on pp. 5, 45, 75).
- [69] I. Pundt et al. “Measurements of trace gas distributions using Long-path DOAS-Tomography during the motorway campaign BAB II: Experimental setup and results for NO<sub>2</sub>”. In: *Atmospheric Environment* 39.5 (2005), pp. 967–975. ISSN: 13522310. DOI: [10.1016/j.atmosenv.2004.07.035](https://doi.org/10.1016/j.atmosenv.2004.07.035) (cit. on pp. 45, 46).
- [70] I. Pundt. “DOAS tomography for the localisation and quantification of anthropogenic air pollution”. In: *Analytical and Bioanalytical Chemistry* 385.1 (Apr. 2006), pp. 18–21. ISSN: 1618-2642. DOI: [10.1007/s00216-005-0205-4](https://doi.org/10.1007/s00216-005-0205-4). URL: <http://link.springer.com/10.1007/s00216-005-0205-4> (cit. on p. 45).
- [71] J. Radon. “On the determination of functions from their integral values along certain manifolds”. In: *IEEE Transactions on Medical Imaging* 5.4 (Dec. 1986), pp. 170–176. ISSN: 0278-0062. DOI: [10.1109/TMI.1986.4307775](https://doi.org/10.1109/TMI.1986.4307775). URL: <http://ieeexplore.ieee.org/document/4307775/> (cit. on p. 39).
- [72] R. Reis. *The Dust Bowl*. 1st ed. New York, New York, USA: Chelsea House, 2008. ISBN: 978-0-7910-9737-3 (cit. on pp. 19, 21).
- [73] V. Rozanov et al. “Sciatran - a new radiative transfer model for geophysical applications in the 240–2400 NM spectral region: the pseudo-spherical version”. In: *Advances in Space Research* 29.11 (June 2002), pp. 1831–1835. ISSN: 02731177. DOI: [10.1016/S0273-1177\(02\)00095-9](https://doi.org/10.1016/S0273-1177(02)00095-9). URL: <https://linkinghub.elsevier.com/retrieve/pii/S0273117702000959> (cit. on p. 35).
- [74] L. A. Shepp and B. F. Logan. “The Fourier reconstruction of a head section”. In: *IEEE Transactions on Nuclear Science* 21.3 (June 1974), pp. 21–43. ISSN: 0018-9499. DOI: [10.1109/TNS.1974.6499235](https://doi.org/10.1109/TNS.1974.6499235). URL: <http://ieeexplore.ieee.org/document/6499235/> (cit. on p. 56).
- [75] R. L. Siddon. “Fast calculation of the exact radiological path for a three-dimensional CT array”. In: *Medical Physics* 12.2 (Mar. 1985), pp. 252–255. ISSN: 00942405. DOI: [10.1118/1.595715](https://doi.org/10.1118/1.595715). URL: <http://doi.wiley.com/10.1118/1.595715> (cit. on pp. 51, 52).
- [76] E. Souza, A. Moreira, and M. Goulão. “Deriving Architectural Models from Requirements Specifications: a Systematic Mapping Study”. In: *Information and Software Technology* (Jan. 2019). ISSN: 09505849. DOI: [10.1016/j.infsof.2019.01.004](https://doi.org/10.1016/j.infsof.2019.01.004). URL: <https://linkinghub.elsevier.com/retrieve/pii/S0950584919300035> (cit. on p. 45).

## BIBLIOGRAPHY

---

- [77] C. Stachniss, C. Plagemann, and A. J. Lilienthal. “Learning gas distribution models using sparse Gaussian process mixtures”. In: *Autonomous Robots* 26.2-3 (Apr. 2009), pp. 187–202. ISSN: 0929-5593. DOI: 10.1007/s10514-009-9111-5. URL: <http://link.springer.com/10.1007/s10514-009-9111-5> (cit. on p. 56).
- [78] J. Stutz and U. Platt. “Numerical analysis and estimation of the statistical error of differential optical absorption spectroscopy measurements with least-squares methods”. In: *Applied Optics* 35.30 (1996), p. 6041. ISSN: 0003-6935. DOI: 10.1364/ao.35.006041 (cit. on pp. 58, 76).
- [79] J. Stutz et al. “A novel dual-LED based long-path DOAS instrument for the measurement of aromatic hydrocarbons”. In: *Atmospheric Environment* 147 (Dec. 2016), pp. 121–132. ISSN: 13522310. DOI: 10.1016/j.atmosenv.2016.09.054. URL: <http://linkinghub.elsevier.com/retrieve/pii/S1352231016307713> (cit. on pp. 6, 46, 47).
- [80] P. Tans et al. *Atmospheric CO<sub>2</sub> concentrations (ppm) derived from in situ air measurements at Mauna Loa Observatory, Hawaii*. Tech. rep. Mauna Loa, Hawaii, USA: NOAA/ESRL and Scripps Institution of Oceanography. URL: [ftp://aftp.cmdl.noaa.gov/products/trends/co2/co2\\_annmean\\_mlo.txt](ftp://aftp.cmdl.noaa.gov/products/trends/co2/co2_annmean_mlo.txt) (cit. on p. 22).
- [81] TSF and Lusa. *Erupção do Vulcão dos Capelinhos foi há 60 anos*. 2017. URL: <https://www.tsf.pt/sociedade/foi-ha-60-anos-a-erupcao-do-vulcao-dos-capelinhos-8798755.html> (visited on 04/11/2020) (cit. on pp. 19, 20).
- [82] UNICEF. “Levels & Trends in Child Mortality: Report 2013-Estimates developed by the UN Inter-agency Group for Child Mortality Estimation”. In: *Unicef/Who/Wb/Un* (2013), pp. 1–32. ISSN: 19326203. DOI: 10.1371/journal.pone.0144443 (cit. on p. 13).
- [83] R. Valente de Almeida and P. Vieira. “Forest Fire Finder – DOAS application to long-range forest fire detection”. In: *Atmospheric Measurement Techniques* 10.6 (June 2017), pp. 2299–2311. ISSN: 1867-8548. DOI: 10.5194/amt-10-2299-2017. URL: <https://www.atmos-meas-tech.net/10/2299/2017/> (cit. on pp. 2, 28, 31).
- [84] D. Vallero. *Fundamentals of air pollution*. 5th ed. Oxford, UK: Academic Press - Elsevier, 2014. ISBN: 9780124017337 (cit. on pp. 10–16, 18, 19, 21, 27).
- [85] P. Vieira and J. Matos. *System for Automatic Detection of Forest Fires Through Optical Spectroscopy*. 2008 (cit. on p. 2).
- [86] P. Vieira, J. Matos, and M. Mendes. *Sistema para a detecção automática de incêndios florestais por espectroscopia óptica*. 2007 (cit. on p. 2).
- [87] P. Virtanen et al. “SciPy 1.0: fundamental algorithms for scientific computing in Python”. In: *Nature Methods* 17.3 (Mar. 2020), pp. 261–272. ISSN: 1548-7091. DOI: 10.1038/s41592-019-0686-2. URL: <http://www.nature.com/articles/s41592-019-0686-2> (cit. on p. 75).
- [88] H. A. de Wit, J. P. Hettelingh, and H. Harmens. *ICP Waters Report 125/2015: trends in ecosystem and health responses to long-range transported atmospheric pollutants*. Tech. rep. 6946-2015. 2015 (cit. on p. 17).

## BIBLIOGRAPHY

---

- [89] World Bank. *World Bank Datasets*. URL: [data.worldbank.org](http://data.worldbank.org) (visited on 04/17/2020) (cit. on p. 24).
- [90] World Health Organization. *Radon and Health*. 2016. URL: <https://www.who.int/news-room/fact-sheets/detail/radon-and-health> (visited on 04/11/2020) (cit. on p. 21).
- [91] J.-M. Zhang and J. An. “Cytokines, Inflammation, and Pain”. In: *International Anesthesiology Clinics* 45.2 (2007), pp. 27–37. ISSN: 0020-5907. DOI: [10.1097/AIA.0b013e318034194e](https://doi.org/10.1097/AIA.0b013e318034194e). URL: <http://journals.lww.com/00004311-200704520-00004> (cit. on p. 17).

